Impacts of Urban Development and Climate Change on Extreme Rainfall over the PRD Region as Inferred from Dynamical Downscaling Experiments

HU, Chenxi

A Thesis Submitted in Partial Fulfillment

of the Requirements for the Degree of

Master of Philosophy

in

Earth and Atmospheric Sciences

The Chinese University of Hong Kong

October 2019

Thesis Assessment Committee

Professor LEE Shing Yip (Chair)

Professor TAM Chi Yung Francis (Thesis Supervisor)

Professor TAI Pui Kuen Amos (Committee Member)

Professor LI Yubin (External Examiner)

Abstract of thesis entitled

Impacts of Urban Development and Climate Change on Extreme Rainfall over the PRD Region as Inferred from Dynamical Downscaling Experiments
Submitted by **HU, Chenxi**
for the degree of **Master of Philosophy in Earth and Atmospheric Sciences**
at The Chinese University of Hong Kong in **October 2019**

Abstract

It is well-known that the Pearl River Delta (PRD) has experienced rapid urbanization since 1990s, and a significant increase (about 5 – 10%) of the extreme rainfall can be observed over Southern China in recent decades, which will keep increasing further in the 21st century. Both warmer climate condition and urban development have affected the local precipitation. In this study, impacts of both urban development and global warming on extreme rainfall over the PRD region are examined by utilizing a mesoscale model to dynamically downscale Global Climate Model (GCM) simulations.

In the first part of this study, the sensitivity of extreme local rainfall to the level of urbanization over the PRD megacity region during the summer (May, June, July, August, and September, MJJAS) is investigated. After selecting 26 non-TC (without effect of tropical cyclone) extreme precipitation events with intensity reaching the 99% of daily rainfall from the Geophysical Fluid Dynamical Laboratory Earth System model version 2 (GFDL-ESM2M) historical simulation data, dynamic downscaling is carried out for these cases by using Weather Research and Forecasting

(WRF) model coupled with an urban canopy model (UCM). In particular, three numerical experiments corresponding to different levels of urbanization are conducted: in the first experiment (referred to as NO-URBAN), urban land use over the PRD which came from the 2004 Moderate Resolution Imaging Spectroradiometer (MODIS) data is replaced by cropland in the model environment; In the second experiment (referred to as AH0), anthropogenic heat (AH) within the UCM is set to zero, while in the third (referred to as AH300) the diurnal peak of AH is set to $300Wm^{-2}$ in the urban area. Results show that the increase of accumulated rainfall in the urban area is more sensitive to rather the intensity of AH than the change of surface properties. Compared with NO-URBAN, the hourly mean rainfall in the urban cluster area of AH300 increases by around 0.7mm/hr, and extreme rainfall (higher than 50mm/hr) occurrence is almost doubled in AH300, which can be attributed to a higher surface temperature (with magnitude about 3.5 to 4°C), higher convective available potential energy (CAPE), and lower convective inhibition (CIN); thus an environment more conducive to strong convection over the urban areas. Enhanced rainfall in AH300, compared to NO-URBAN, is supported by more moisture supply from the South China Sea and increased water vapor flux convergence over the PRD city area. Moreover, it shows that the moisture flux convergence has a strong relationship with the direction of prevailing background wind over the PRD city region. In general, urbanization increases both the intensity and frequency of extreme local rainfall over the PRD megacity.

In the second part, how urban development and climate change might affect near-future projections of rainfall extremes in the PRD megacity area is investigated. By applying the similar case selection method as in the first part, 30 extreme cases are selected from GFDL-ESM2M present run (1951-2000) and future (RCP8.5) (2001-2050) projections and dynamically downscaled by WRF-UCM. Moreover, the historical land use/land cover (LULC) data in 1999 and the near-future projection in 2030 (based on Cellular-Automata-type land use change modeling) built on the World Urban Database and Access Portal Tools (WUDAPT) method are used, to represent the PRD megacity land use in 1999 and 2030, respectively. Three experiments under various background climate and land use/land cover conditions are conducted, with land use in 1999 and present climate condition (1999LS-HIS), land use in 1999 and future climate condition (1999LS-FUT), land use in 2030 and future climate condition (2030LS-FUT). Results show that both global warming and urban development can lead to an increase in rainfall intensity around 5-12mm/day in the PRD metropolitan area. The probability of heavy rainfall (higher than 50mm/hr) will probably double in the near future over the urban area due to warming and urban development. However, global warming tends to suppress the frequency of light rainfall (by 1–20mm/hr), while the probability of rainfall at the range of 1-10mm/hr decreases by about 30%. CIN has an increase under warmer climate, which makes convection more difficult to be triggered. Urban development results in an increase of rainfall frequency at all ranges (1–110mm/hr) over the urban area, this effect is regional, it increases rainfall more in the central PRD megacity area. For urban

development, the increase of rainfall intensity and frequency can be attributed to the increased CAPE, which creates a more unstable atmosphere during these extreme rainfall cases. Besides, considering the diurnal change of rainfall, global warming may lead to the delay in the peak diurnal rainfall to later hours in the afternoon during these extreme rainfall cases, possibly due to the high sensitivity of land-sea breeze characteristics and the time period used in simulations.

摘要

眾所周知近珠三角地區自 1990 年來經歷了一系列急速城市化的進程，同時近幾十年來華南地區觀測到顯著的極端降水強度增長（5%到 10%），這一增長趨勢在未來將保持。同時全球氣候變化與城市發展都會對本地降水帶來影響。本研究通過在天氣尺度模式下對全球氣候模式進行動力降尺度分析來檢驗城市發展與全球變暖對珠三角地區（PRD）極端降水所帶來的影響。

本研究的第一個部分重點研究了珠三角城市區域地區夏季（五到九月）當地極端降水與城市化等級的敏感度。基於 GFDL-ESM2M 歷史模擬的 99%日平均降水作為閾值，26 個不受颱風影響的極端降水個例被選出，這些個例通過耦合了 UCM 模式的 WRF 模式進行了動力降尺度分析。同時根據不同的城市化程度，我們設計了三個對比實驗：在第一個實驗（NO-URBAN）中，珠三角地區的城市在模式環境中被替換成了農田，在第二個實驗中（AH0），在城市冠層模式中使用了城市下墊面，但人為熱排放被設置為 0，而第三個實驗中，珠三角地區城市區域人為熱排放的日變化峰值被設置為 300Wm^2。研究結果表明，城市區域的累計降水增強對人為熱排放強度的敏感性（基於 AH300 與 NO-URBAN 的實驗結果對比）要高於其對城市下墊面變化的敏感性（基於 AH0 與 NO-URBAN 的實驗結果對比）。對比 NO-URBAN 實驗，城市區域的逐小時平均降水增加了大約 0.7mm/hr，而 AH300 實驗中的極端降水率（定義為大於 50mm/hr 的降水）幾乎翻倍。這個變化可以用城市區域中更高的地表溫度、更高的對流可用位能（CAPE）和更低的對流抑制能（CIN）來解釋，因而城市環境中更容易導致對流的發生。同時對比 AH300 與 NO-URBAN，珠三角地區的城市區域作為輻合中

心獲得了來自南海的充足水汽而導致大氣中濕度的增強 這些水汽支持了降水的增強。此外, 水汽通量散度的變化與背景風場的方向有著密切的關係。總而言之, 可以看到珠三角區域的城市化會顯著的增強當地極端降水的強度與頻率。

本研究的第二個部分主要研究城市發展以及氣候變化對珠三角地區近未來極端降水的影響。通過使用與本研究第一部分相同的方法, 我們從 GFDL-ESM2M 歷史 (1951-2000) 與近未來 (2001-2050) 模擬中各自選出 30 個與颱風無關的極端降水個例。同時, 1999 年的土地利用數據以及預測的 2030 年的土地利用數據 (基於 cellular-automata-type 土地利用變化模式) 被用來模擬 1999 年以及近未來 2030 年珠三角地區的城市化情況。通過改變土地利用數據以及氣候條件, 這個研究同樣設計了 3 個對比實驗。第一個實驗 (1999HIS) 中使用 1999 年珠三角的土地利用數據以及現在的氣候條件, 第二個實驗 (1999FUT) 使用 1999 年珠三角的土地利用數據以及近未來的氣候條件, 第三個實驗 (2030FUT) 使用 2030 年珠三角的土地利用數據以及近未來的氣候條件。結果表明, 城市發展與全球變暖效應都會導致珠三角城市區域降水強度增強 5-12 毫米每天。但同時全球變暖可能抑制小雨的發生, 導致小雨 (1-10 毫米每小時) 發生率降低 30%。而城市發展則會導致城市區域的降水頻率在所有強度上增強。此外, 城市發展對降水的影響是局地的, 主要在城市中心地區。降水強度與頻率的增強可能是由於對流可用位能的增加導致的 從而使得在極端降水事件中大氣變得更不穩定。此外, 全球變暖可能會導致極端降水事件中日降水峰值時間發生一個小時的延後 這可能是由於降水抑制陸地溫度從而減弱了海陸熱力差異而導致的。

Table of Contents

List of Figures

List of Tables

Chapter 1

1 Introduction

1.1 Urbanization

1.1.1   Urbanization in the Pearl River Delta region

Since the last century, rapid urbanization can be observed in a lot of places over the globe. Urbanization has a significant impact on the local climate, such as extremely high temperature (Mohajerani e al., 2017), precipitation (Huff and Changnon., 1972 and Han et al., 2013) and local circulation (Li et al., 2016). Due to more heavy precipitation and extreme temperature, urban flooding and heat waves have become increasingly common in many cities in China. Therefore, it is necessary to investigate and understand how urbanization might affect the local climate for preparedness and mitigation of disasters during recent decades.

The Pearl River Delta (PRD) region is a megacity cluster located in the Southern coast of China, it receives a high amount precipitation during the summer in addition to the Asian summer monsoon and also tropical cyclones (TC). Since the early 1990's, the PRD area has experienced a rapid urbanization. It now accounts for almost 10% of China's economic aggregate, and has become the largest megacity cluster in the world. Comparing the build-up area in 1999 and in 2010, the urban fraction changed from 3.56% to 15.18% in the PRD land area. Figure 1.1 gives the land cover distribution over PRD region in 1990 and 2009 respectively, based on the United States Geological Survey (USGS) land use data. Comparing Figure 1.1a and b,

it can be seen that the PRD urban area has greatly expanded during these 30 years, with more than 5 time of increase due to its rapid economic growth.
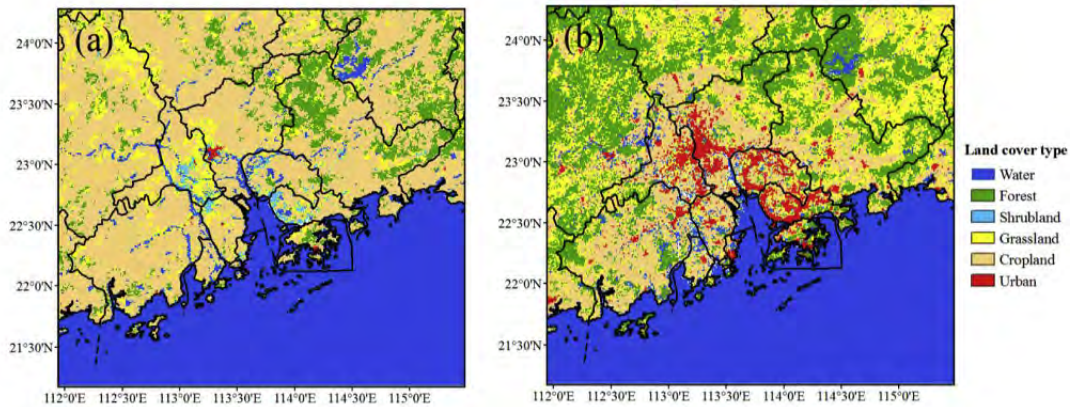
Figure 1.1 (a) Land use categories in the PRD region based on 1990 USGS data, while urban and build-up shown areas in red, and orange, yellow, blue, green and blue represent the cropland, grassland, shrubland, forest and water respectively. (b) Same as (a) but for land use categories from 2010 USGS data.

1.1.2 Urban meteorology

With the change of land surface, urbanization can influence the local atmosphere, especially the planetary boundary layer (PBL). Many researches have investigated the effect of urbanization on the local meteorology, and it has been found that urban surface properties, urban morphology, anthropogenic aerosols, and anthropogenic heat (AH) can play important roles. For land surface properties, the artificial surfaces lead to lower albedo, higher heat conduction, and more heat capacity than rural surfaces. Also, compared with natural surfaces, urban area means less water permeability: concrete and asphalt prevent the release of moisture and decrease surface evaporation, which results in lower surface moisture content in the urban area, especially in summer. (Bornstein, 1968; Oke, 1988). Moreover, changes

of the surface can also reduce the latent heat flux to the atmosphere (Bornstein, 1968; Oke, 1988), which can decrease convective available potential energy (CAPE) (Guo et al., 2006; Zhang et al., 2009).

For urban morphology, the structure of city buildings results in more absorption of solar radiation and higher surface temperature. Walls and roofs of the building can absorb radiation and store the heat in the daytime, and the release of which leads to higher night temperature over the city area (Soltani and Sharifi, 2017). Urban area also has higher roughness length than cropland and grassland due to building height deviation and building distances, which can slow down the surface wind (Coceal and Belcher, 2004; Hou et al., 2013). Apart from urban structure, AH plays a role in many aspects. It is known that AH can significantly enhance the Urban Heat Island (UHI) effect, and also the frequency and intensity of extreme rainfall (Holst et al. 2016). Finally, the anthropogenic-induced aerosols have a complex influence on urban meteorology such as cooling effect which can reduce the surface temperature in the urban area (Wang et al., 2018), or act as condensation core to play an essential role in orographic precipitation process (Creamean et al., 2013).

1.1.3   Urban Heat Island effect

Properties of the urban land surface can change the surface energy balance and lead to a warming effect over the city area (Tayanc and Toros, 1997). This effect is called UHI effect and was first studied in the city of London (Howard, 1833). The main reason of the UHI effect is the modification of land surface (Solecki et al., 2005)

and energy-induced heat flux (Li and Zhao, 2012). The intensity of UHI has a positive relationship with the density of population and urban expansion (Wu and Zhang, 2018). Figure 1.2 shows how UHI occurs over a city area. Generally, more radiative heat is absorbed by the surface, which increases heat transfer from the surface to the atmosphere. Also, AH release can lead to the rise of air temperature over urban areas.
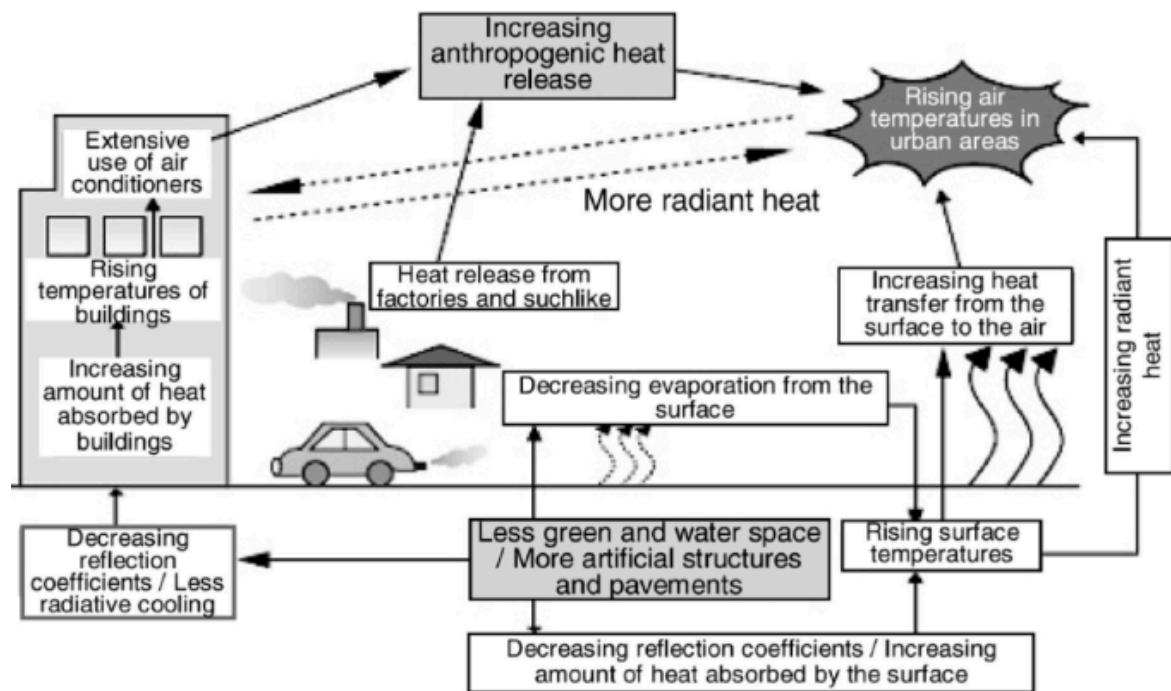
Figure 1.2 *How UHI occurs. (Source: Mohajerani, Bakaric and Jeffrey, 2017)*

Urbanization tends to enhance the UHI effect (Oke, 1973), and megacity areas tend to have stronger surface temperature than surrounding rural area (Adachi, 2012). Moreover, the temperature increase due to UHI is usually about 2 to 3°C and can be further enhanced with more population. The UHI effect can play a role in the local circulation and weather system in the large scale. UHI can also alter the development of clouds and fog (Sachweh and Koepke, 1995), and it is already known that the temperature anomaly between urban and rural areas can change atmospheric stability

and turbulence (Jin et al. 2015), frequency of lightning strikes (Orville et al. 2001), thunderstorm and precipitation (Changnon and Huff, 1986).

1.1.4   Impacts of urbanization on precipitation

Rapid urbanization has a strong influence on both frequency and intensity of extreme event, which can cause heavy economic losses to our society. The effects of urbanization on the local climate has become a hot research topic in recent years. Since the last century, some pieces of observational evidence about the changes of precipitation related to urbanization have been revealed. Changnon reported that the urban influence on precipitation tends to be found in the La Porte area downwind of Chicago (Changnon 1968). After this pioneering work, many researches had focused on rainfall anomalies over the urban downwind locations. Based on the Metropolitan Meteorological Experiment (METROMEX), Changnon found that total rainfall and severe storm activities of St. Louis increased up to 30% and 100% respectively, around 15 to 40 km downwind of city in summer, indicating that the UHI effect can enhance the downstream precipitation (Huff and Changnon, 1986). By using Tropical Rainfall Measuring Mission (TRMM) from January 1998 to May 2002, Shepherd and Burian also found the annual mean rainfall is maximum in the downwind of Houston (Shepherd and Burian, 2003). UHI intensities also have a positive correlation with rainfall amounts in summer in the Continental United States (CONUS) (Gu and Li, 2017). Besides, there are also many studies based on numerical models. Shem and Shepherd simulated two extreme precipitation cases in Atlanta; it was found that the

center of rainfall increment caused by UHI was located downwind of the city, by 10 to 13% (Shem and Shepherd, 2009). A summary of results on urban influence on rainfall was recently given by Lin and Niyogi (2019). See Figure 1.3.
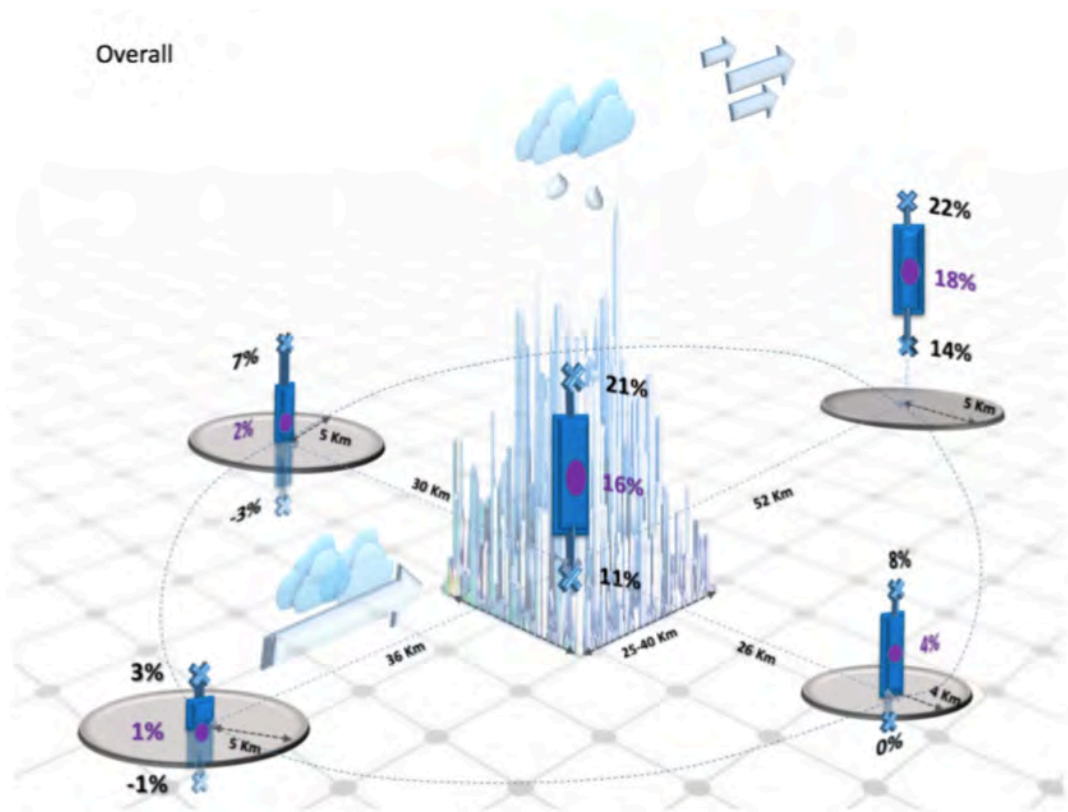
Figure 1.3 *Precipitation changes over urban areas and for surrounding landscape. The bars indicate the sample standard deviation for the precipitation change, and circles correspond to the mean change in precipitation location. (Source: Liu and Niyogi, 2019)*

By utilizing Climate Prediction Center morphing (CMORPH) data, it was found that there is stronger afternoon rainfall in the urban area in PRD, than in the surrounding rural area (Chen et al., 2015). Lin et al. used the MM5 mesoscale model to study the impact of urbanization on precipitation over Taiwan; they found that after increasing the city area of Taichung, the precipitation center moved from the

mountain to the area downstream of the city (Lin et al., 2007). Holst et al. designed several numerical experiments to investigate the sensitivity of urban rainfall to surface AH in PRD; they showed that heavy rainfall rates have a high sensitivity to AH (Holst et al., 2016). However, the influence of urbanization is complex and might depend on the geographical location. Strong UHI can cause rainfall to increase directly in the Beijing urban area, while for weak UHI, rainfall will be bifurcated and avoid the city center (Dou et al., 2015; Zhang et al., 2017). Fung (2018) found that AH can significantly increase the probability of extreme precipitation in urban PRD locations based on dynamical downscaling experiments. The location of the city may also be an important factor, in relation to availability of moisture in the surrounding area. Shimadera et al. used WRF to simulate the precipitation in Osaka Kinki region for August from 2006 to 2010, which is a coastal megacity cluster in Japan. Because of the stronger sensible heat flux, the formation and development of convective clouds also enhanced, and the substantial moisture supply led to a 27% increase of total precipitation in the urban area (Shimadera et al., 2015). By utilizing the WRF model, Kusaka (2014) designed sensitivity experiments to examine the urbanization effect on precipitation climatology in Tokyo, which is also a coastal megacity. It was found that urbanization can lead to a robust increase of rainfall amount in the Tokyo metropolitan region, but a decrease in more inland location. The increase of urban rainfall within the city can be attributed to the increase of surface sensible heat flux, which leads to lower atmospheric stability and stronger convection.

1.2 Climate change

1.2.1　Climate change in PRD

Climate change can pose a remarkable and multidimensional threat to our living environment (IPCC 2012). Greenhouse gas related to anthropogenic activities can lead to global warming, and changes in the large-scale circulation, frequency and intensity of extreme temperature (Raymond et al., 2016), droughts (Sheffield and Wood, 2007) and extreme precipitation (Hsu et al., 2012) in many locations. It is therefore essential to investigate the impact of climate change on heavy precipitation.

Regarding global warming, temperature of the urban area in Hong Kong kept increasing at a rate of about 0.12°C per decade during the past 118 years, according to observations from the Hong Kong Observatory (HKO) (Leung et al., 2004; see Figure 1.4). Apart from temperature, both extreme precipitation magnitude and frequency also increased in the PRD region (IPCC 2007 and 2012; Xu et al., 2015). Figure 1.5 shows the trend of total daily precipitation exceeding the 95% threshold (R95P) and the Simple Day Intensity Index for Rain (SDII) during 1951-2010 according to the IPCC WG1 AR5, here, SDII was computed as accumulated rainfall averaged by number of wet days (daily rainfall larger than 0.1mm/day). It can be seen that both extreme rainfall and accumulated rainfall have increased significantly in the whole South China during the recent 60 years. Moreover, the increasing trend of extreme rainfall and accumulated rainfall can reach 15 to 20% and 5% to 10% per decade over the PRD.
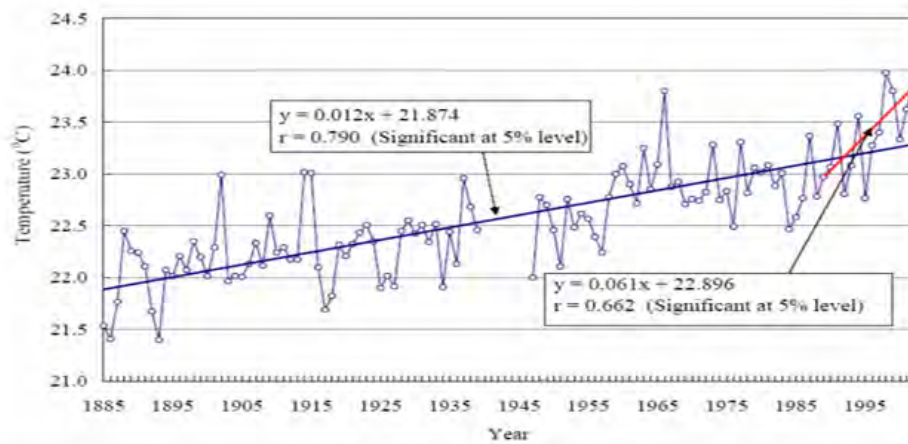
Figure 1.4 Long term annual mean temperature trend from 1885 to 2003 in Hong Kong, based on station observation data in Hong Kong. (Source: Leung et al.) 2004)
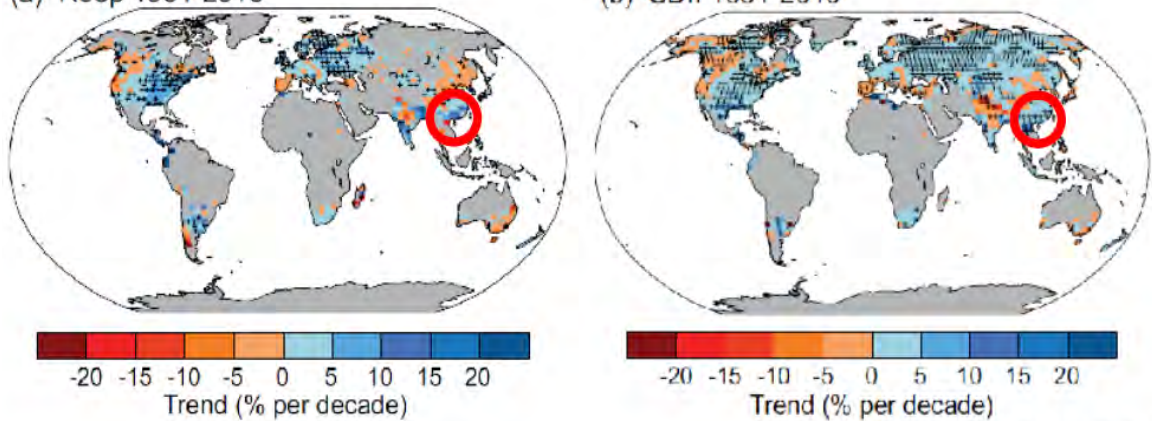
Figure 1.5 (a) R95p trend from 1951-2010 per decade, red circle represents the South China region. (b) Same as (a) but for global trend of SDII.

1.2.2 Regional impacts of climate change on precipitation

Higher temperature tends to increase the atmospheric moisture content and surface evaporation, leading to more precipitable water which is conductive to stronger extreme rainfall. However, due to more latent heat released in high altitude, global warming is characterized by warmer upper atmosphere and stronger atmospheric static stability. The latter effect tends to suppress convection or rainfall

(Chou et al., 2012). The impact of global warming on the mean rainfall also depends on the location of interest region; land-sea contrast may be weaker due to global warming (Ueda et al. 2016), which may lead to the decline of monsoon circulation. It is found that global warming has an impact on the India monsoon in that the number of dry (wet) days increases (decreases) (Rani and Sreekesh, 2018; Yaduvanshi et al., 2017). However, observations do not show any trend in South Asia summer monsoon in intensity during the recent 50 years, except a southward shift (Li et al., 2010). Overall the impact on global warming on rainfall is highly complex, with the intensity change affected by factors such as atmospheric stability and monsoon circulation, and the effect strongly depends on the location and season.

On the other hand, according to both observations and climatic model simulations, there is evidence that global warming can increase both strength and frequency of extreme rainfall. According to the Clausius-Clapeyron (CC) relationship (Ali and Mishra, 2017), the saturated vapor pressure (e_s) is related to the temperature (T):

$$e_s(\text{hPa}) = 6.11 \times 10^{\frac{7.5 \times T(^oC)}{273.3 + T(^oC)}}$$

The saturated vapor pressure increases by 6 to 7% per degree increase in near-surface temperature, which means the atmosphere can accommodate more water vapor. With higher moisture capacity and evaporation, the atmosphere will get wetter

in the future. Hence, heavy rainfall which drains out moisture from atmosphere column will be stronger and more frequent.

The changes in extreme rainfall were first documented by Iwashima and Yamamoto (1993) who used the strongest three yearly extreme rainfall scores from stations in Japan and the United States. They also found that the extreme rainfall indeed has a decadal increasing trend in both countries. By using 200 long-term stations' observation data, Karl and Knight (1998) demonstrated that the highest daily precipitation events had a significant increasing linear trend over most of Contiguous United States from 1910 to 1995. By using satellite observations, Allan and Soden (2008) also found that there was a distinct link between extreme rainfall and increase of temperature; during warmer periods, observed amplification of extreme rainfall was found to be larger than that predicted by models, which meant that the projections of global warming in extreme rainfall might be underestimated.

There are also studies using numerical simulations for examining the relationship between global warming and extreme rainfall. Gordon et al. (1992) utilized the CSIRO 4-level general circulation model with different CO2 conditions, and found significant increase in convection rainfall and a decrease in non-convective rainfall in mid latitudes. Also, the frequency of massive rainfall increases, while its return period decreases significantly in all regions. By utilizing coupled general circulation models (GCMs), Kharin et al. (2007) found that relative change in the intensity of extreme rainfall generally exceed that in the annual mean precipitation,

particularly in tropical and subtropical regions. Chen (2013) also examined the future

projected rainfall by using 16 Coupled Model Inter-comparison Project Phase 5

(CMIP5) models under RCP4.5 and RCP8.5. They showed that intensity of heavy

precipitation (larger than 50 mm/day) will increase by about 32% at the end of 21st

century for both climates scenarios, while the global warming will suppress light

rainfall (1 to 10 mm/day).

1.3 Dynamical downscaling

GCMs are useful tools for projecting the future climate, but they do not

perform well in representing the regional climate due to their relatively coarse

resolution. Dynamical downscaling is a technique that makes use of high-resolution

regional climate models (RCMs) to obtain regional climate information, based on

lateral boundary conditions provided from a GCM. RCMs can better incorporate

surface heterogeneities, land-sea contrast, complex topography, and can compute the

regional circulation to a more accurate level (Bao et al., 2015). Figure 1.6 shows the

2000 - 2014 JJA mean air surface temperature from observations, National Centers

for Environmental Prediction (NCEP) Global Final Analysis (FNL), ERA-Interim,

and WRF downscaling results using FNL as boundary conditions, and also

downscaling results based on ERA-Interim (Huang and Gao, 2018). It can be found

that the summer mean air temperature decreased from south to north over China

according observations, FNL and ERA-Interim results show some biases in the

temperature distribution. Both FNL and ERA-Interim results can not capture the south

to north temperature gradient, and FNL (ERA-Interim) output has a clod (hot) bias over eastern China. However, after dynamical downscaling by WRF, the simulated air temperature become more comparable to observations. For example, there are finer details in South China, with the underestimation (overestimation) in FNL (ERA-Interim) adjusted in eastern China, and clearer north - south temperature gradient. Dynamical downscaling is a useful method for local climate studies.
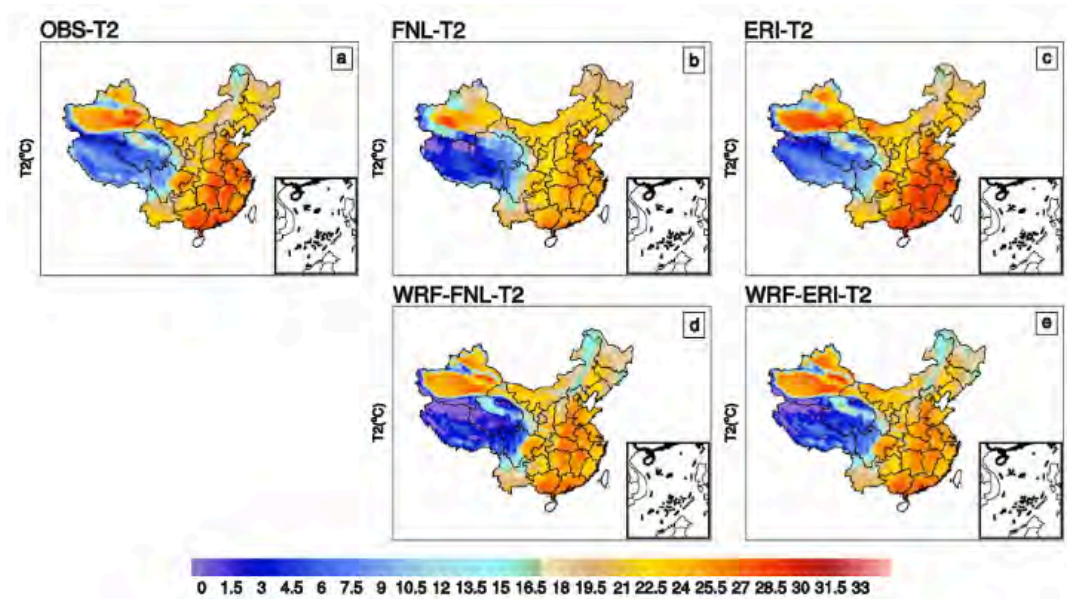
Figure 1.6 *Spatial distributions of summer mean air surface temperature (units: °C) for 2000–2014 over China from observations (a), FNL (b), ERI (c), and downscaling simulations WRF-FNL(d), and WRF-ERI (e). (Source: Huang and Gao, 2018)*

Chapter 2

2 Methodology

2.1 Outline of this study

As mentioned in Chapter 1, many studies have investigated the impact of urbanization and global warming on extreme rainfall based on observations or numerical simulations. However, only a few of them focus on the influence of urban developing expansion, especially in coastal cities. This study seeks to investigate these issues with the following objectives: (1) to examine the sensitivity of extreme rainfall to urban land use, and (2) to project changes in extreme rainfall characteristic due to near-future urban development and global warming conditions. To investigate the influence of both urbanization and climate change on extreme rainfall, a mesoscale model is utilized to dynamically downscale the global climate model (GCM) output. The GCM used in this study is the Geophysical Fluid Dynamical Laboratory Earth System model version 2 (GFDL-ESM2M) (see section 2.2) and the mesoscale model utilized is the Weather Research and Forecasting (WRF) model with the Advanced Research WRF (ARW) dynamical core version 3.8.1. In part 1, to enhance the robustness of results, 26 extreme rainfall cases are selected from GCM's daily rainfall output. These cases are not related to tropical cyclone (TC) occurrence, and are referred to as non-TC cases. To investigate the effects of urbanization, dynamical downscaling for each of these extreme cases is carried out with three

parallel experiments using different surface properties and urban parameters. In part 2, 30 non-TC extreme rainfall cases are selected from the GFDL-ESM2M historical run, and also near-future projections according to the RCP8.5 scenario. Extreme cases are downscaled with different urban land use conditions, for different climate scenarios. The following sessions introduce the selection criteria of extreme rainfall cases identification based on GFDL-ESM2M outputs, and details of dynamical downscaling by utilizing WRF-ARW.

2.2 Observation data used

For model evaluation in this study, two observational data sets are used to test the performance of GFDL-ESM2M. The Tropical Rainfall Measuring Mission (TRMM) 3B42 is a satellite mission between NASA and the Japan Aerospace Exploration (JAXA) Agency, and its data are used for research on tropical precipitation. This data cover the 50S to 50N band with $0.25^{o}*0.25^{o}$ spatial resolution, with temporal resolution of 3hours. In this study, TRMM precipitation data from 1998 to 2013 are regrided into $2.5^{o}*2^{o}$ for evaluating the precipitation performance of GFDL-ESM2M over East Asia region.

For other circulation variables such as temperature and wind, ERA-Interim is used to examine the performance of GFDL-ESM2M over East Asia. ERA-Interim is the global reanalysis data from the European Centre for the Medium-Range Weather Forecasts (ECMWF) (Dee et al. 2011) from 1979 to present, which proposes to improve the performance of previous reanalysis data ERA-40 in some aspects such as

hydrological cycle (Berrisford et al. 2011). The ERA-Interim data covers global scale atmosphere observation parameters with 1.5º*1.5º spatial resolution, 37 vertical level from surface to 1hPa, and 6hours temporal resolution. Same as TRMM data, the temperature and U,V wind from ERA-Interim are also regrided into 2.5º*2º resolution.

2.3 GFDL-ESM2M

The GCM utilized in this study is the GFDL-ESM2M (Dunne et al. 2012, 2013) with Modular Ocean Model version 4 (MOM4) as its ocean component. GFDL-ESM2M is the updated version of GFDL climate model version 2.1 (GFDL-CM2.1), and has been used in many studies due to its reasonable performance in East Asia monsoon circulation, temperature, etc. (McSweeney el al. 2015). The atmospheric component of GFDL-ESM2M has horizontal resolution of 2ºx 2.5º in latitude and longitude. The performance of some circulation variables in GFDL-ESM2M is also evaluated. Figure 2.1 shows the distribution of summer mean precipitation over East Asia from GFDL-ESM2M simulations and TRMM-V3B42 reanalysis data from 1998 to 2013. Results show that the model can reproduce major features well in East Asia such as heavy rainfall in south Tibet Plateau and over the western North Pacific. But the model still has its limitation in some areas and may underestimate the intensity of rainfall in South China. The intensity of summer mean rainfall over South China is about 8-9mm/d based on TRMM, but only 4-5mm/d from

the GFDL-ESM2M data. Therefore, the intensity of extreme cases over PRD region selected from GFDL-ESM2M may be underestimated compared to observations.

Figure 2.2 gives the distribution of summer mean 850hPa wind over East Asia from GFDL-ESM2M and ERA-Interim reanalysis data during 1979 to 2014. GFDL-ESM2M performs reasonably well in the summertime low-level wind circulation in Asia, e.g. over the Indian Ocean and Central China. However, the model tends to give low-level easterlies instead of westerlies in the South China Sea, in relation to its tropical easterlies being too strong over the western Pacific.
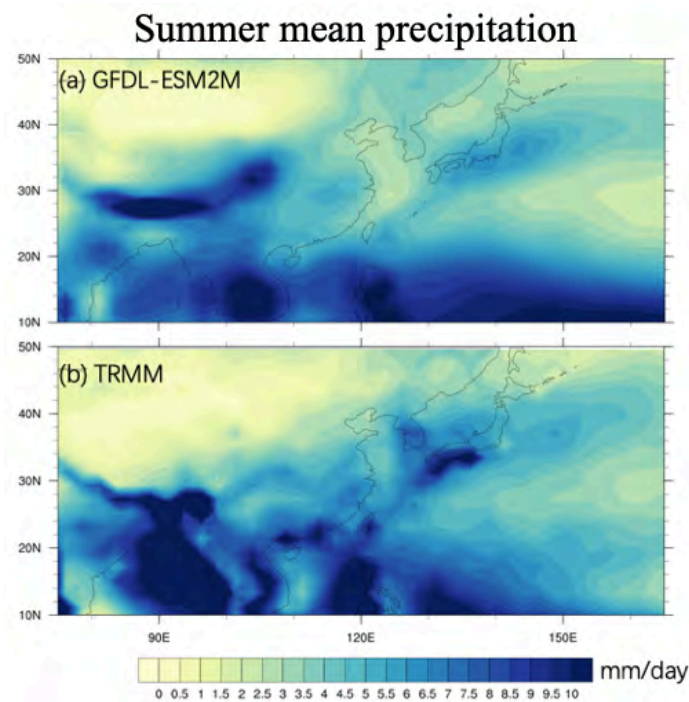
Figure 2.1 *Horizontal distribution of summer mean (MJJAS) precipitation over South Asia (10-50N, 75-165E) from GFDL-ESM2M simulations and TRMM-V3B42 reanalysis data during 1998 to 2013.*

850hPa wind
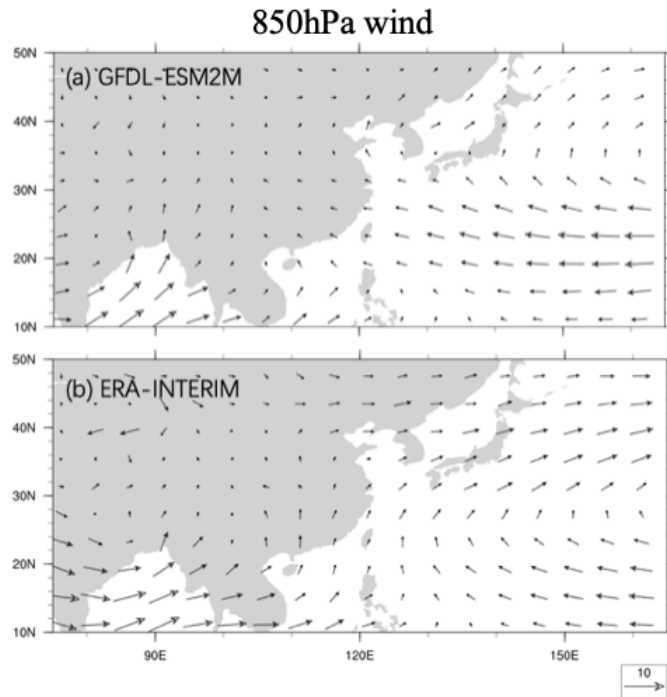
Figure 2.2 *Horizontal distribution of 850Pa summer seasonal mean (MJJAS) wind over South Asia (10-50N, 75-165E) from GFDL-ESM2M simulations and ERA-Interim reanalysis data during 1979 to 2014.*

To summarize the model's performances in difference circulation variables, Figure 2.3 shows the summer mean (MJJAS) temperature from GFDL-ESM2M simulations and ERA-Interim in the levels of 1000hPa, 850hPa, 500hPa and 250hPa over East Asia (10-50N, 75-165E). Compared with ERA-Interim, the temperature over East Asia region from the model has cold biases at almost all layers. In particular, there is moderate cold bias in the low levels and also near 250hPa, but bias becomes stronger at 500hPa.
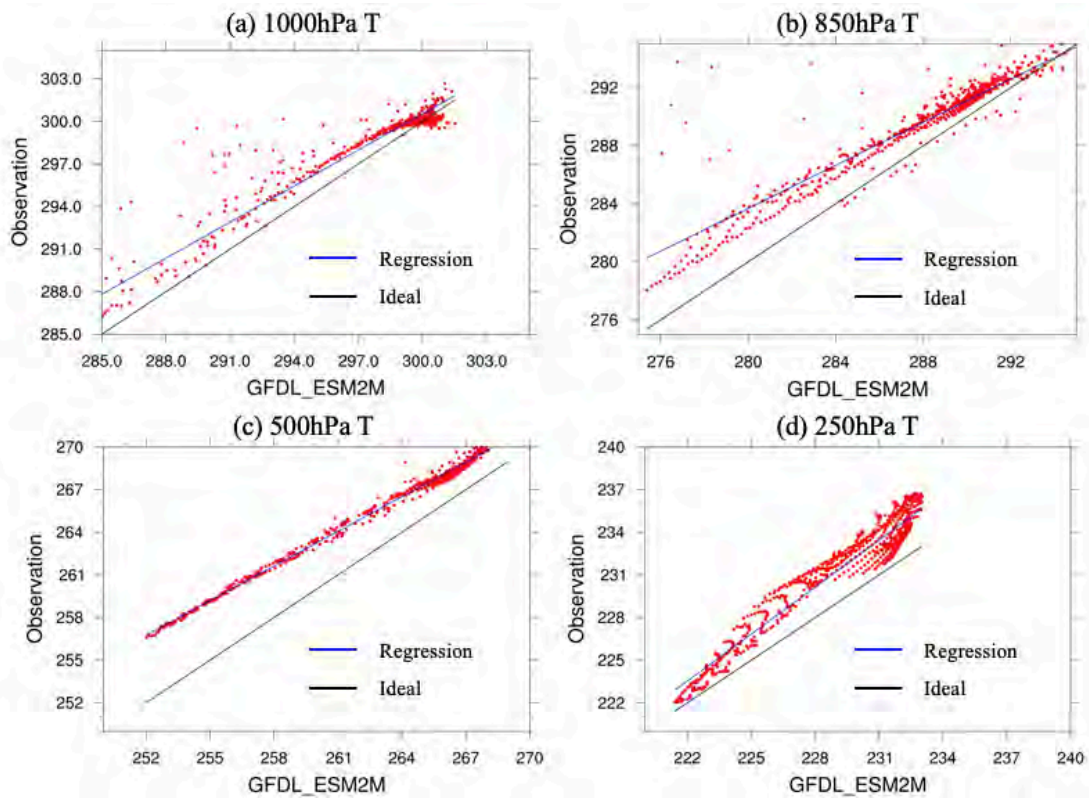
Figure 2.3 *Bias scatter plot of summer seasonal mean (MJJAS, during 1979 to 2014) temperature over East Asia (10-50N, 75-165E) between GFDL-ESM2M simulations and ERA-Interim reanalysis data in the level of (a) 1000hPa, (b) 850hPa, (c) 500hPa and (d) 250hPa.*

Figure 2.4 compares the zonal wind from the GFDL-ESM2M simulations with ERA-Interim over the same East Asia region. It can be seen that the model slightly overestimates both easterlies and westerlies in the layer of 1000hPa and 850hPa. Figure 2.5 shows the same plots but for summer V wind over East Asia region. The performance of model is good in the low levels, but gives stronger wind speed above 500hPa. Overall, GFDL-ESM2M has a reasonable performance in simulating the circulation in the East Asia region, albeit with an underestimated mid-to-upper troposphere temperature.
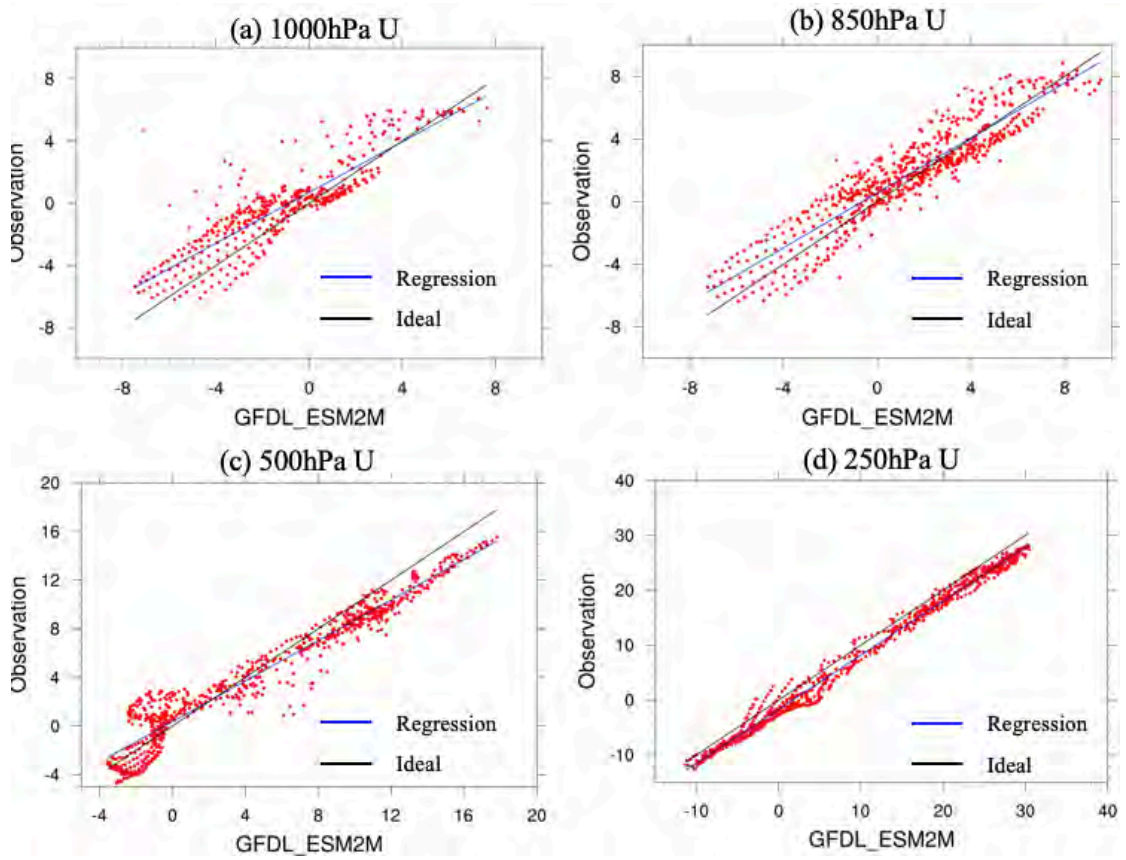
Figure 2.4 *Same as Figure 2.3 but for MJJAS mean U wind.*
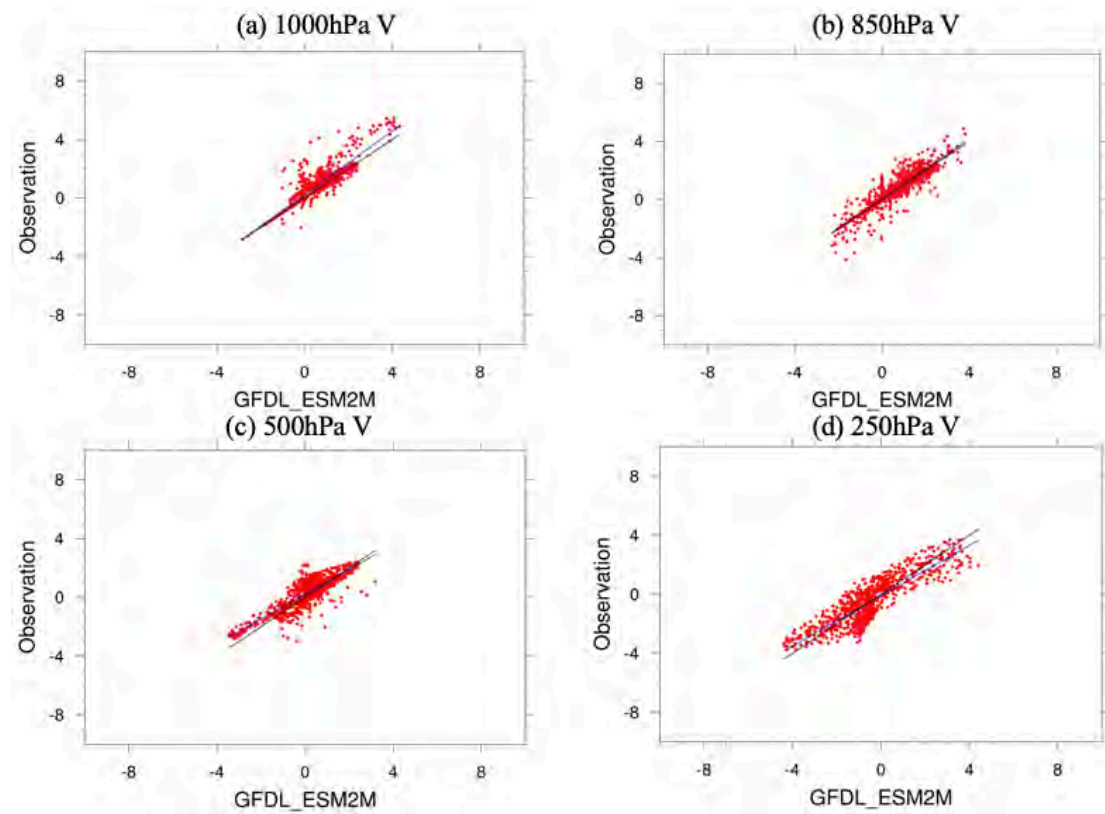
Figure 2.5 *Same as Figure 2.3 but for V wind.*

2.4 MODIS and WUDAPT

Land use categorization used in WRF is based on the Moderate Resolution Imaging Spectro-radiometer (MODIS) data and the World Urban Database and Access Portal Tools (WUDAPT) (for urban areas only). MODIS land cover data is derived from the Terra and Aqua satellites, and is classified according to the International Geosphere-Biosphere Programme (IGBP) Land Cover Type Classification. It consists of 17 types of land cover: Water, Evergreen Needleleaf Forest, Evergreen Broadleaf Forest, Deciduous Needleleaf Forest, Deciduous Broadleaf Forest, Mixed Forest, Closed Shrublands, Open Shrublands, Woody Savannas, Savannas, Grasslands, Permanent Wetlands, Croplands, Urban and Built-up, Natural Vegetation Mosaic, Snow and Ice, and Barren. In the first part of this study (see Chapter 3), the 2004 MODIS land use data is utilized, which is the default land cover in the WRF version 3.8.1.

WUDAPT is an initiative which collect land cover information of city around the world (Mills et al., 2015). It is also an efficient land use producing data tool for meso-scale models (Ching et al., 2018). The Local Climate Zone (LCZ) classification framework (Bechtel et al., 2015) is used for consistently characterizing urban and non-urban land use in WUDAPT. In this framework, land areas can be classified into 17 LCZs based on parameters like building height and density, vegetation cover (Steward and Oke, 2012) (see Figure 2.6), with 10 types for urban land use (Compact

High-rise, Compact Mid-rise, Compact Low-rise, Open High-rise, Open Mid-rise, Open Low-rise, Lightweight Low-rise, Large Low-rise, Sparsely Built, Heavy Industry), and 7 types for natural land use (Dense Trees, Scattered Trees, Bush and Scrub, Low Plants, Bare Rock or Paved, Bare Soil or Sand, and Water). This framework also provides parameters needed in model such as surface albedo, and other thermal parameters of difference LCZs (Stewart et al., 2014). In part 2 (see Chapter 4), PRD land use categories for 1999 and those for 2030 are provided as inputs for the use of WRF simulations. Here, the 2030's (or near-future) urban land use is projected based on the Cellular Automata (CA) land use/land cover change (LCLUC) model (Huang et al., 2019). By using this method, 2030 LCZ maps in the PRD region are forecasted, which are then used as inputs to investigate the impact of both urban development and climate change on extreme rainfall.
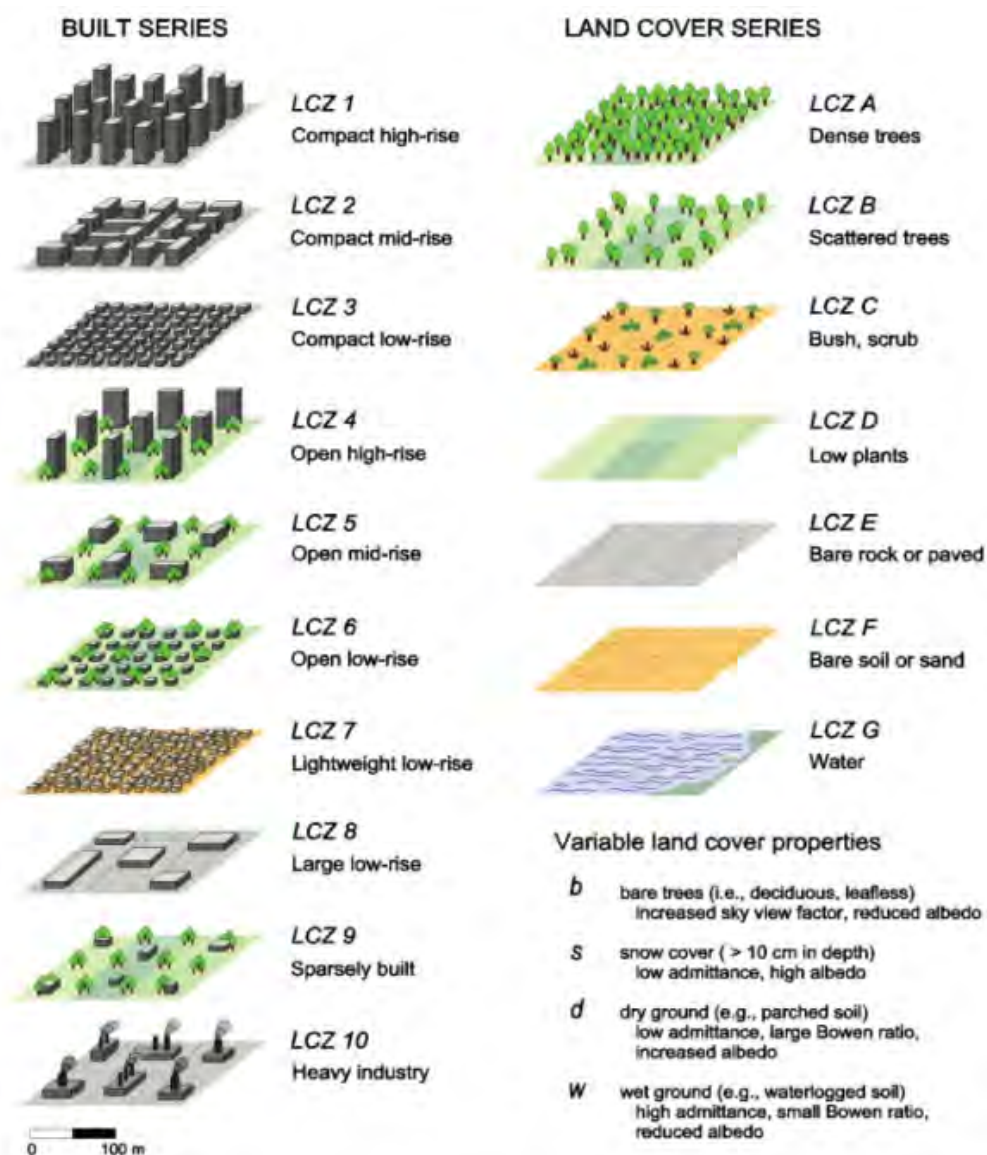
Figure 2.6 *Land cover types from WUDAPT data, with LCZ 1 to 10 representing urban land use and LCZ A to G representing non-urban land use. (Source: Steward and Oke, 2012)*

2.5 Case selection

The extreme rainfall cases to be downscaled are identified based on daily mean rainfall outputs from GFDL-ESM2M. In part 1, daily precipitation averaged over the region of 17-27N, 105-117E from GFDL-ESM2M historical run (1946-2005) was first computed in GCM data by Fung (2018). Figure 2.7 shows the

abovementioned selection region chosen by Fung (2018) for part 1. Days during which the daily mean rainfall is larger than the 99th percentile (based on rainfall in wet days, in which rain rate > 0.1mm/day) are defined as extreme rain days. 110 cases are found from the historical run, with 75% found in the MJJAS season. Around 60 cases are randomly selected from these cases, and are then dynamically downscaled by WRF with a 2km*2km resolution. Only those give rainfall patterns consistent with the GFDL-ESM2M run are considered. Finally, 26 non-TC cases are further downscaled to 2-km resolution over PRD region (see section 2.5). Each integration begins (ends) 72 hours prior to (after) the identified extreme rain day.

For part 2, only rainfall over land area within 17-27N, 105-117E is considered while selecting extreme cases, using the same method for both the historical (1946-2005) and RCP8.5 near-future simulations (2006-2050) from GFDM-ESM2M (see Figure 2.7b). 30 non-TC extreme cases are selected, for both historical and near-future runs. Because the time period of cases in part 1 exceed the extreme rainfall events, integration by WRF starts (ends) only 48hours prior to (after) the extreme rain day for these cases.
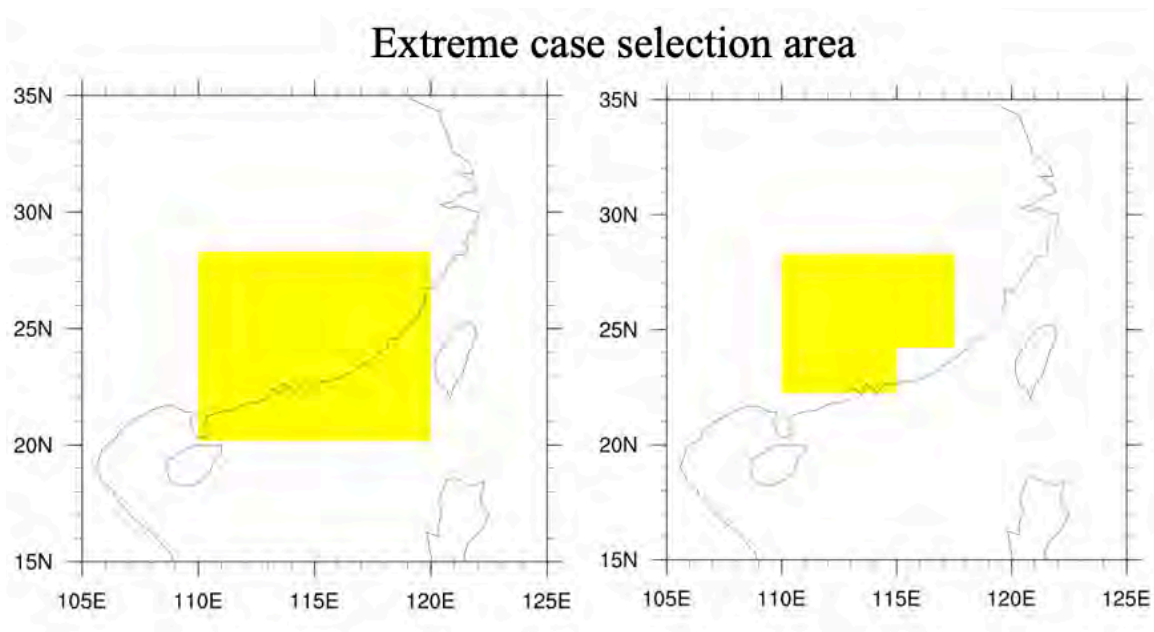
Figure 2.7 *Extreme rainfall case selection area in South-Eastern China (17-27ᵒN, 105-117ᵒE) based on (a) all grid boxes in the domain, and (b) land grid boxes only.*

2.6 Experiments designs

In part 1, three sets of parallel numerical experiments are carried out for examining the sensitivity of extreme rainfall to urban land use and urban parameters over PRD. In experiment 1 (referred to as NO-URBAN), the PRD urban area is replaced by "cropland" in the land use categorization when running WRF. To simulate the urban effect, WRF is coupled with a single layer for the urban canopy (Kusaka and Kimura, 2004) and can simulate the micro-scale meteorology within and above the urban area. The single layer urban canopy model (SLUCM) has parameterization of urban building effect, which can simulate energy exchange between surface and atmosphere, estimate temperature from roof, wall and road (Kusaka et al., 2001). Experiment 2 and 3 (referred to as AH0 and AH300, respectively) utilize the SLUCM

to capture the effect of highly urbanized locations in PRD. According to satellite measurements, a 289W m^{-2} diurnal peak in AH was found in Hong Kong during summer (Wong et al., 2015). Accordingly, the AH diurnal peak is set to zero and 300W m^{-2}, for AH0 and AH300 experiments respectively. Moreover, a diurnal profile with maximum AH at 0 am and 9 am, and minimum at 8 pm local time is adopted in SLUCM (Holst et al., 2016). Results of downscaling experiments AH0 and AH300 are provided by Fung (2018). There are also three sets of parallel experiments in part 2 to investigate the impact of urban development expansion and near-future climate change on PRD extreme rainfall. WRF integrations with 1999 land use under present climate conditions, with 1999 land use under future climate conditions, and 2030 land use under future climate conditions are referred to as 1999LS-HIS, 1999LS-FUT and 2030LS-FUT respectively. Overall, there are 6 numerical experiments in this research; see Table 1 for details of the experiments.

part 1	NO-URBAN	AH0	AH300
GCM DATA (GFDL-ESM2M)	26 cases in 1946-2005	26 cases in 1946-2005	26 cases in 1946-2005
LANDUSE	Urban replaced by cropland	Urban with no AH	Urban with 300Wm^{-2} AH (diurnal max)

part 2	1999LS-HIS	1999LS-FUT	2030LS-FUT
GCM DATA (GFDL-ESM2M)	30 cases in 1950-1999 (His.)	30 cases in 2000-2050 (RCP8.5)	30 cases in 2000-2050 (RCP8.5)
LANDUSE	1999	1999	2030

Table 1 *Experiment design for part 1 and part 2 of this study*

2.7 Dynamical downscaling of extreme rainfall cases

2.7.1 Configuration of WRF

2.7.1.1 Model domains and physics

By using the Weather Research and Forecasting model version 3.8.1 with Advanced Research WRF (ARW) dynamic core (Skamarock et al. 2008) coupled with the single layer urban canopy model (SLUCM) (Kusaka and Kimura, 2004), dynamical downscaling experiments are conducted with a focus on the PRD region. The WRF model with Advanced Research WRF (ARW) dynamic core version 3.8.1 is a non-hydrostatic model, developed by the National Center for Atmospheric Research (NCAR) of National Centers for Environmental Prediction (NCEP) National Oceanic and Atmospheric Administration (NOAA) and other laboratories. Due to its tremendous flexibility, operability, and the broad range of options for different physical processes, WRF is often utilized as community mesoscale model for weather forecasting and region climate analysis study (Skamarock et al. 2008).

Here, 3 nested domains are used for the dynamical downscaling experiments with one-way nesting adopted. Figure 2.8a shows the nested domains for the WRF simulations, with domain 1 (50km x 50km resolution, 129x89 grids in the zonal and meridional direction, respectively, in time steps of 90 s), domain 2 (10km x 10km resolution, 70x80 grids in the zonal and meridional direction, respectively, in time steps of 18 s) and domain 3 (2km x 2km resolution, and 130x130 grids in the zonal and meridional direction, respectively, in time steps of 3.5 s) covers the East Asia/western North Pacific area (2.23-43.82N, 70.81-147.05E), South China (19.94-27.09N, 110.68-117.60E) and PRD (21.5-23.83N, 112.51-115.04E),

respectively. These domains are chosen based on the following considerations (1) to avoid the error results caused by cross-cutting steep relief; (2) to keep the target region at the center of the domain and decrease the influence of boundaries. In each domain, the relaxation zone has a width of 4 grids boxes and results in these zones are not considered. Finally, there are 39 vertical levels, reaching the height of ~ 23km. See Table 2 for the detailed configuration and model setting.

Domains	D01	D02	D03
Resolution	50km	10km	2km
Time interval	180s	36s	7s
Number of grids	(129,89)	(70,80)	(130,130)
Domain coverage	2.23-43.82N, 70.81-147.05E	19.94-27.09N, 110.68-117.60E	21.50-23.83N, 112.51-115.04E
Vertical layers	39layers		
Soil layers	4layers		
TIME	5-9 days		

Table 2 WRF configuration for 3 domains.

Physical parameterizations used in this WRF setting include the Rapid Radiative Transfer Model for General Circulation Model (RRTMG) for the longwave radiation (Iacono et al. 2008), Dudhia short wave scheme (Dudhia 1989), WRF single-moment 6-class microphysics scheme (Hong et al. 2006), Eta Similarity similarity theory for the surface layer options (Janjic et al. 2002), unified Noah land-surface model (LSM), which supports SLUCM (Chen and Dudhia, 2001; Tewari et al. 2004), Bougeault and Lacarrere planetary boundary layer (PBL) scheme (Bougeault et al. 1989), and the simplified Arakawa-Schubert (SAS) GFS cumulus parameterization (for the outermost domain only; Han and Pan 2011). By not using cumulus schemes in domain 2 and 3, the discontinuity between simulations in the two domains can be reduced. Various boundary layer options have been tested by Fung

(2018), who found that only BouLac PBL gave stable solutions for all cases. On the other hand, unstable solutions were found for some extreme rainfall cases using the PBL scheme of Mellor-Yamada-Janjic. Table 3 shows the details about physical parameterization schemes used in this WRF configuration.

Domains	d01	d02	d03
ra_lw_physics	RRTMG		
ra_sw_physics	Dudhia		
mp_physics	WSM 6-class scheme		
sf_surface_physcis	Unified Noah land-surface model		
sf_urban_physics	Single layer Urban Canopy Model		
bl_pbl_physics	BouLac PBL		
cu_physics	Old SAS	Turn off	Turn off
Spectral nudging	U,V-wind(500hpa or above and ~1300km wavelength) (only d01)		

Table 3 Model physical parameterization schemes in WRF for 3 domains.

In part 1 of this study, land use information adopted is taken from the 2004 MODIS data. Figure 2.8b gives the land use categories within domain 3 such as Forest (green shading in Figure 2.8b), Grasslands (cyan), Croplands (yellow), Urban and Built-up (red), and Water bodies (blue), also shown are the locations of major cities in PRD, namely, Hong Kong, Shenzhen, Dongguan, Guangzhou, Foshan, Zhongshan, Zhuhai, and Macao (see black dots). Within the inner-most domain, over grids categorized as urban and built-up, SLUCM is used for parameterizing urban effects in the model environment. The SLUCM can incorporate three types of urban categories, (1) "Low Intensity Residence", representing a mixture of constructed materials and vegetations, and mainly including single-family housing units with low

population density; (2) "High Intensity Residence", representing highly developed areas with people residing in high numbers, (3) "Commercial and Industrial", representing infrastructure and highly developed areas. Due to lack of data in MODIS, all urban grid points are categorized as to High Intensity Residence, with albedo of 0.15 and surface emissivity of 0.88. Standard land use information was adopted in experiment AH0 and AH300. Figure 2.8c shows the land use distribution after replacing the urban area by cropland in the innermost domain. Such land use information will be adopted in WRF in the NO-URBAN experiment.
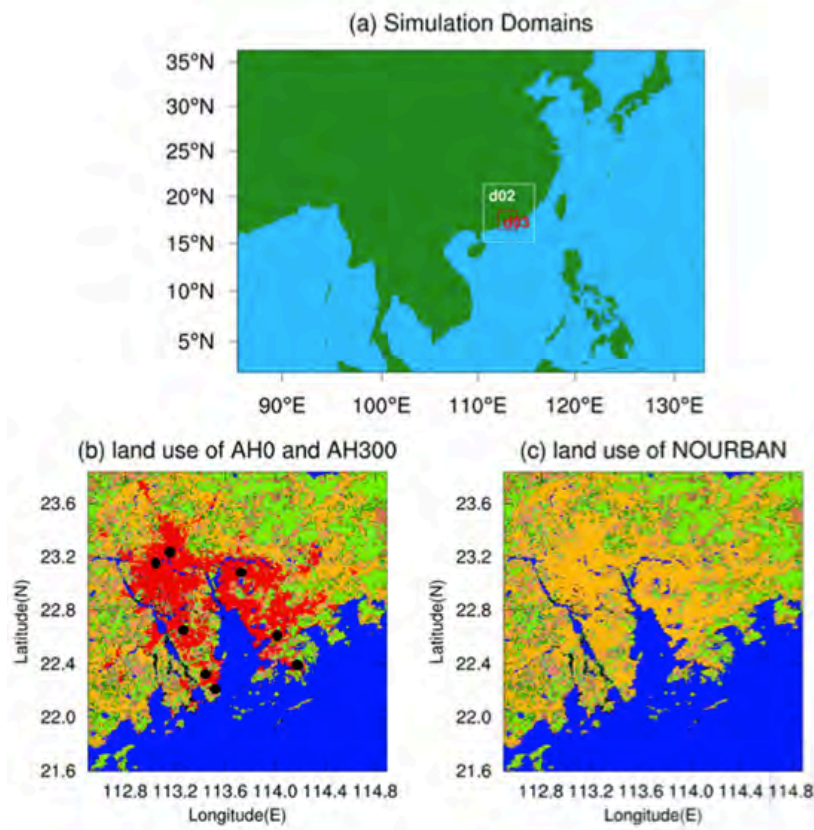
Figure 2.8 (a) Nested domains for the WRF simulations. (b) Land use categories in domain3 for AH0 and AH300 experiments, based on 2004 MODIS data with urban and build-up shown areas in red. Also shown are the location of major cities in the PRD (counterclockwise from lower right): Hong Kong (HK), Shenzhen (SZ),

Dongguan (DG), Guangzhou (GZ), Foshan (FS), Zhongshan (ZS), Zhuhai (ZH) and Macao (MC). See text for details. (c) Land use categories for the NOURBAN experiment, in which urban and build-up areas are replaced by cropland.

For numerical experiments in part 2, the domains are the same as those for part 1, but different urban land use data are adopted in the model environment. The land use information is based on WUDAPT which gives 17 LCZs in the PRD region at 50m resolution, comprising 10 types of urban and 7 types of non-urban land use. To incorporate the land use information into the UCM setting, WUDAPT urban data are aggregated to 2km*2km resolution and regrouped into three urban types. In particular, Open Mid Rise, Open Low Rise, Sparsely Built, Open High Rise, Lightweight Low Rise, Large Low Rise are grouped as "low Intensity Residence" (type 1). Compact Mid Rise; Compact Low Rise are grouped as "High Intensity Residence" (type 2). Finally, Compact High Rise and Heavy Industry are grouped as "Commercial and Industrial" (type 3). For non-urban land use, MODIS data is adopted in WRF. Figure 2.9 shows the urban distribution of 1999 (based on WUDAPT) and 2030 in the innermost domain.

The 2030 urban distribution was simulated by Huang with the Cellular Automata (CA) land use/land cover change (LCLUC) model. In that study, Huang et al. utilized the Geographical Simulation and Optimization System (GeoSOS) – the Future Land Use Simulation (FLUS) model (Liu et al., 2017) to predict reasonable future land use interactions and changes. For discovering the probability of occurrence of land use changes from the current LCZ, the Artificial Neural Network

(ANN) was applied, which is a data mining technique. Then, to predict the demand of future society, the trends of LCLUC with socioeconomic developments are analyzed and extrapolated. Finally, the CA model is utilized to simulate LULCC change and generate the future land use map based on the probability of occurrence and neighborhood influences, until future demands are met. Moreover, the model accuracy was examined by comparing the predicted 2014 PRD LCZ (based on maps in 2009) with the observed one in 2014.

Based on the CA model projection, the urban fraction in PRD will expand significantly, especially for the low-intensity residence category. Overall, the urban area will expand by more than 2.5 times in PRD in 2030 compared with 1999. It is also clear that part of the urban area will become even more developed, e.g. some locations labeled as Low Intensity Residence will become High Intensity or Commercial Industrial in the future. The PRD urban area will also become more "connected" in 2030, and this change may have significant influence on the local urban climate.
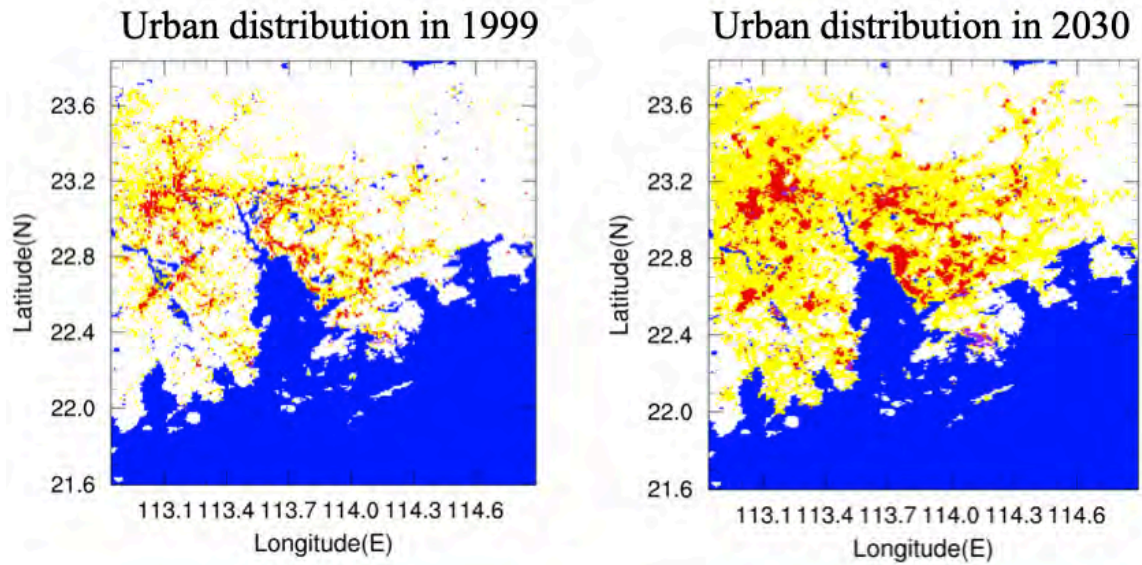
Figure 2.9 *(a) Urban distribution in 1999 PRD region from WUDAPT data for WRF-UCM simulation. (b) Same as (a) but for 2030 PRD urban distribution.*

2.7.1.2 UCM set up

To simulate the heat flux transport, momentum exchange and water vapor over the urban area in the meso-scale model, the SLUCM is utilized in the study. The SLUCM gives parameterization of buildings, which has a 3-dimensional radiation treatment including the canyon orientation and diurnal change of the azimuth angle (Tewari et al., 2008). The SLUCM includes parameters in building height, standard deviation of roof height, roof width, road width, AH, AH diurnal profile, urban fraction, heat capacity of roof, building wall, and road, etc. See Table 4 for details.

Parameter	Unit
Building height	m
Standard Deviation of roof height	m
Roof width	m
Road width	m
Anthropogenic heat	$W\ m^{-2}$
Anthropogenic heating diurnal profile	Fraction
Fraction of the urban	Fraction
Heat capacity of roof	$J\ m^{-3}\ K^{-1}$
Heat capacity of building wall	$J\ m^{-3}\ K^{-1}$
Heat capacity of road	$J\ m^{-3}\ K^{-1}$
Thermal conductivity of roof	$J\ m^{-1}\ s^{-1}\ K^{-1}$
Thermal conductivity of building wall	$J\ m^{-1}\ s^{-1}\ K^{-1}$
Thermal conductivity of road	$J\ m^{-1}\ s^{-1}\ K^{-1}$
Surface albedo of roof	Fraction
Surface albedo of building wall	Fraction
Surface albedo of road	Fraction
Surface emissivity of roof	-
Surface emissivity of building wall	-
Surface emissivity of road	-

Table 4 Parameters required in SLUCM.

For part 1, the mean building height is set to 30m (based on data from the Hong Kong Lands Department). The standard deviation of building height is 4m, and the road width is 16m, which are the default values for commercial land use. As mentioned in section 2.6, a diurnal profile of AH with a maximum of 300W m^{-2} at 9 am and 4 pm local time (see Figure 2.10) is adopted (Holst et al., 2016).

Diurnal profile of AH
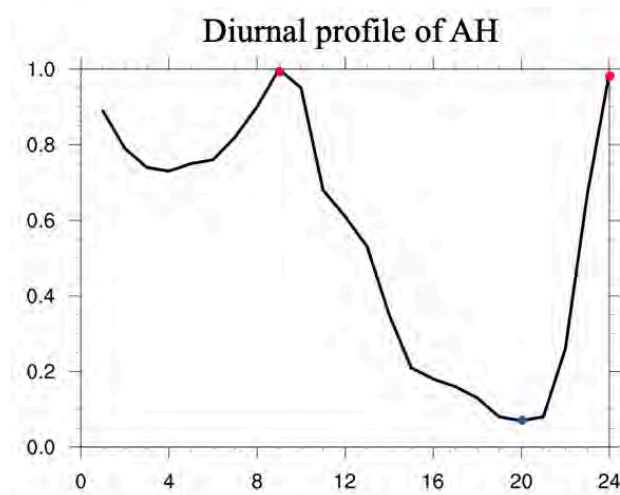
Figure 2.10 *Diurnal profile of AH over urban grids of innermost domain for experiments with peak AH = 300Wm^{-2}, the daily mean AH is about 166Wm^{-2}.*

For the WRF simulation in part 2, WUDAPT data for urban area are regrouped to 3 types (see section 2.3). Table 5 shows some of the surface properties parameters of these three urban types in the PRD region. For instance, the building height for "Low-Intensity Residence", "High-Intensity Residence", and "Industrial and Commercial" are 13.31m, 14.01m, and 53.92m, respectively. See Table 5 for some value of the UCM parameters used.

UCM parameter	Type1	Type2	Type3
Anthropogenic heat [W m^{-2}]	15.0	50.0	200.0
Building height [m]	13.31	14.01	53.92
Urban fraction	0.4	0.9	0.7
Standard Deviation of roof height [m]	10.42	5.64	33.18
Roof width [m]	38.01	14.28	35.5

Table 5 *Parameters in SLUCM for three types of urban.*

2.7.2   Dynamical downscaling and spectral nudging

To carry out the dynamical downscaling experiments, boundary data for U- and V- wind, relative humidity, air temperature, air pressure (with 6 hour resolution), near-surface wind, near-surface specific humidity and near-surface temperature (with 3 hour resolution) variables from the GFDL-ESM2M historical and RCP8.5 simulation are used. To avoid inconsistent land surface conditions between WRF and the GCM, other surface and soil parameters such as daily mean sea surface temperature, monthly mean soil water content, soil temperature are also assimilated

by WRF. Moreover, spectral nudging was adopted to ensure consistency between WRF and GCM circulation, which is widely used in meso-scale simulation (Von Storch et al., 2000). Here we followed the method used by Fung et al. (2019), namely that spectral nudging was adopted only in the outmost domain (d01) with 50km*50km resolution with a strength of 3×10^{-4} s for U, V wind only above 500hPa, and at the wavelength of about 1300km.

According to the result of Fung et al. (2019), it was found that WRF outputs could not capture the intensity of the peak rainfall of original GFDL-ESM2M data over eastern China without nudging, and nudging perturbing geopotential height or water vapor have no effect on the intensity of precipitation. Nudging multiple variables also could not enhance the accuracy of rainfall outputs, and only larger scale circulation should be nudged for the maximum freedom in WRF system. Typical nudging coefficient representing the strength for wind is 3×10^{-4} s^{-1} (Otte and Gilliam, 2007), and this value is considered reasonable while spectral nudging is only adopted in outermost domain.

Chapter3

3 Sensitivity of extreme rainfall to the presence of megacity and urban parameters in the PRD area

3.1 Surface temperature

In this part of the study, how extreme local rainfall might be influenced by the presence of megacity as well as the AH flux are investigated by downscaling output from GFDL-ESM2M using WRF-UCM. After the modification of land use in the PRD area, properties of land surface will also be changed in the model environment of WRF-UCM. Figure 3.1a shows the surface albedo difference between AH0 and NO-URBAN in the innermost model domain. In the NO-URBAN experiment, urban grids are replaced by "cropland" in the model environment. Comparing AH0 with NO-URBAN experiments, the surface albedo decreases by about 0.06 to 0.012 over the original urban area. Figure 3.2 gives the ratio of surface albedo between NO-URBAN and AH0 experiments, and there is a decrease of the surface albedo by about 40% to 45%. Lower surface albedo over the urban area can lead to more absorbed shortwave radiation, and therefore stronger sensible heat flux compared with rural areas. Also shown in Figure 3.1 are the 2m temperature difference between experiments AH0 and NO-URBAN, and also between AH300 and NO-URBAN. It is clear that AH0 experiment gives higher 2m temperature than NO-URBAN over almost the whole urban in PRD region, meaning that the presence of a megacity itself can lead to higher temperature, even if there is no AH released

within the city. The warming magnitude ranges from 0.5 to 2˚C, in the Northern urban area, and the change of 2m temperature can reach 1.5˚C or more. On the other hand, the temperature difference in the surrounding locations is small (no more than 0.5˚C), meaning that the influence of surface properties on the temperature is very localized. Overall, the surface warming is likely caused by the decrease of surface albedo, which can lead to more shortwave radiation received over the megacity area. Also, complex building structures can hold more heat. This can also contribute to warmer temperature within the city.

For the AH300 experiment, Figure 3.1c shows that 2m temperature increases by about 2 to 4˚C compared to NO-URBAN, with more than 3.5˚C warming in northwestern and northeastern parts of the megacity. Noted that the 2m temperature anomaly pattern in Figure 3.1c is similar to that in Figure 3.1b. Finally, the warming due to changes in urban surface properties is only (i.e. difference between NO-URBAN and AH0) about 1.2˚C, while about 1.65˚C is due to the presence of AH (i.e. between AH300 and AH0) in the city area. Thus, the AH heat flux has a stronger effect on the urban surface temperature.
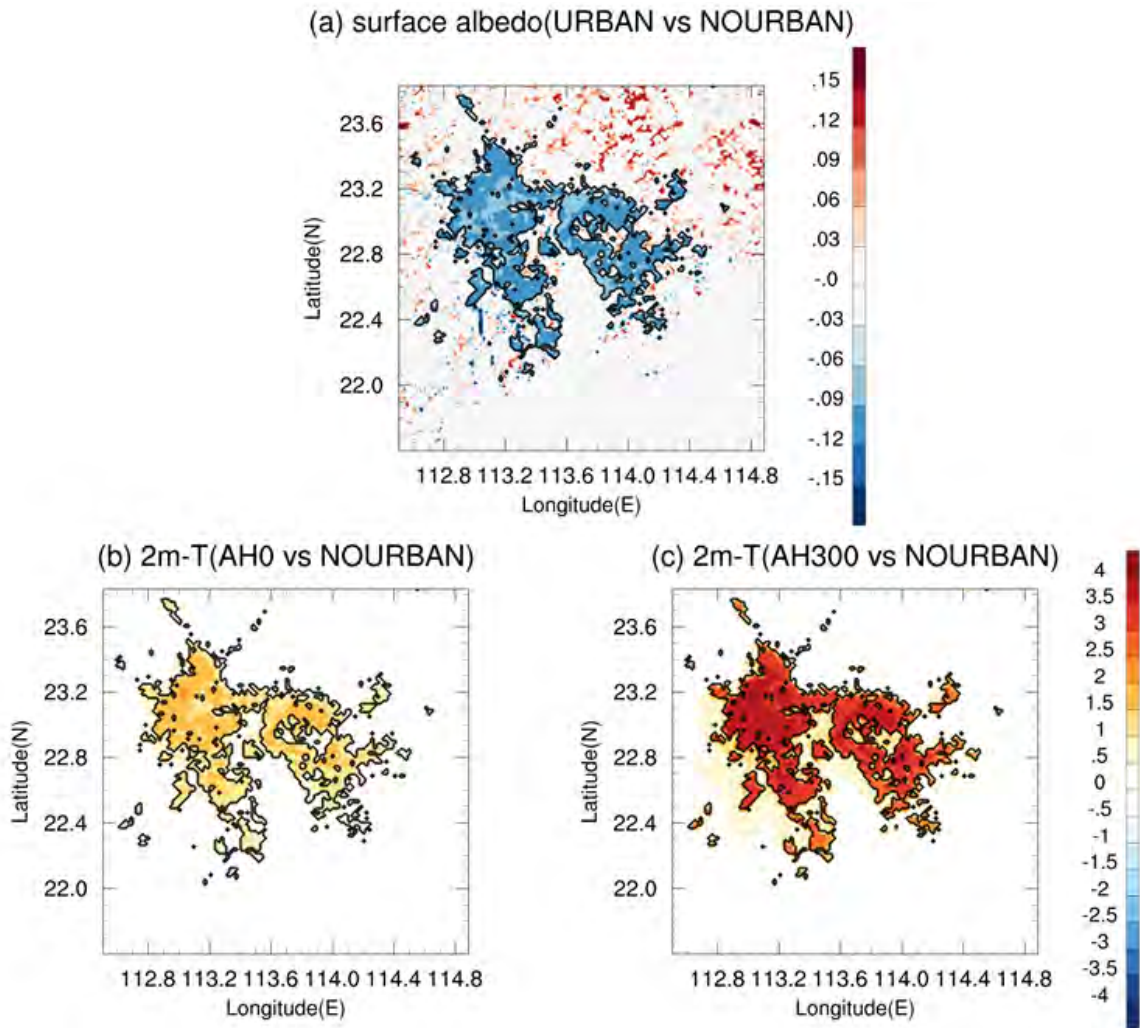
Figure 3.1 *Surface albedo difference between (a) URBAN and NO-URBAN, and 2m temperature difference (units: ˚C) between (b) AH0 and NO-URBAN and (c) AH300 and NO-URBAN. Temperature are computed by averaging over entire integrations for all selected extreme cases. See text for details. The urban area within PRD is outlined by black contours.*
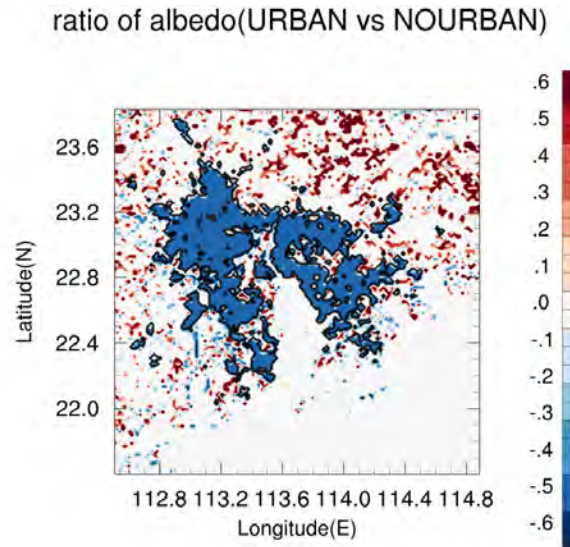
Figure 3.2 *Same as Figure 3.1 except for ratio of surface albedo.*

In addition to 2m temperature, the vertical temperature profiles from the three experiments are also examined. Figure 3.3 shows the temperature differences averaged over the PRD urban area from 200m to 6km above surface. The largest difference between NO-URBAN and the other 2 experiments was found in the lowest 500 to 1000m, with anomaly about 0.3K (0.76K) at 200m for AH0 (AH300). Such warming due to either the surface properties of the city or increased AH was found to decrease with height, with the positive anomaly between AH0 and NO-URBAN vanishing at 0.6km, and that between AH300 and NO-URBAN vanishing at 1.4km. It is obvious that the warming effect due to urbanization has limited vertical extension.
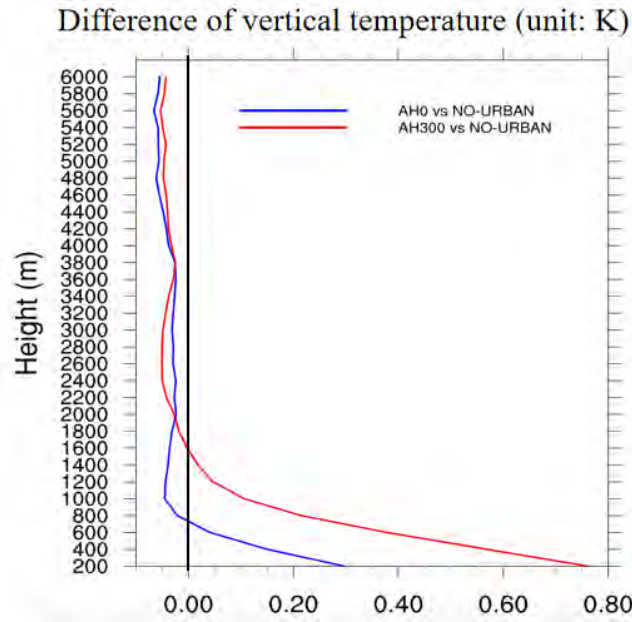
Figure 3.3 *Vertical temperature difference profile averaged over urban grids in d03 between AH0 and NO-URBAN (blue); AH300 and NO-URBAN (red). Temperatures are computed by averaging over entire integrations for all selected extreme cases.*

On the other hand, for AH0 (AH300) experiments at 800m (1600m) of height, the air temperature is actually lower than that in the NO-URBAN experiment. To understand the reason why the temperature has a slight decrease in upper atmosphere, Figure 3.4 gives the difference of upwelling longwave radiation flux at top of the atmosphere between AH0 and NO-URBAN, and also between AH300 and NO-URBAN. Results show that though AH0 and AH300 experiments has higher surface sensible heat flux, the outgoing longwave radiation (OLR) is still reduced over the urban area, especially for the AH300 experiment. There is a decrease of OLR of about 4 to 8W/m^{-2} in the southern part of megacity for AH0 compared with NO-URBAN (see Figure 3.4 a), 2 to 6W/m^{-2} over more inland locations. Such a difference is likely due to that in the cloud fraction in the two experiments. In fact, the

cloud fraction is increased over the central – to south-western part of the domain (see Figure 3.5a). For AH300, there is an obvious decrease of OLR by about 4-10W/m^{-2} over most urban locations, especially in the norther part of megacity (see Figure 3.4 b), which matches well with the pattern of cloud fraction difference (see again Figure 3.5b). Also shown in Figure 3.4 is the difference of upwelling clear sky longwave radiation flux at top of the atmosphere. Both AH0 and AH300 give clear sky upwelling flux which is larger than NO-URBAN, presumably due to higher surface temperature in the former experiments.
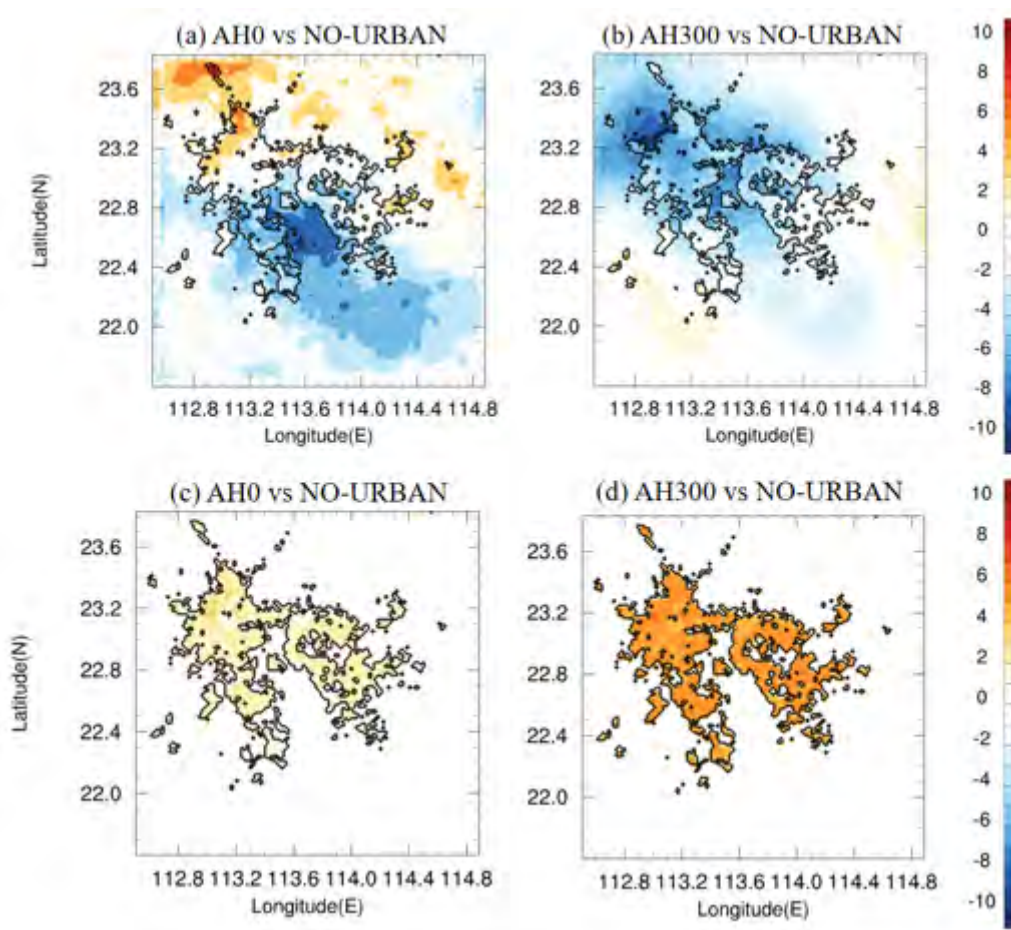
Figure 3.4 *Same as Figure 3.1 except for (a)(b) upwelling longwave radiation flux at top of the atmosphere (units: W/m^{-2}) and (c)(d) upwelling clear sky longwave radiation flux at top at the atmosphere (units: W/m^{-2}).*
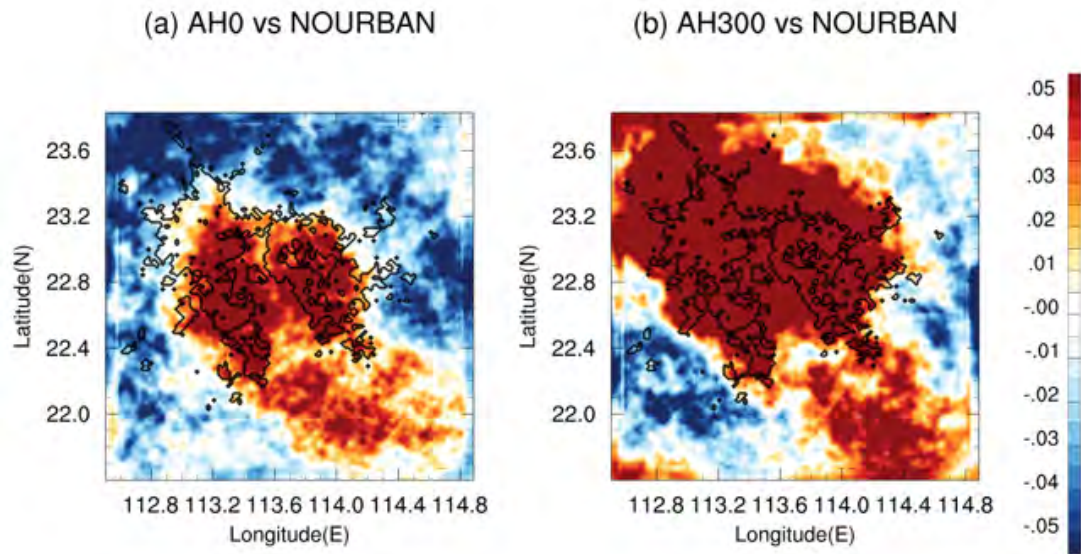
Figure 3.5 *Same as Figure 3.1 except for cloud fraction averaged over all layers (units: %).*

Figure 3.6 gives the vertical profiles of cloud fraction difference between AH0 and NO-URBAN, and also AH300 and NO-URBAN averaged over the urban location. The decrease of surface evaporation caused by the presence of urban surface leads to less water vapor content in the lowest few levels, then result in decreased cloud fraction in either AH0 or AH300. However, the cloud fraction increases at a height of 600m (800m) or more for AH0 (AH300) and NO-URBAN. The increase of relatively high clouds can explain the decreased OLR over the urban area.
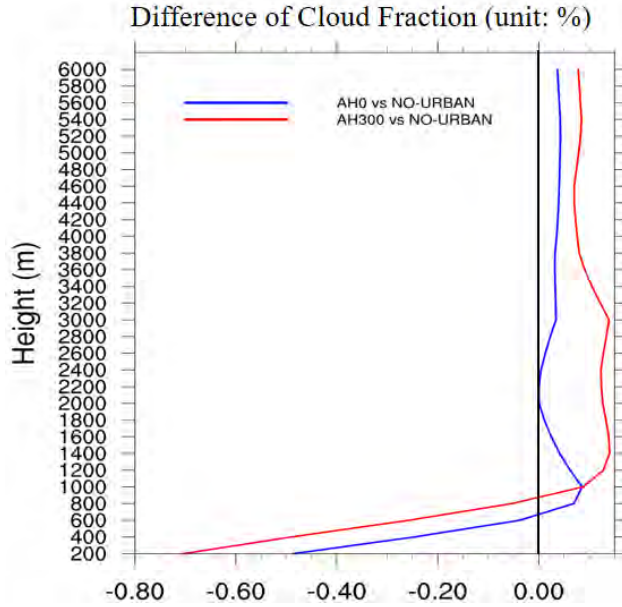
Figure 3.6 *Same as Figure 3.3 except for cloud fraction difference (units: %).*

3.2 Precipitation

To represent extreme rainfall characteristics and the role of urbanization, probability density functions (PDF) of hourly precipitation rates are calculated. PDFs based on hourly rain rate over all urban grids from the three experiments are computed, which counting the number of events in each range (i.e. 1-10mm/hr) divided by the number of whole rainfall events. Figure 3.7a shows the rainfall PDF results for NO-URBAN, AH0, and AH300. Comparing AH300 with NO-URBAN, it is seen that the rainfall probability increases significantly for rain rates larger than 10mm/hr. AH0 also gives higher probability of heavy rainfall compared to NO-URBAN, but the difference is slight (no more than 20% for 10 mm/hr to 100mm/hr). For AH300, the occurrence of 80 to 90mm/hr rain rate is almost 3 times as likely as for the case without a megacity. In general, urbanization can significantly enhance the likelihood of heavy rainfall in the PRD region. Figure 3.7b gives the ratio

of probability of hourly rain rate in the PRD urban area in the range of 1 to 110mm/hr.

It is clear that the impact of urbanization on heavy rainfall (50-110mm/hr) is stronger

than that on light rainfall (1-20mm/hr). The probability of rain rates due to either

replacing cropland with urban land use or stronger AH increases with rainfall

intensity in the range of 1-100mm/hr, with the ratio between AH0 and NO-URBAN

being 1 to 1.5, and that between AH300 and NO-URBAN being 1.25 to 3.
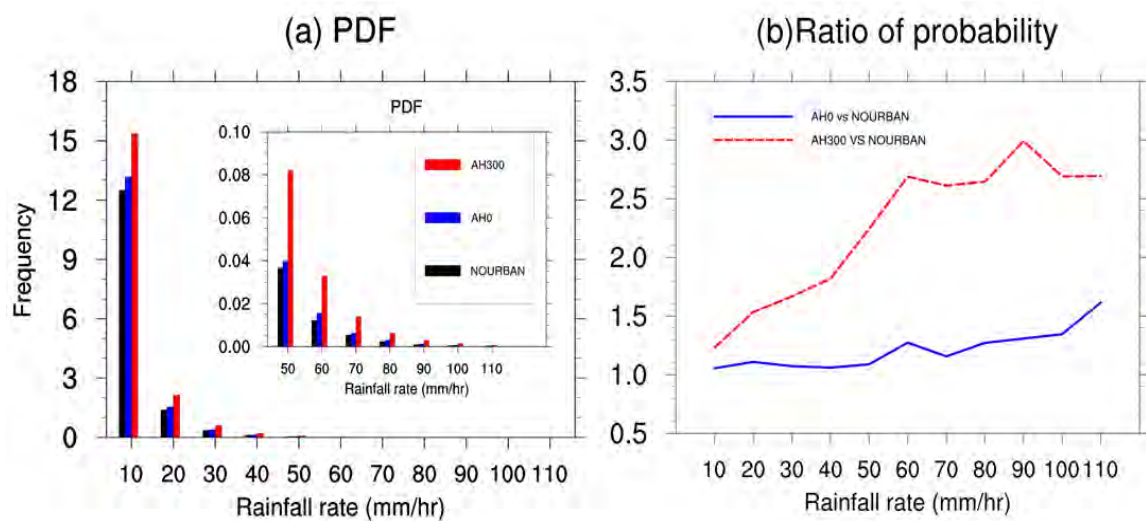
Figure 3.7 (a) PDFs of hourly precipitation rates within the rages of 1-10, 10-20, 20-30, 30-40, 40-50, 50-60, 60-70, 70-80, 80-90, 90-100, and 100-110 mm/hr (denoted by 10, 20, 30, 40, 50, 60, 70, 80, 90, 100, 110mm/h, respectively) for the NO-URBAN (black), AH0 (blue), AH300 (red) experiments over urban locations within PRD. (b) Ratio of the probabilities between AH0 and NO-URBAN (blue), and that between AH300 and NO-URBAN (blue) at different precipitation rates.

Figure 3.8 shows the daily precipitation differences between various

numerical experiments, which are computed by averaging over entire integration

periods for all selected extreme cases. Compared with NO-URBAN (see Figure 3.8a),

accumulated rainfall increases slightly over the city area in the AH0 runs. Daily mean

rainfall is enhanced by 4 to 6 mm/d over the northeastern corner of the megacity, but

otherwise the difference is small (no more than 4 mm/d) over most urban locations.

Moreover, the intensity of rainfall decreases about 4-12 mm/day in some regions such

as east of urban. For the AH300 experiment, there is an increase of rainfall by 8 to 12

mm/d over most urban grids compared with NO-URBAN (see Figure 3.8b), with

maximum increase of about 20 mm/d over the northwestern part of the domain (near

cities of Guangzhou and Foshan). The more intense precipitation over these city areas

appear to be related to the strong warming at the same locations (see Figure 3.1c). In

our models, stronger surface temperature warming related to urbanization tends to

give more rainfall within the PRD megacity.
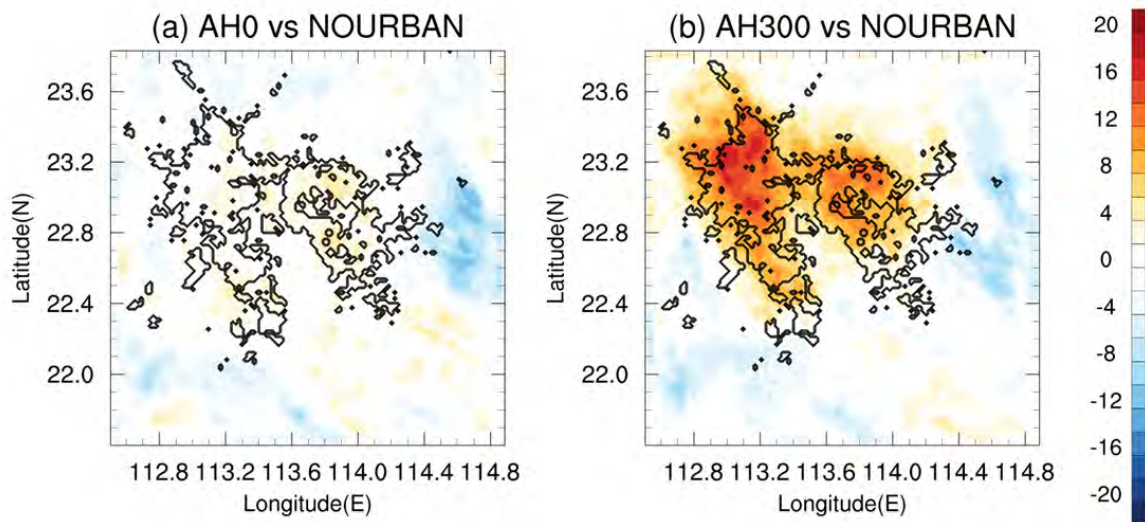
Figure 3.8 *Same as Figure 3.1 except for averaged daily precipitation rates (units: mm/d).*

To further illustrate such a temperature effect, Figure 3.9a shows the scatter

plot of the differences of 2m temperature vs accumulated daily rainfall over urban

grids between AH0 and NO-URBAN, and also those between AH300 and NO-URBAN. For AH0, the surface warming over the city area (compared to NO-URBAN) is weakly related to the rainfall difference. For AH300 experiment, a strong positive relationship between temperature and rainfall difference can be found. However, it is noticed that, for some grids, there are larger increase of rainfall even when the surface warming is small (see red box in Figure 3.9a). Figure 3.9b shows the geographical location of these grids (in red), which are selected if the temperature difference is less than 2°C but with rainfall difference larger than 5mm/day. In fact, these grid boxes are located at the boundary of the urban area. It seems likely that the predominance of urban areas over rural areas is a non-local effect, and is caused by advection of rainfall from the urbanized region in the domain.
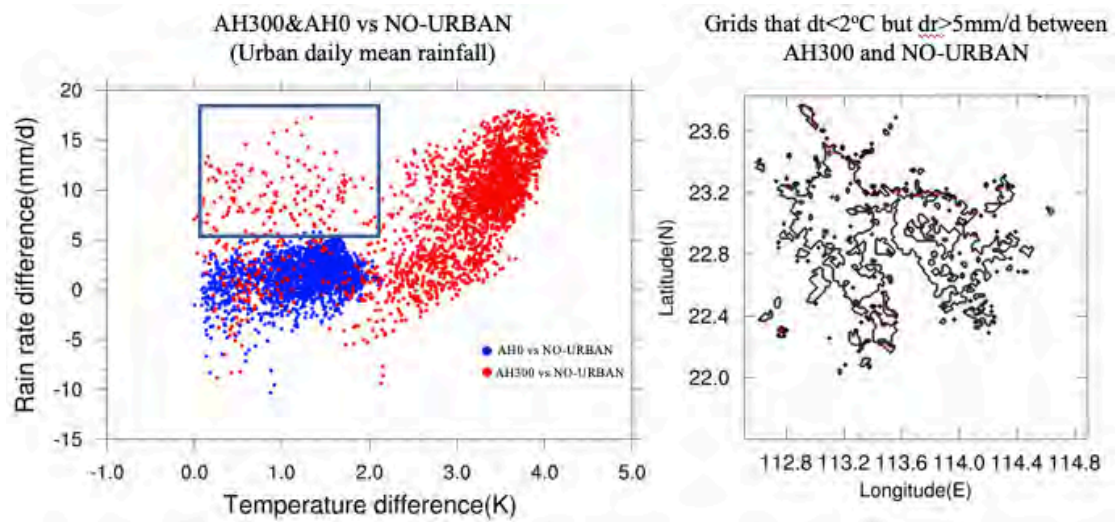
Figure 3.9 *(a) Scatter plot of temperature and daily rainfall difference between AH0 (blue), AH300 (red) and NO-URBAN. (b) Location of grids for temperature difference less than 2°C and rainfall difference larger than 5mm/day between AH300 and NO-URBAN (grids in blue rectangle of Figure 3.9a).*

The relationship between surface warming and extreme rainfall is also examined. Figure 3.10 shows the 2m temperature difference vs extreme rainfall difference, with the extreme rainfall defined as the 95th percentile of hourly rain rate based on the integration periods of all cases considered. Again, there is only a weak relationship between 2m temperature and extreme rainfall difference in AH0 compared to NO-URBAN. For AH300, the change of extreme rainfall intensity and 2m temperature warming is positively correlated, enhanced extreme rain rate can reach 10mm/hr for a 4°C surface warming.
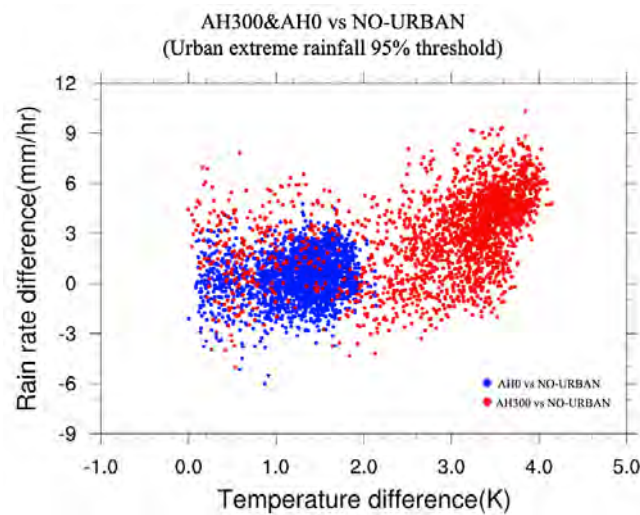
Figure 3.10 *Same as Figure 3.9a except for the extreme rainfall difference based on the 95% threshold of rainfall events (larger than 0.1mm/hr).*

To ascertain the robustness of change of rainfall characteristics, the Student's t-test and the Kolmogorov-Smirnov (K-S) test are applied for the accumulated rainfall difference and rainfall PDFs. Figure 3.11 shows the result of Student's t-test for AH0 vs NO-URBAN, and for AH300 vs NO-URBAN. The difference of accumulated rainfall between AH0 and NO-URBAN experiments do not pass the 95% significance

level in the PRD region (see Figure 3.11a), meaning that the increase of accumulated rainfall by modifying the land use from "cropland" to "urban" is slight and insignificant. On the other hand, for the AH300 experiment, Student's t-test indicate that almost the whole northern urban area show robust changes in accumulated rainfall compared to NO-URBAN (see Figure 3.11b); such significant signals are consistent with the stronger warming in the same region due to urbanization (see Figure 3.1c). This suggests that urbanization can enhance rainfall if there is strong warming over the urban area.
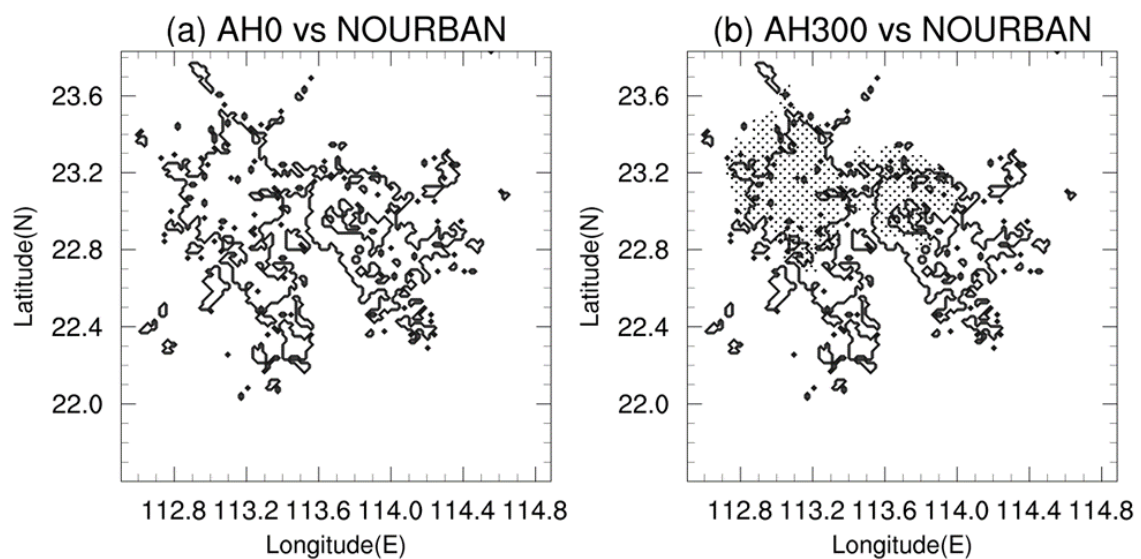
Figure 3.11 *Results of Student's t-test of daily mean rainfall difference between (a) AH0 and NO-URBAN, (b) AH300 and NO-URBAN. Locations in which the difference exceeds the 95% significance levels are denoted by black dots. The urban area within PRD is outlined by black contours.*

For the K-S test, results show that there are only a few locations in which the AH0 hourly rain rate in PRD is significantly different from that for NO-URBAB (see

Figure 3.12a). On the other hand, comparing AH300 with NO-URBAN, PDFs of the

two experiments are distinct from each other at the 95% confidence level in most part

of the urban area (see Figure 3.12b). Therefore, when considering both the effects of

urban land use and AH, the rainfall PDFs can be significantly modified by the

warming effect of urbanization.
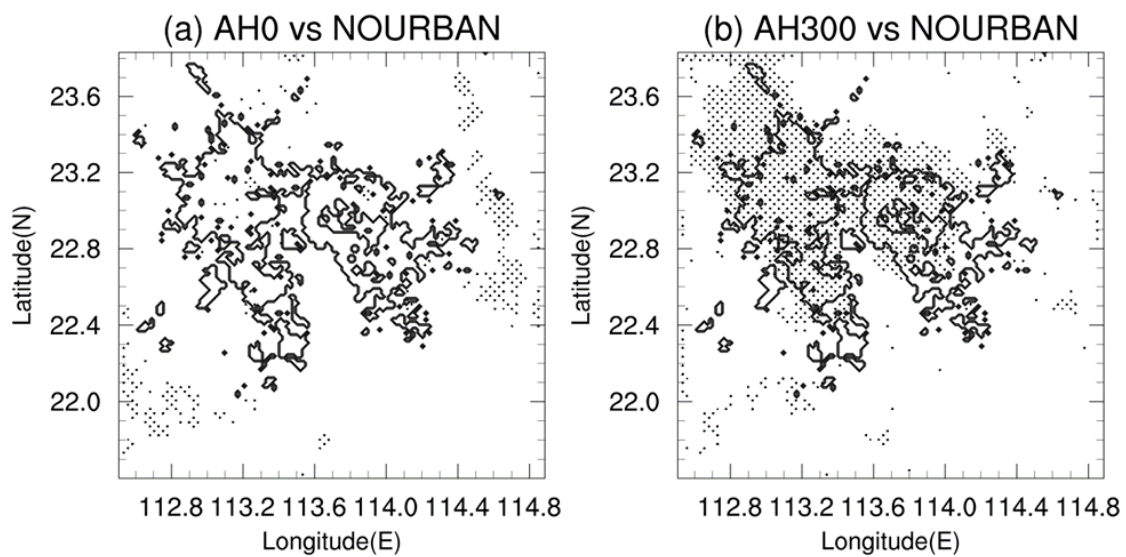
Figure 3.12 *Same as Figure 3.11 except for results of the K-S test on the difference of PDFs of hourly precipitation rates.*

3.3 Convective instability and moisture transport

Physically, building materials such as cement and concrete have lower

permeability to water vapor, thus reducing evapotranspiration, leading to lower

surface humidity in the urban area while compared to cropland. Figure 3.13 shows the

difference of surface evaporation between AH0 and NO-URBAN, and also between

AH300 and NO-URBAN in the PRD region. It is clear that the change from cropland

to urban surface can lead to a decrease of surface evaporation around 0.012 to 0.024 $g \cdot m^{-2} \cdot s^{-2}$ over the whole urban area, meaning that there is less water vapor available over the urban surface.

(a) AH0 vs NOURBAN   **(b) AH300 vs NOURBAN**
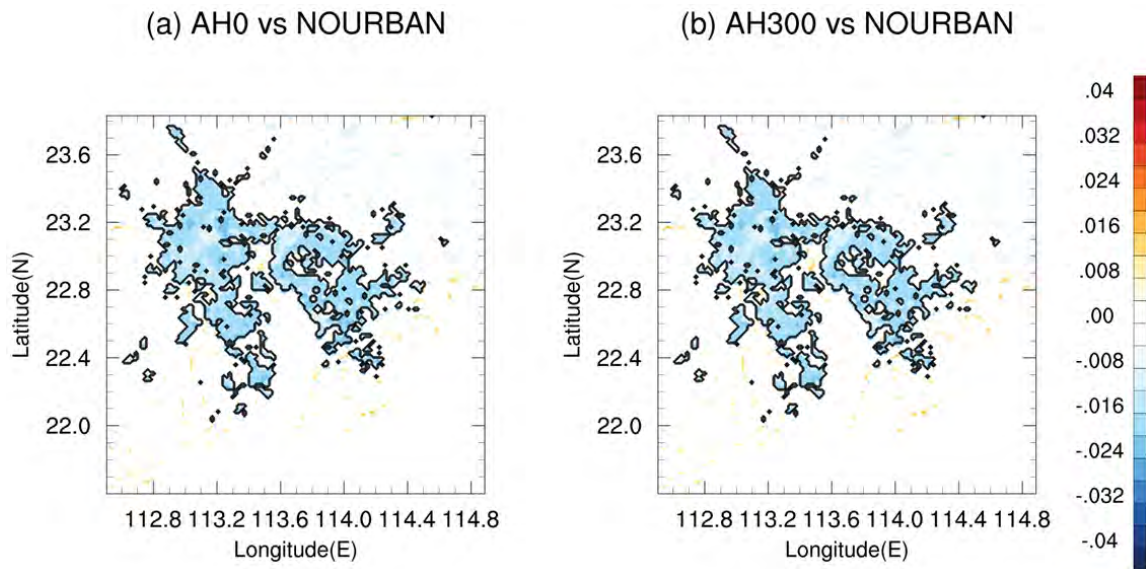
Figure 3.13 *Same as Figure 3.1 except for surface evaporation (units: $g \cdot m^{-2} \cdot s^{-2}$).*

To find the reason why the rainfall is still increases in the PRD megacity despite suppressed local evaporation, the atmospheric environment and the propensity of convection are further investigated. Figure 3.14 shows the vertical profile of the difference of convective available potential energy (CAPE) and convective inhibition (CIN) averaged over the PRD urban area between AH0 and NO-URBAN, and also between AH300 and NO-URBAB, with both CAPE and CIN computed by taking average over entire integration period for all extreme cases. CAPE is the positive buoyancy energy that air parcels will have for vertical uplift, while CIN represents the buoyancy energy needed for air parcels to rise from surface to the level of free convection. In general, lower (higher) CAPE (CIN) means that the environment is

less conductive to convection development. CAPE and CIN are calculated based on following formula with the air parcel undergoing adiabatic process condition and with environmental virtual temperature.

$$cape = \int_{z_{lfc}}^{z_{el}} g\left(\frac{T_v - T_{v,env}}{T_{v,env}}\right) dz$$

$$cin = -\int_{z_{surface}}^{z_{lfc}} g\left(\frac{T_v - T_{v,env}}{T_{v,env}}\right) dz$$

It can be seen that both AH0 and AH300 experiments give lower CAPE than NO-URBAN for air parcel starting in low levels in the urban area (see Figure 3. 14a). Comparing AH0 (AH300) with NO-URBAN, there is a decrease of CAPE about -137.76 (-84.36) J/kg for parcel at the surface. This can probably be attributed to the reduced water vapor content in these levels, because dry air parcel will have a higher lapse rate of virtual temperature. The difference of CAPE between AH0 and NO-URBAN almost vanish at 600m. However, in higher levels the difference is rather small (no more than 5J/kg). For the AH300 experiment, it can be inferred that CAPE is larger than NO-URBAN in the level higher than 600m of height. After further calculation, results show that CAPE increases by about 63.6, 56.92 and 44.85J/kg at 800m, 1000m, and 1200m of height over the urban area. Therefore, the atmosphere becomes more unstable for air parcels lifting in these levels, implying stronger convection and stronger vertical motion.

Moreover, there is a decrease of CIN in all level for either AH0 or AH300 compared with NO-URBAN over the PRD urban area (see Figure 3.14 b). For AH0

and NO-URBAN, the largest difference is found at the surface, with CIN reduces by 5.9J/kg. For AH300, much stronger reduction of CIN is found from surface to 2000m of height, with a difference of about 9.4J/kg at the surface. Therefore, it can be said that convection can be triggered more easily due to the presence of megacity with AH flux added to the urban surface.
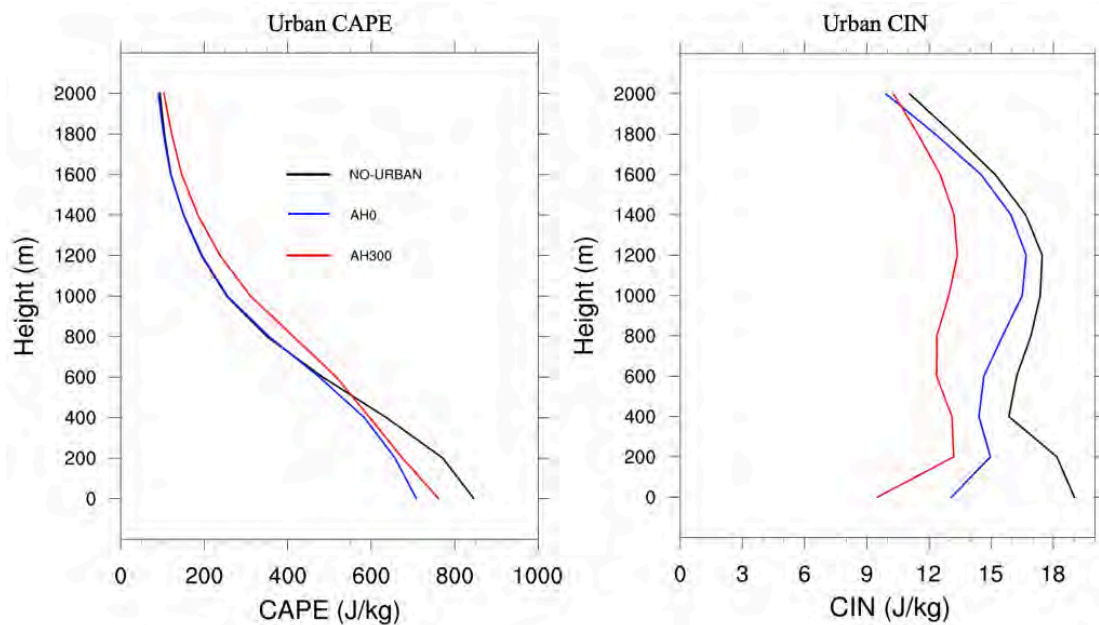
Figure 3.14 *(a)Vertical CAPE profile averaged over urban grids in d03 from NO-URBAN (black), AH0 (blue) and AH300 (red). CAPE is computed by averaging over entire integrations for all selected extreme cases. (b) Same as (a) except for CIN.*

Figure 3.15 shows the CAPE difference for air parcels lifting at 1000m of height. For AH0 vs NO-URBAN (see Figure 3.15 a), the change of CAPE is quite small (no more than 10J/kg) in most locations. However, for the AH300 experiment, there is a strong increase of CAPE over the whole urban area compared to NO-URBAN (see Figure 3.15 b), with the difference greater than 70J/kg over the norther part of the megacity. It can be seen that the distribution of CAPE difference

between AH300 and NO-URBAN for air parcel lifting at 1000m is consistent with the distribution of daily mean rainfall well (see Figure 3.8b).
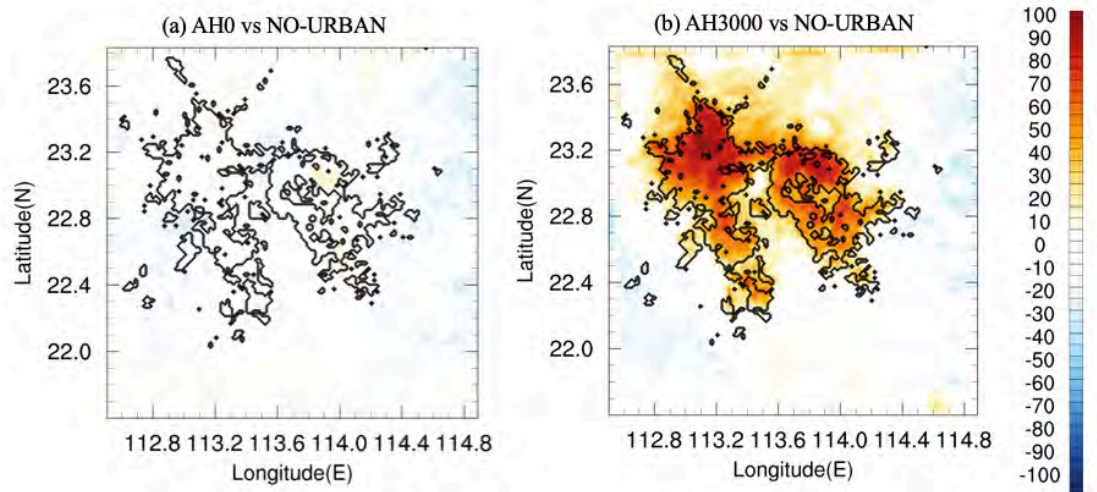
Figure 3.15 *Same as Figure 3.1 except for CAPE of parcel at 1000m of height (units: J/kg).*

Figure 3.16 gives the CIN difference for parcel lifting at 1000m. Similar to CAPE, the change of CIN is weak (no more than 1.5J/kg) when comparing AH0 with NO-URBAN (see Figure 3.16 a). For AH300 minus NO-URBAN, CIN gives a strong decrease of more than 5J/kg over the northeastern part of the urban area (see Figure 3.16 b), while for other urban locations the decrease of CIN is about 3-5J/kg.
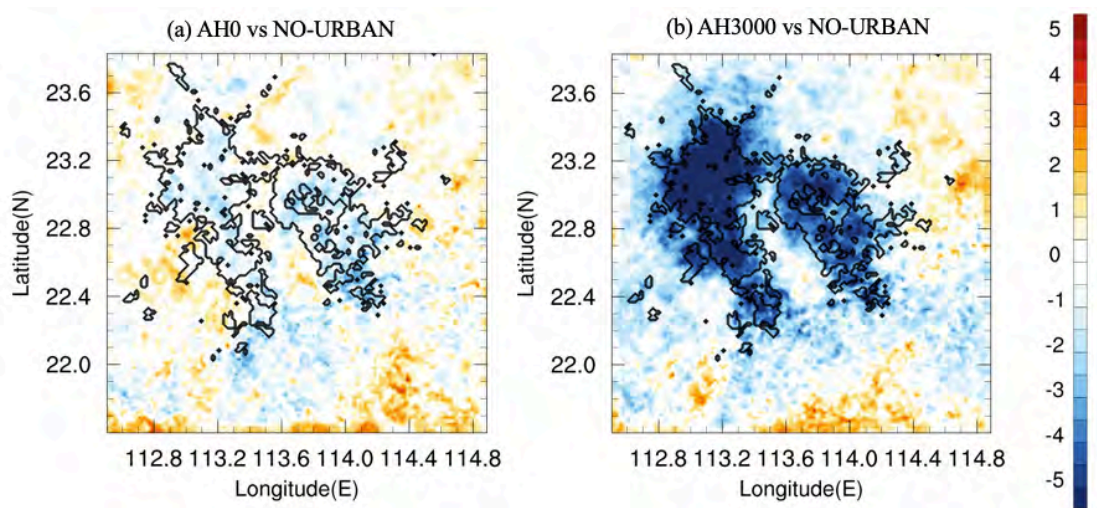
Figure 3.16 *Same as Figure 3.1 except for CIN of parcel at 1000m of height (units: J/kg).*

Overall, the significant increase of rainfall can be attributed to higher CAPE and lower CIN over the urban area in AH300 compared with NO-URBAN. Both show that higher CAPE and lower CIN over the urban area lead to more convection which increases the vertical motion.

The vertical profile of specific humidity from various experiments, and also their differences are inspected. Figure 3.17 shows the southwest to northeast cross-section of vertical wind vector and specific humidity difference over the PRD region between AH0 and NO-URBAN, and also between AH300 and NO-URBAN. It can be seen that both AH0 and AH300 still gives more water vapor than NO-URBAN at higher altitudes, especially for the AH300 experiment. Specific humidity increases more than 0.3g/kg from 0.2km to 2km in AH300, 0.1g/kg at 4.2km and less than 0.1g/kg at 15km. Integrating over all levels in the urban area, there is more water vapor in the AH300 runs compared with NO-URBAN. Noted that stronger vertical motion in the urban area is found in AH300. The increase of specific humidity in higher altitude for AH0, on the other hand, is not as significant as AH300, with no more than 0.1g/kg from 0.2km to 2.5km. Also, the difference in the vertical velocity vector is noisier than that in AH300 (see Figure 3.17a).

To understand the increase of rainfall and its relationship with moisture transport, Figure 3.17 shows the vertically integrated difference of water vapor flux and its divergence between AH0 and NO-URBAN, and also between AH300 and

NO-URBAN. Both maps of the moisture flux difference between AH0 and NO-URBAN, and between AH300 and NO-URBAN, give a similar southwest to northeast direction pattern of vector difference, indicating moisture transport from ocean to the urban area. It can also be seen that for AH300, almost the whole urban area has stronger convergence, especially in the northwestern and eastern urban area, where the difference of moisture flux divergence can reach more than -0.04g/m^{-2}s^{-1}.

Based on the moisture budget equation (see the formula below), while P and E represent the precipitation rate (mm) and surface evaporation rate, t, g, ρ_w, q, V, P$_{sfc}$ and P$_{top}$ mean the time, gravity constant, density of water, specific humidity, horizontal wind velocity, surface air pressure and air pressure at the top of atmosphere, respectively. The first term of right hand means the local moisture change. The second term represents the divergence of moisture flux integrated over all atmospheric layers, while the moisture flux divergence represents the net loss of moisture in atmosphere during unit time. It means that the intensity of rainfall is related to surface evaporation, local moisture term and moisture flux divergence integration.

$$P - E = -\frac{1}{g\rho_w}\frac{\partial}{\partial t}\int_{P_{top}}^{P_{sfc}} q\,dp - \frac{1}{g\rho_w}\nabla * \left[\left(\int_{P_{top}}^{P_{sfc}} \bar{q}\bar{V}\,dp\right) + \left(\int_{P_{top}}^{P_{sfc}} \overline{q'V'}\,dp\right)\right]$$

Though the surface evaporation decreased due to the presence of megacity, the increased moisture flux convergence still leads to the increase of precipitation rate over the urban area.
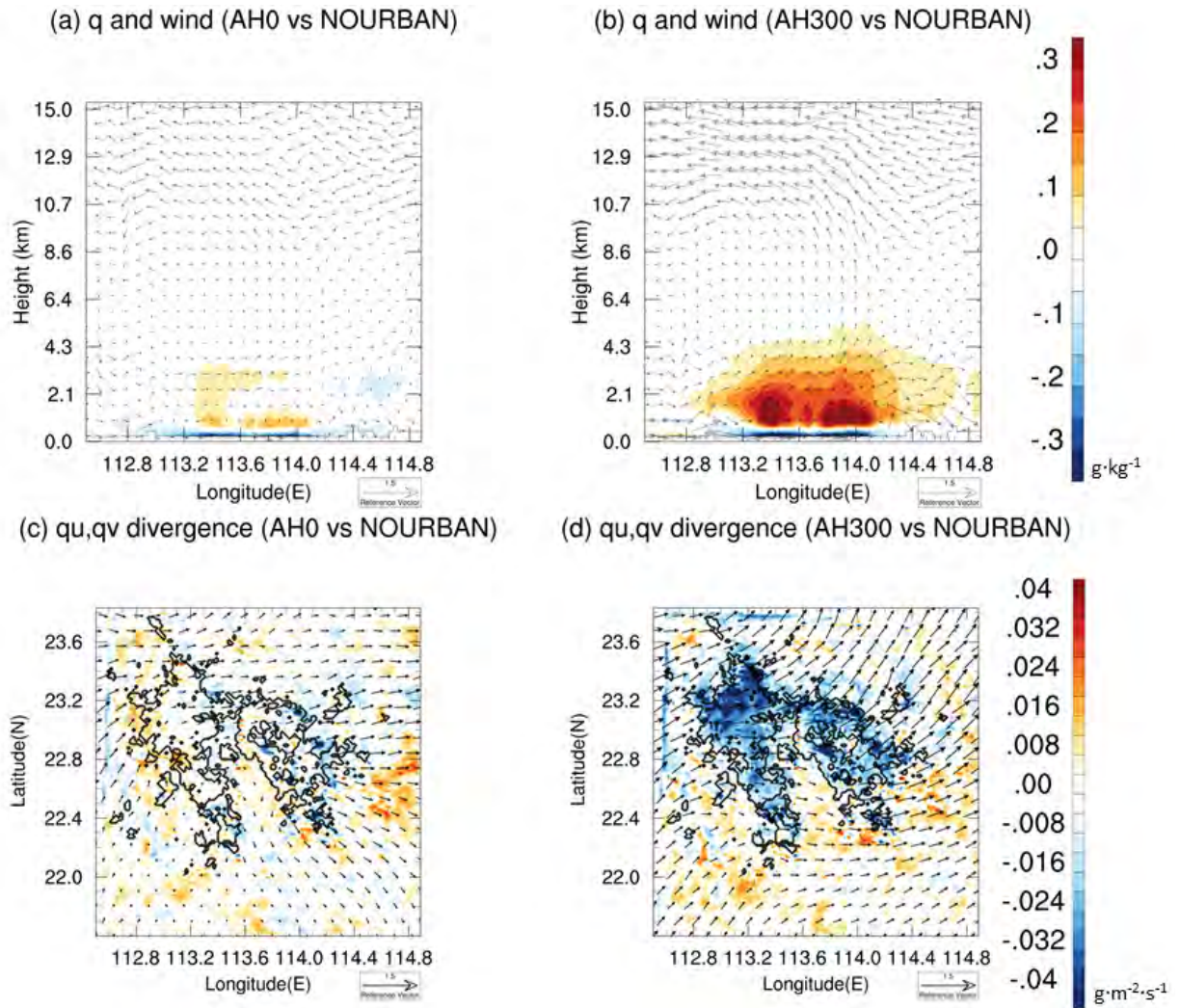
Figure 3.17 *Cross section of hourly mean vertical wind vector and specific humidity between (a) AH0 and NO-URBAN; (b) AH300 and NO-URBAN. Difference of moisture flux and divergence between (a) AH0 and NONURBAN; (b) AH300 and NONURBAN, and their divergences are calculated by summing over entire integrations for all layers in selected extreme cases. See text for details. The urban area within PRD is outlined by black contours*

Figure 3.18 shows the difference of 500hPa vertical velocity between AH0 and NO-URBAN, and also between AH300 and NO-URBAN. It is obvious that the AH0 had slight stronger vertical motion over the urban area compared to NO-URBAN experiment, especially in the eastern part of the megacity (with magnitude less than 0.1m/s). For AH300, the vertical velocity increases over the

whole urban area at a range of 0.1 to 0.4 m/s. That fits the results of increased (decreased) CAPE (CIN) well. The stronger vertical motion can result in more low-level convergence over the urban area, thereby enhancing moisture flux convergence in the region. And corresponding with this picture, there is more accumulated rainfall, and also more moisture content in AH300 runs compared with those in NO-URBAN.
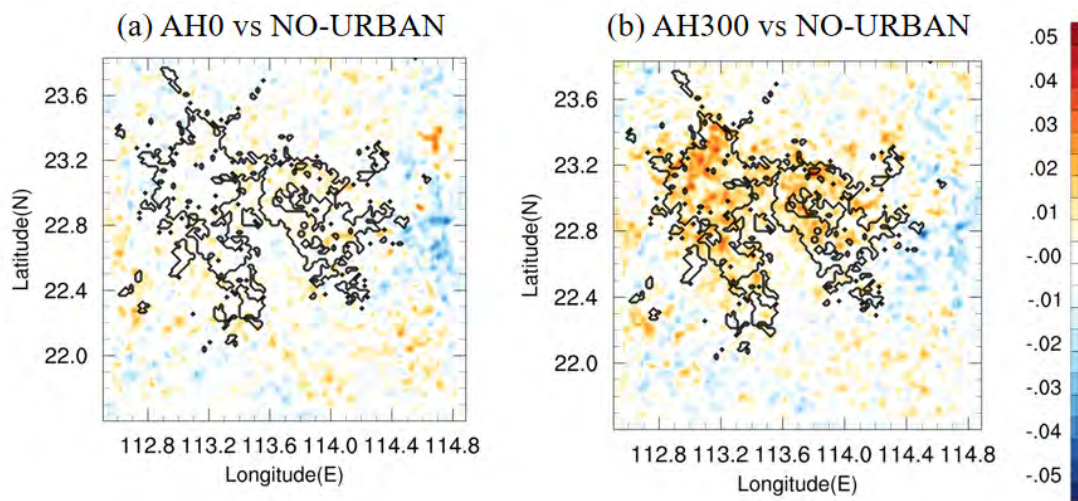
Figure 3.18 *Same as Figure 3.1 except for 500hPa vertical wind speed (units: m/s).*

Finally, the relationship between the prevailing background wind direction and moisture transport is also considered. Figure 3.19 shows the low-level prevailing background wind direction, together with the vertically integrated moisture flux convergence difference between AH300 and NO-URBAN, for each case over the urban area. Here the 950hPa prevailing background wind directions over the urban area are classified into Northeast (black), East (blue), Southeast (red), and Southwest (yellow). There are only three cases with a background northeasterly wind, six cases with an easterly wind, 15 cases with a southeasterly wind and two with a southerly

wind. It is clear that with winds with a southerly component (i.e. from the ocean) tends to be associated with stronger moisture flux convergence than northerly wind. In fact, cases with the letter background wind do not show an obvious increase of convergence of moisture flux. The above suggests that the background prevailing wind can play a role in the moisture convergence over the PRD megacity area.
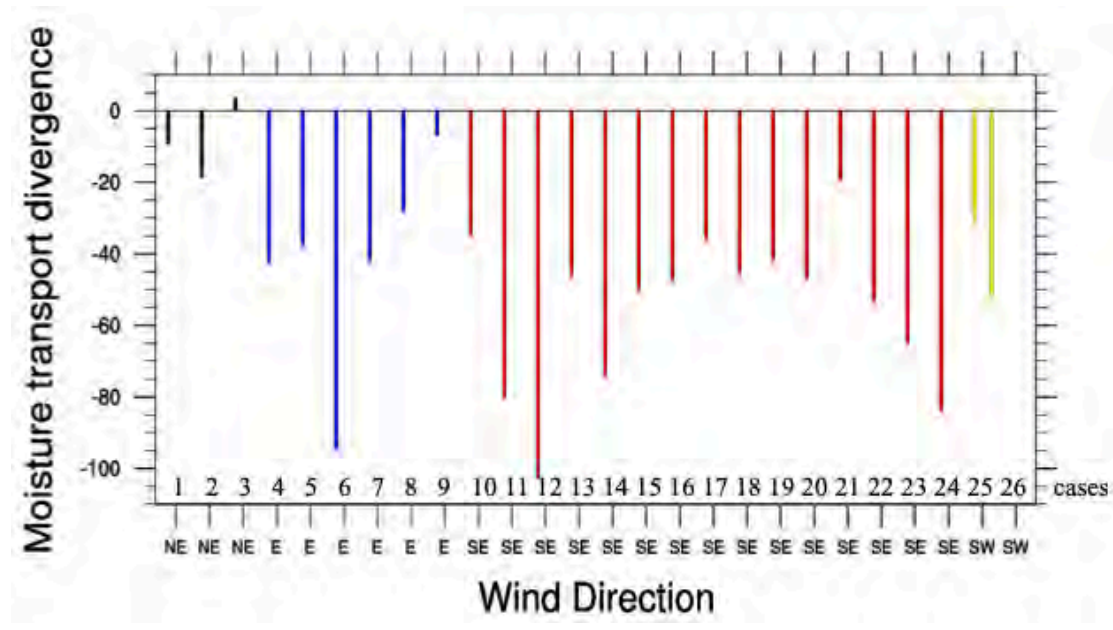
Figure 3.19 Moisture flux divergence for each case of AH300, the value was calculated by summing over entire integrations for all urban grids in selected extreme cases. Abscissa represents the low level prevailing wind direction in urban area. See text for details.

3.4 Discussion and Summary

By utilizing WRF UCM and GFDL-ESM2M simulation, sensitivity of extreme precipitation to the level of urbanization described by land use and AH over PRD megacity region was assessed. Parallel experiments were designed by varying the value of surface AH flux (zero or 300Wm^{-2} as daily maximum) and land use types (urban or cropland). As a result, the PRD mega city cluster had strong UHI effect

which leads to a higher temperature, higher CAPE and lower CIN, and stronger vertical convection.

Furthermore, both the intensity and frequency of extreme rainfall in the urban area of AH300 are increased significantly more than downstream of urban area. The hourly mean rainfall increased by more than 15mm/day, and the probability for strong precipitation is enhanced by 20% at 10-20mm/h^{-1} to almost 200% at 90-100mm/h^{-1}, comparing AH300 with NO-URBAN. This result fits well with observation studies indicating that both the intensity and frequency of extreme rainfall have increased in the PRD mega city cluster area in recent years (Wang et al. 2016). The ocean also plays a role in the increased precipitation. Though surface water vapor content decreased over the urban area, there were more water vapor supply from the South China Sea in AH300 compared to NO-URBAN. Strong convergence induced by higher sensible heat flux can lead to enough water vapor supply from the ocean. However, the change of moisture flux divergence in AH0 was still weak and insignificant compared to NO-URBAN. Overall, the comparison between AH300 and NO-URBAN experiment consistent with the results of Fung (2019), who also utilized the WRF-UCM for dynamical downscaling and found that high AH can lead to stronger extreme rainfall.

Chapter4

4 Impacts of urban development and climate change on near-future extreme rainfall projections over the PRD megacity

It is well-known that urbanization has significant impacts on the local climate over city areas such as high temperature and extreme rainfall (see Chapter 3). At the same time, global warming will result in changes of large-scale circulation, as well as the frequency and intensity of extreme temperature and precipitation events in many locations over the world. In this part, a suite of numerical experiments on extreme rainfall over the PRD area under various background climate and land use/land cover (LULC) conditions will be conducted. The WRF model coupled with SLUCM is utilized to simulate the mesoscale atmospheric conditions in PRD.

4.1 GFDL-ESM2M climatology for historical and RCP8.5 simulations

Projected changes of summertime climate characteristics from GFDL-ESM2M simulation in global scale are first examined. Figure 4.1 represents the 11-years running average of near-surface temperature from 1951 to 2050 over the land region of South China. Here the present period is defined as the period of 1951 to 2000, and the period of 2001 to 2050 is referred to as the near-future period. It can be found that during these years, the near-surface temperature is projected to increase by about 2°C from 299K in 1951 to 301K in 2050, and with a faster trend in near-future era than the present era. In particular, there is only about 0.5°C of increase from 1951 to 2000, but about 1.5°C in 50 years in the near future.
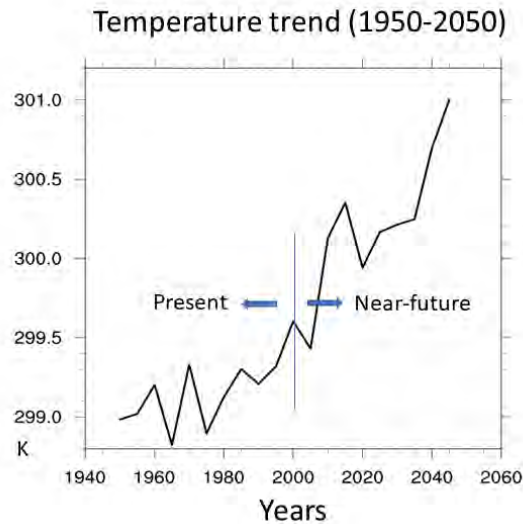
Figure 4.1 *Surface temperature (units: K) from present (1951-2000) to near-future (2001-2050) in summer over the South China land area, based on GFDL-ESM2M historical and RCP8.5 simulations.*

Figure 4.2 shows the near-future minus present surface temperature over East Asia in MJJAS. Strong temperature rises over central China, North India, Central South Peninsula, and Mongolia, with magnitude more than 1.5°C are seen in these regions. In comparison, the change of temperature over South China is relatively mild, with warming of about 0.6 to 0.8°C only.
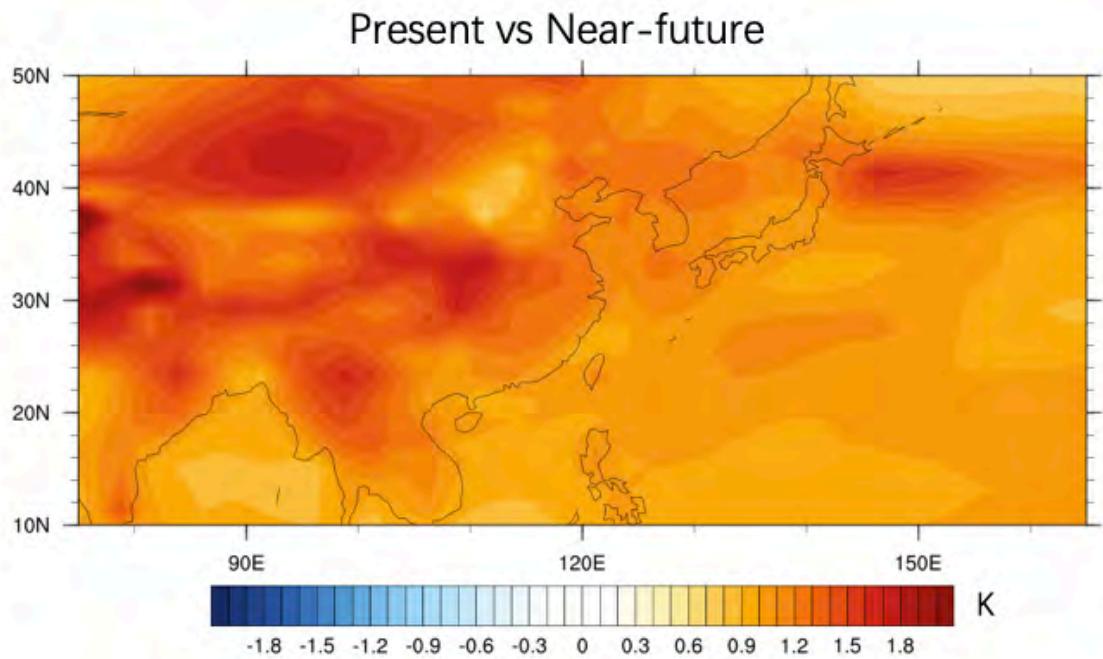
Figure 4.2 *Horizontal distribution of summer near-surface temperature (units: K) comparison between present (1951-2000) and near-future (2001-2050) over East Asia (10-50N, 75-165E). Black contours mean the coastline.*

Figure 4.3 gives the SDII during the present and future era for the MJJAS season, the SDII is computed by the accumulated wet days' rainfall (more than 0.1 mm/day), divided by the number of wet days. It is seen that the pattern of SDII in East Asia does not have a significant change in the near future, with intense precipitation present over the foothills of Himalayas, Central China, Japan, and South East Asia, but the intensity will change due to the global warming.

Based on the SDII, difference between near-future and present climate is also shown in Figure 4.4. The precipitation intensity is projected to increases in several areas, such as Northern China, Southern Himalayas, and Central South Peninsula, where the precipitation anomalies are around 0.6 to more than 1mm/day. On the other hand, there is only slight enhancement of SDII over South China with magnitude of

about 0.3 to 0.5mm/day near Hainan Island. The increase of SDII is no more than

0.3mm/day in most area of Southern China.
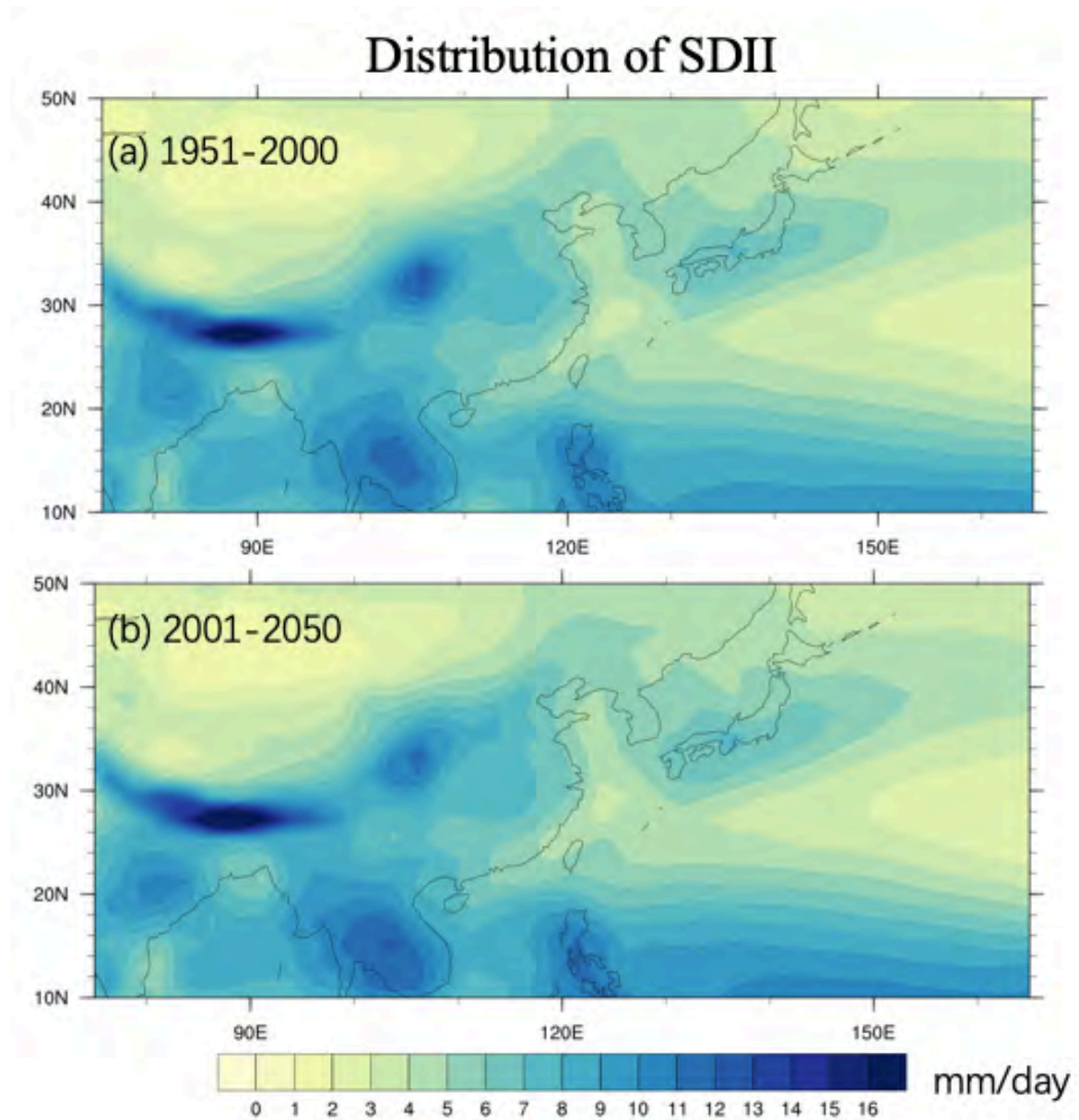
Figure 4.3 *Horizontal distribution of summer SDII (units: mm/day) from (a) present (1951-2000) and (b) near-future (2001-2050) over East Asia (10-50N, 75-165E). Black contours mean the coastline.*
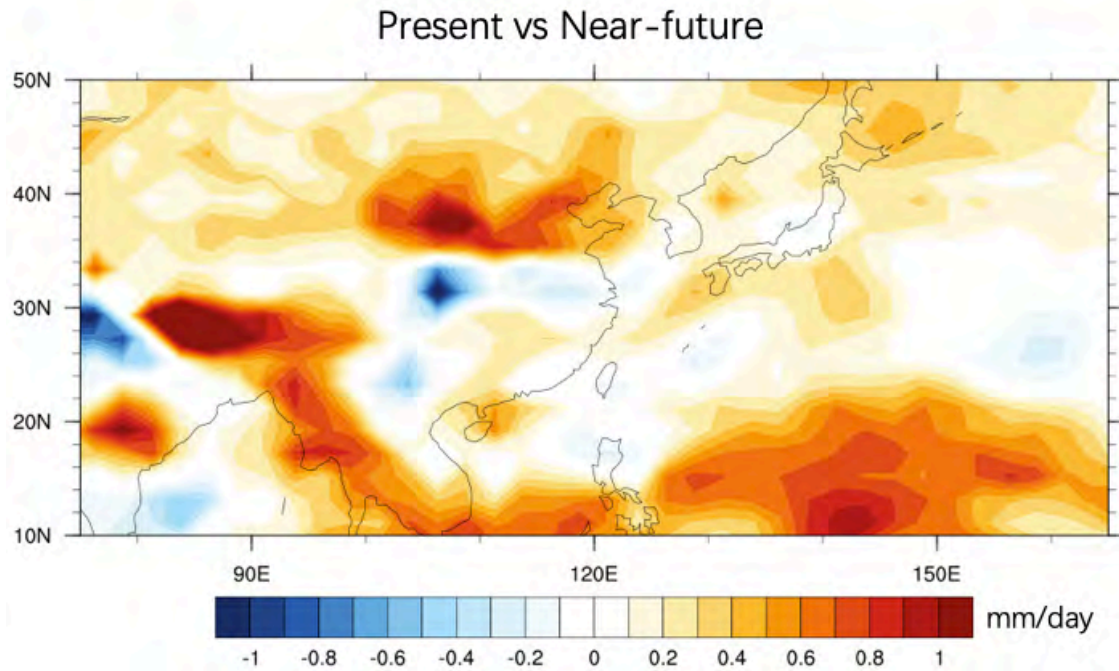
Figure 4.4 *Same as Figure 4.2 except for SDII (units: mm/day).*

Figure 4.5 gives the difference between near-future and present values of 99th percentile daily rainfall over Asia from the GFDL-ESM2M simulations. It can be seen that global warming can greatly influence extreme rainfall over China, India, and South-eastern Asia, with increment of more than 5mm/day in these regions. The extreme rainfall magnitude increases more than 4mm/day in parts of South China, and around 2.5 to 3mm/day over the PRD area. Overall, in southern China the surface temperature and the 99th percentile of daily rainfall increase from 229.12 to 300.17K, and 22.6 to 25.1mm/day, respectively, in the near future. It is also noteworthy that the number of wet days (larger than 0.1mm/day) is projected to decline slightly from 137.34 days/year to 132.7 days/year under global warming. In other words, rainfall in PRD can become more intense, while the rain period can decrease in a warmer climate.
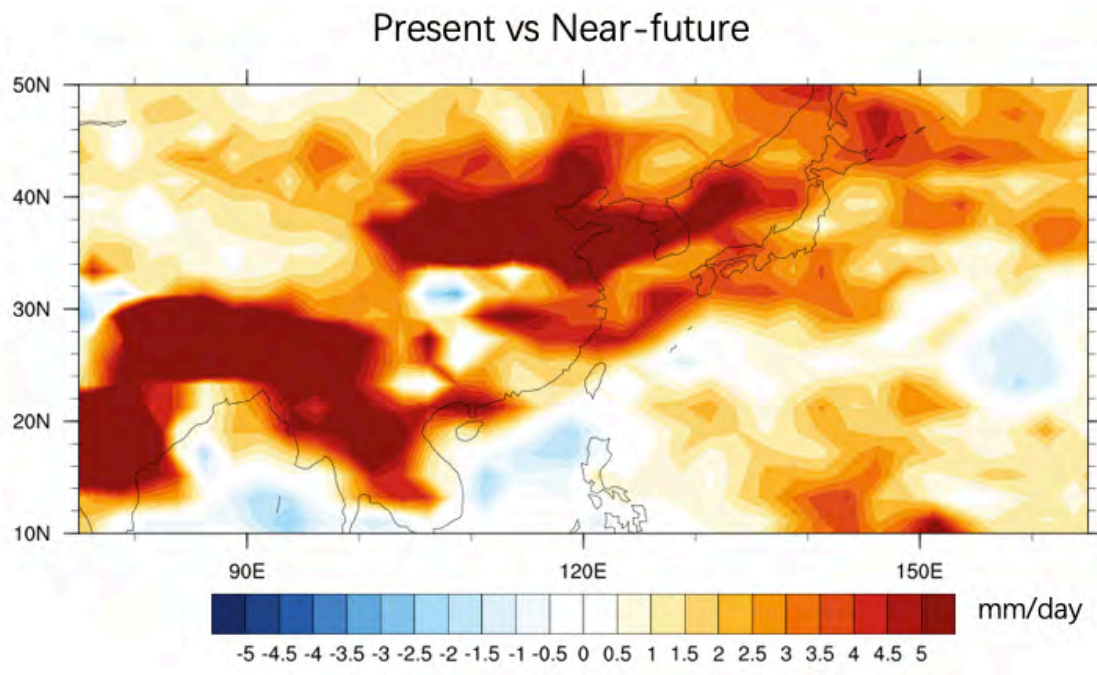
Figure 4.5 *Same as Figure 4.2 except for extreme rainfall based on 99th wet days rainfall (units: mm/day).*

4.2 Dynamical downscaling for extreme rain cases

In this part, three parallel experiments are designed (see Chapter 2.6), the difference between 1999-HIS and 1999-FUT, 1999-FUT and 2030-FUT gives the warming effect and urban development respectively. Figure 4.6 shows the comparison of aggregated 2m temperature PDF within the range of 17 to 37°C at an interval of 1°C from the 1999-HIS, 1999-FUT, and 2030-FUT respectively. Comparing 1999-FUT and 1999-HIS, global warming enhances the 2m temperature significantly in the urban area, and the frequency of high temperature increases for values larger than 27°C. For instance, the likelihood of temperature in the range of 28-29°C increases from 10% to 13%. The mode of 2m temperature has a shift to high intensity in the near future, meaning that the likelihood of higher temperature increases over the urban area due to global warming. At the same time, urban development also seems to have a similar influence on temperature. Comparing 2030-FUT and 1999-FUT results, the probability of high 2m temperature is further increased due to urban development, which is most significant in the range of 28-30°C (with probability enhance from 13% to 15%).
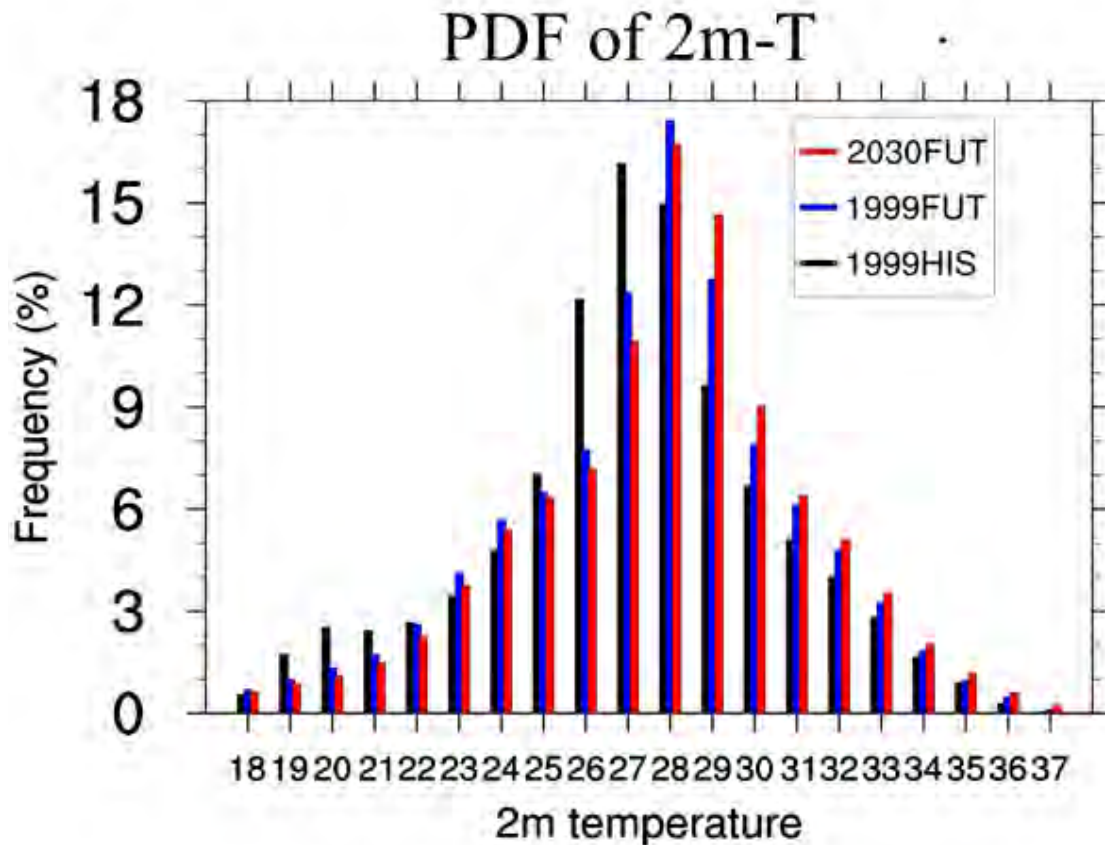
Figure 4.6 *PDFs of hourly 2m temperature within the rages of 17-37°C for the 1999-HIS (black), 1999-FUT (blue), 2030-FUT (red) experiments over corresponding urban locations within PRD.*

Figure 4.7 gives the 2030-FUT minus 1999-HIS, and 1999-FUT minus 1999-HIS 2m temperature difference over the PRD region. Shading indicates the anomaly of 2m temperature, and black lines represent the urban area of 2030's (a) and 1999's (b) in the innermost domain. Global warming can lead to an increase of the mean 2m temperature over these experiments by about 0.2 to 0.6°C over land and 0.3 to 0.6°C over the ocean. When the effect of urban development is considered, the 2m temperature is enhanced by about 0.4 to 0.8°C over the urban area. Therefore, according to these experiments, global warming and urban development can result in a comparable 2m temperature increase over the PRD megacity area in the near future.
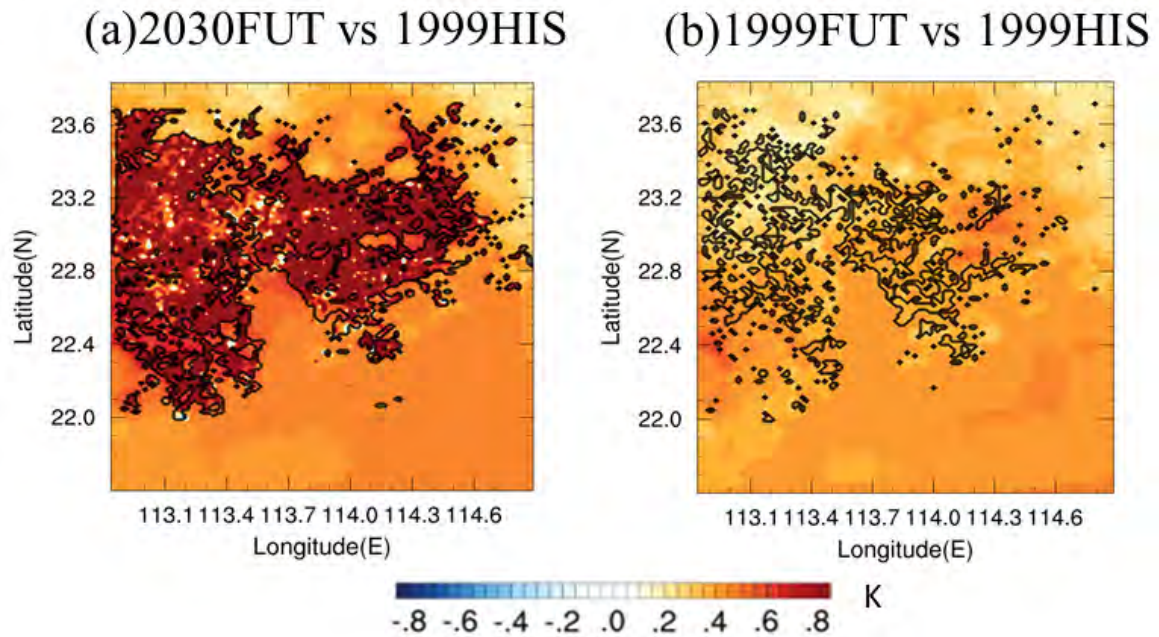
Figure 4.7 2m temperature difference (units: ˚C) between (a) 1999-HIS and 2030-FUT and (b) 1999-HIS and 1999-FUT. Temperatures are computed by averaging over entire integrations for all selected extreme cases. See text for details. The urban area within the PRD in 1999 and 2030 is outlined by black contours.

PDFs of hourly precipitation rates are now considered, in order to investigate the influence of urban development and climate change on extreme rainfall. Figure 4.8 shows the rainfall PDFs from 1999-HIS, 1999-FUT, and 2030-FUT experiments within the range of 1-110mm/hr. Compared with 1999-HIS, frequency of light rainfall (those rainfall events in the range of 1-20mm/hr) from 1999-FUT is decreased in the range of 1-10 mm/hr (from 14% to 9.3%). However, global warming can lead to an increase of heavy rainfall (larger than 20mm/hr) probability significantly in the near future. For rainfall rates of 50mm/hr, the increase is around 20% to 40%. Comparing 1999-FUT and 2030-FUT, it can be inferred that urban development can increase the frequency of urban precipitation for all rain rates (1-110mm/hr), and an even stronger effect on heavy rainfall (larger than 50mm/hr) than light rainfall (1-20mm/hr). For

rain rates in the range of 50-100mm/hr, the frequency increase is about 30% to even 60% due to PRD urban development.
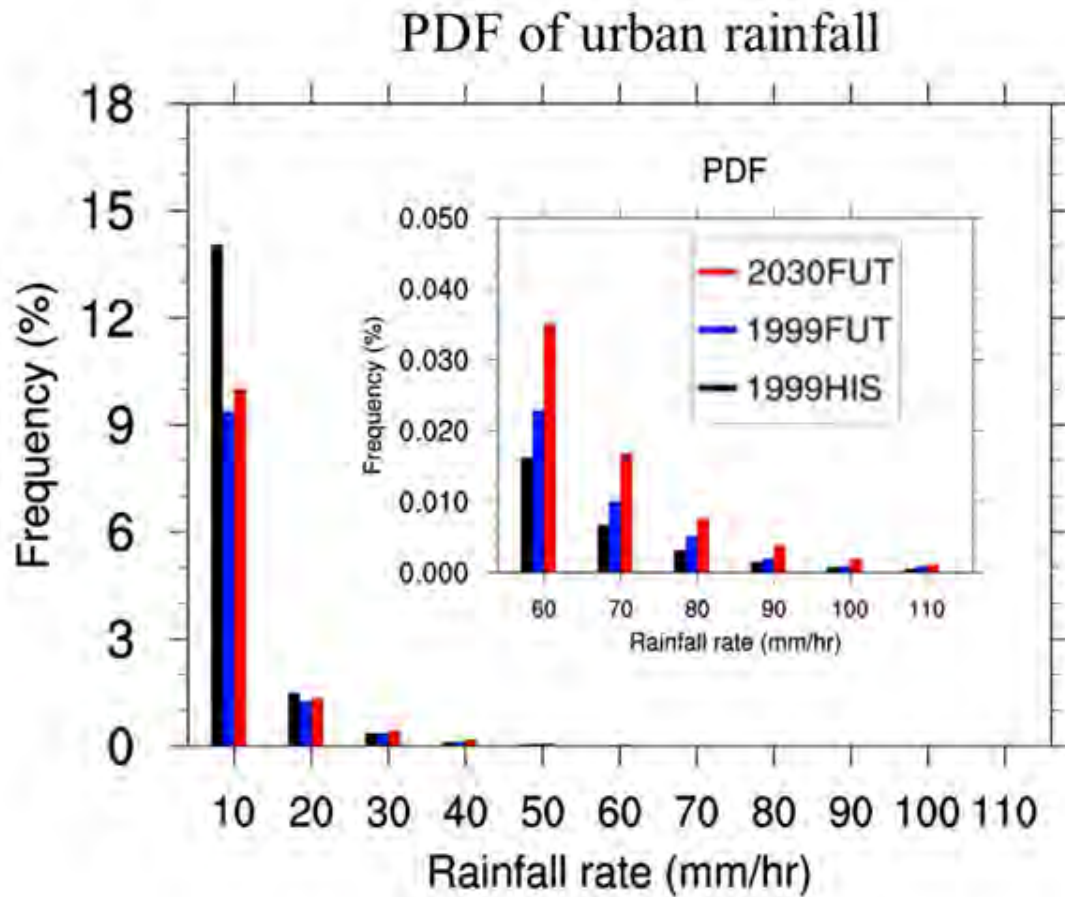
Figure 4.8 *PDFs of hourly precipitation rates within the rages of 1-10, 10-20, 20-30, 30-40, 40-50, 50-60, 60-70, 70-80, 80-90, 90-100, and 100-110 mm/hr (denoted by 10, 20, 30, 40, 50, 60, 70, 80, 90, 100, 110mm/h, respectively) for the 1999-HIS (black), 1999-FUT (blue), 2030-FUT (red) experiments over corresponding urban locations within PRD.*

Figure 4.9 shows the ratio of rainfall probability between 1999-HIS and 1999-FUT, and also between 2030-FUT and 1999-FUT, computed over all urban grid boxes. Here the red and blue lines represent the ratio for type1 (Low-Intensity Residence) urban land use, and for combined type2 (High-Intensity Residence) and

type3 (Commercial and Industrial) land use respectively. From the 1999-FUT to 1999-HIS ratio (see Figure 4.9a), it is clear that global warming tends to suppress light rainfall over whole the urban area in the range of 1-20 mm/hr, while the likelihood of heavy rainfall (larger than 30mm/hr) is enhanced. Such an enhancement is even stronger over the highly urbanized area (type2 and 3), with the ratio reaching 2.1 to 2.4 in 70-100mm/hr; for Low-Intensity Residence (type1), the ratio does not exceed 1.5 for all ranges (1-110mm/hr). Urban development, however, has a stronger influence over Low-Intensity Residence than highly urbanization locations. The 2030-FUT to 1999-FUT ratio of rain rate (1-100mm/hr) probability is about from 1.1 to 2.3, with increasing values as the rain rates increase. Over highly urbanized area, such ratio is only about 1.1 to 1.5.
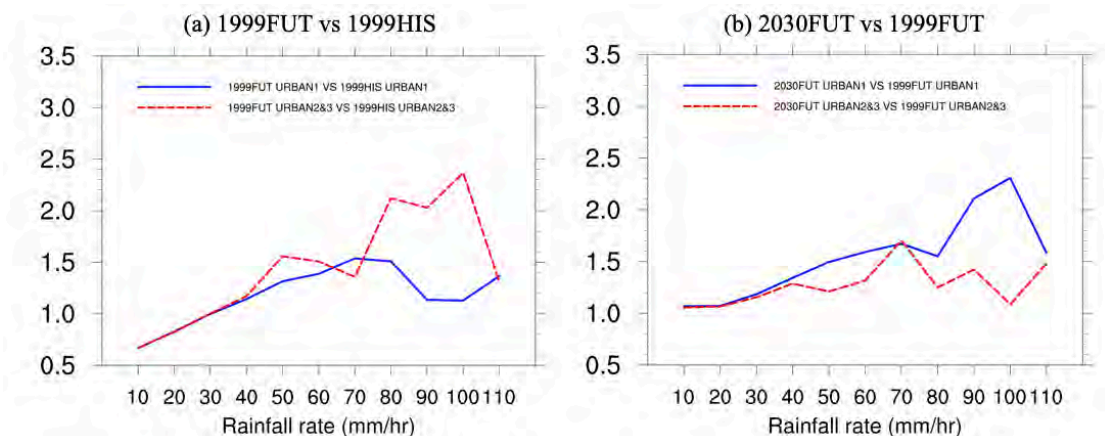
Figure 4.9 *Ratio of the probabilities between (a) 1999-FUT and 1999-HIS, (b) 2030-FUT and 1999-FUT over low intensity residence (blue), high intensity residence and commercial and industrial (red) at different precipitation rates.*

Overall, both urban development and global warming can significantly enhance the frequency of extreme rainfall over the PRD urban area. Figure 4.10 shows the difference of daily mean rainfall between 1999-FUT and 1999-HIS, and

that between 2030-FUT and 1999-FUT, based on all selected extreme cases considered. Global warming can enhance the daily mean rainfall amount over the whole land area in the near future, and the change is about 5-8 mm/day over the urban area. Urban development only leads to more accumulated rainfall in highly urbanized areas such as the central area of the PRD urban cluster, with increment of about 8-10mm/day. Over the more southern part of the domain, the rainfall change seems to be insignificant.
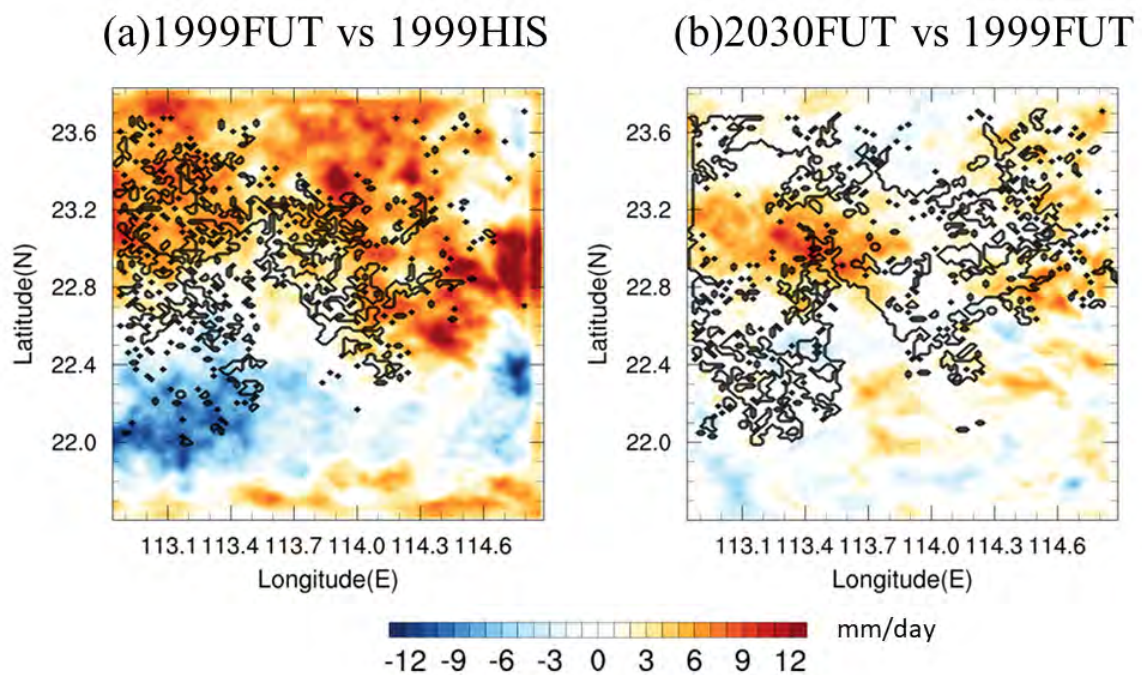
Figure 4.10 *Same as Figure 4.7 except for daily precipitation rates (units: mm/d).*

Student's t-test, and K-S test are also conducted to examine the statistical significance of changes in rainfall characteristics in these experiments. Figure 4.11 shows the results for mean rainfall difference. The precipitation difference caused by global warming can pass 95% significance level in most grids over land, especially in the northwest and north part, and also some negative signals in the ocean can pass the

95% significance level. Increased total rainfall due to urban development in central part of the megacity area is also significant to the 95% significance level. For the K-S test (see Figure 4.12), results indicate that the PDF of 1999-HIS and 1999-FUT are significantly different over almost all grids in northwest part of the domain (at the 95% significance level). However, the 1999-FUT and 2030-FUT PDF comparison gives a noisy pattern (see Figure 4.12b), which can be attributed to the weak change of urban parameters in model environment.
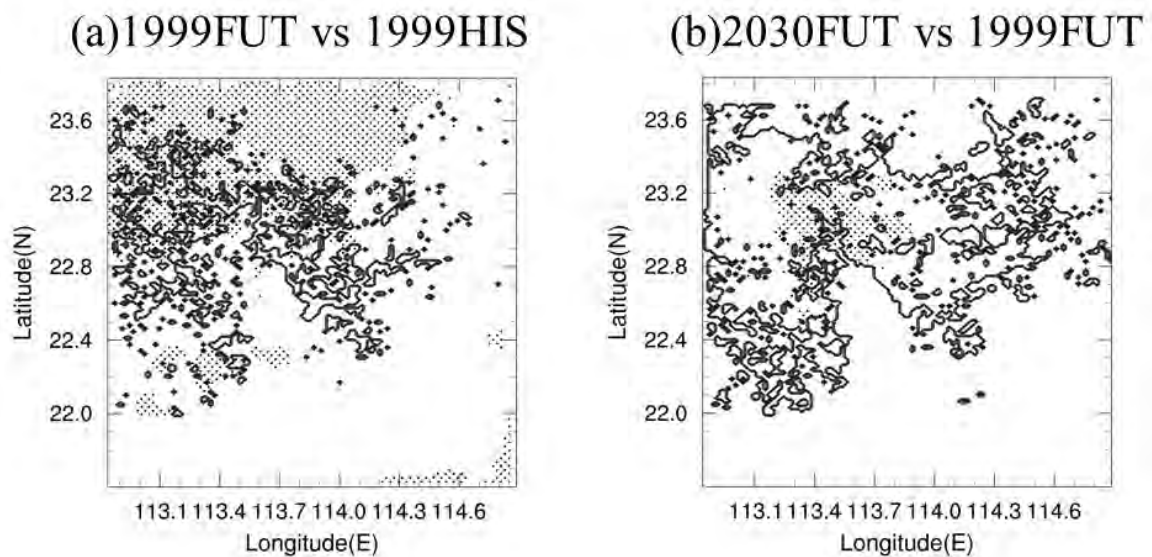
Figure 4.11 *Results of Student's t-test of daily mean rainfall difference between (a) 1999-HIS and 1999-FUT, (b) 1999-FUT and 2030-FUT. Locations in which the difference exceeds the 95% significance levels are denoted by black dots. The urban area within 1999's and 2030's PRD is outlined by black contours.*
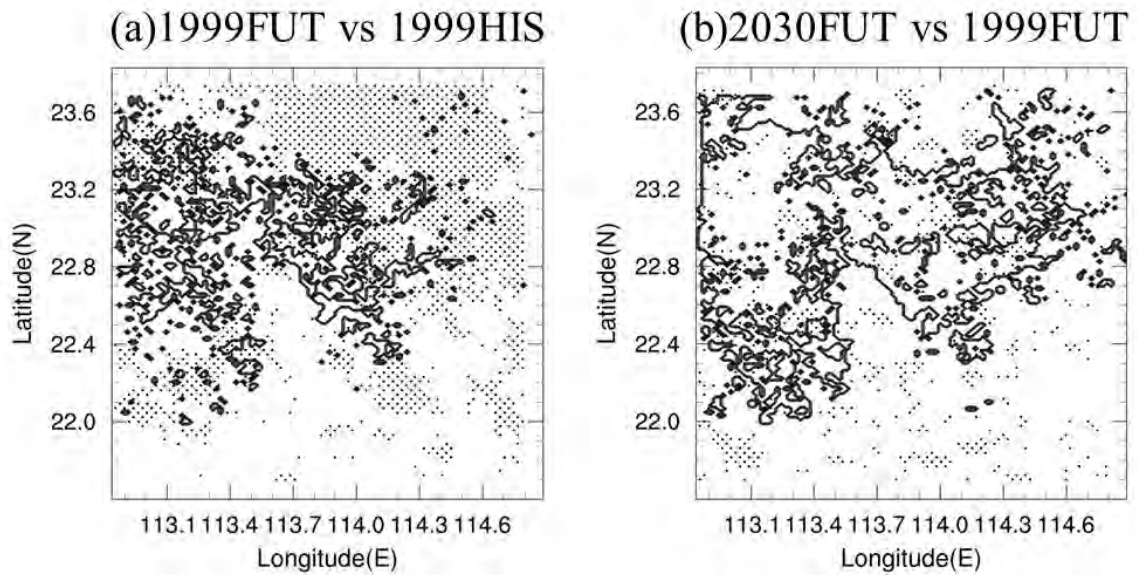
Figure 4.12 *Same as Figure 4.11 except for results of the K-S test on the difference of PDFs of hourly precipitation rates.*

4.3 Convective stability and humidity

To explain why global warming and urban development play a positive impact on both frequency and intensity of extreme rainfall, Figure 4.13 shows the precipitable water difference, between 1999-HIS and 1999-FUT, and also between 2030-FUT and 1999-FUT. Higher surface evaporation (see Figure 4.14a) and surface latent heat flux (see Figure 4.14b) in the near-future runs can enhance precipitable water in the region. In fact, the precipitable water is increased in 1999-FUT compared with 1999-HIS in the whole region. Such an increase can contribute to stronger extreme rainfall in the near future. Also, as demonstrated in Chapter 3, the stronger UHI effect caused by urban development can also lead to moisture flux convergence, which results in more precipitable water in 2030-FUT compared with 1999-FUT. This

is seen over the central part of the megacity areas. Such an increase is consistent with stronger extreme rainfall at the same location.
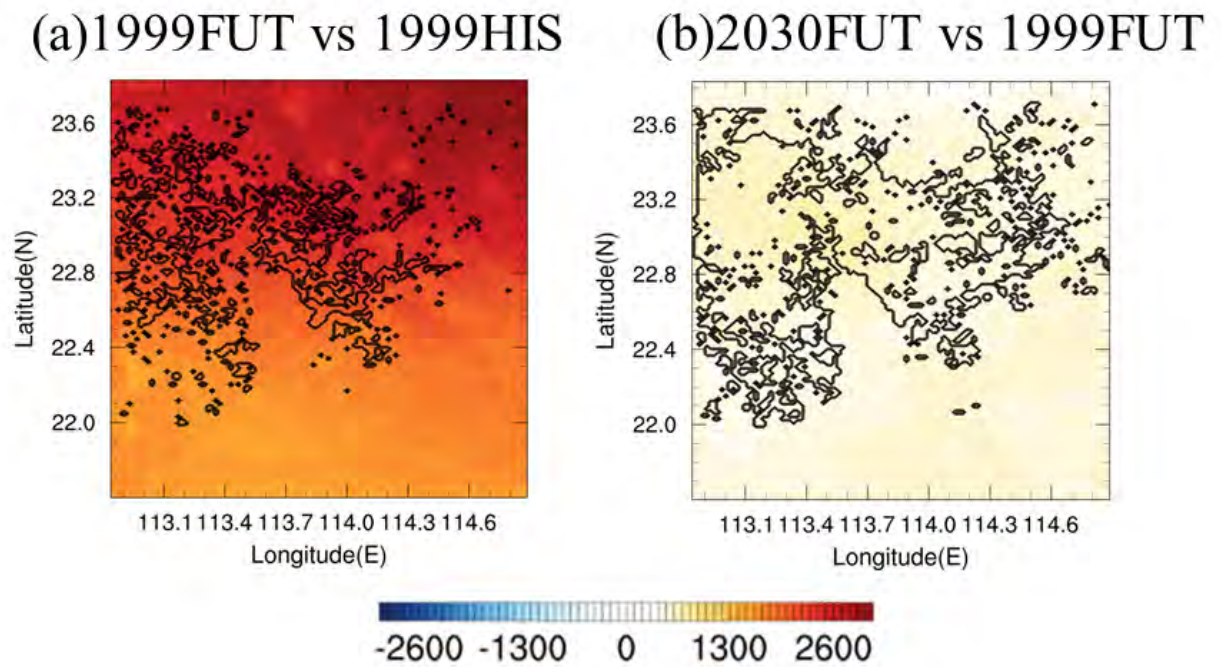
Figure 4.13 Same as Figure 4.7 except for precipitable water (units: g/m²).
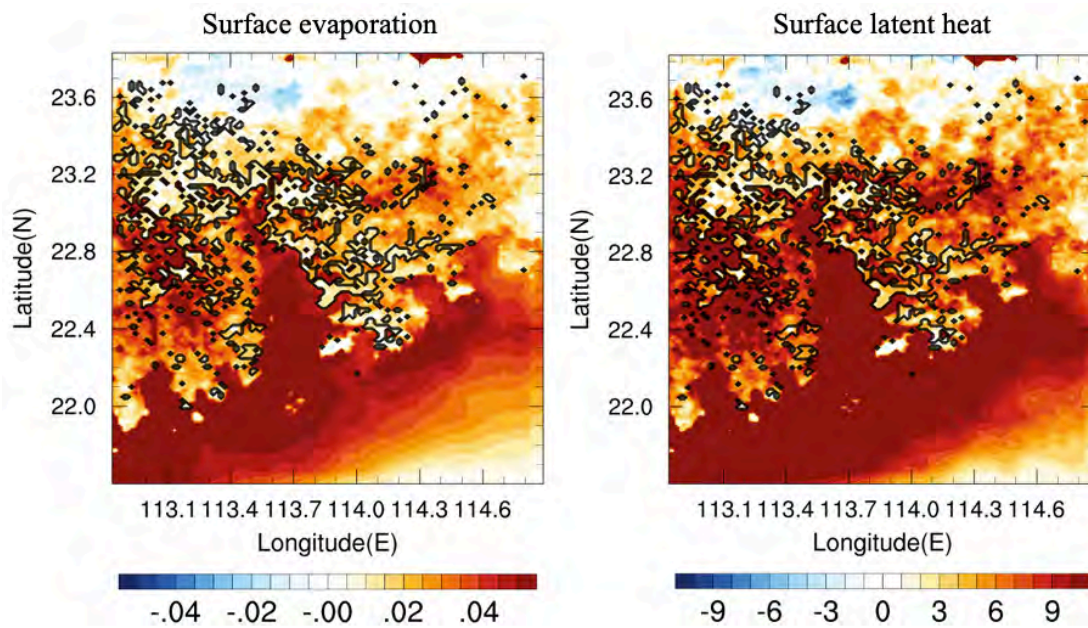
Figure 4.14 *Same as Figure 4.7 except for (a) surface evaporation (units: g/m²/s), (b)*

surface latent heat flux (W/m²).

CAPE and CIN are also calculated for three experiments. Figure 4.15 gives the vertical profiles of CAPE and CIN with parcels rising in various levels, averaged over the urban area from 1999-FUT and 1999-HIS. For the difference of CAPE between 1999-FUT and 1999-HIS, it can be inferred that global warming leads to a decrease of CAPE from the surface to 600m of height. For air parcels higher than 600m, there is a strong increase, reaching 43.04 J/kg at 1000m. For CIN, the change is weak from surface to 400m of height, but there is a strong positive increase from 400 to 1400m due to warmer climate. The difference of CIN is about 2.3, 3.1, and 2.4J/kg at the height of 600, 800, 1000m respectively. At 1400m or higher the CIN difference becomes negative.

In general, global warming can lead to an increase of both CAPE and CIN at 600m or higher. Higher CIN means the atmosphere tends to be more stable, and it is more difficult for convection to be triggered. But increase of CAPE above 600m (CIN also decrease above 1400m) can still lead to more convection above that level during these extreme rainfall cases.
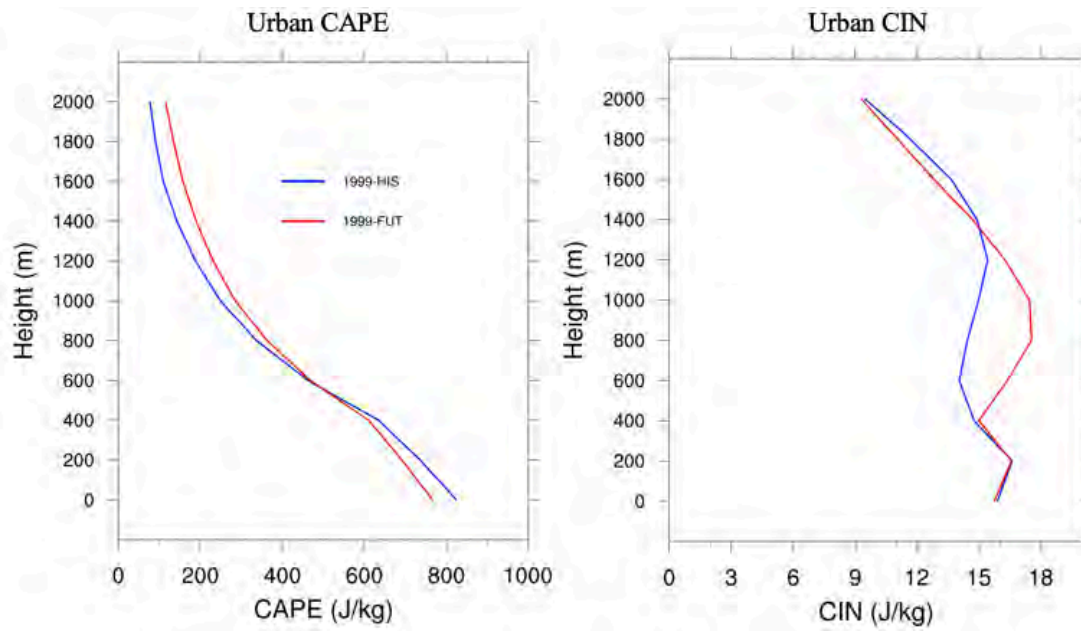
Figure 4.15 (a)Vertical CAPE profile averaged over urban grids in d03 from 1999-HIS (blue) and 1999-FUT (red). CAPE is computed by averaging over entire integrations for all selected extreme cases. (b) Same as (a) except for CIN.

To understand the increase of CIN, Figure 4.16 shows the vertical profiles of temperature and relative humidity averaged over the urban area from 1999-FUT and 1999-HIS. Temperature difference caused by warmer background climate increases with height (see Figure 4.16a), and the average temperature difference over the urban area is only about 0.38°C at surface, then increasing to 0.747K at 2000m. For relative humidity (see Figure 4.16b), the result is similar. The relative humidity remains almost unchanged at the surface, and then increases by 0.57% and 1.04% at 1000m and 2000m respectively. Hence, the 1999-FUT experiment gives higher environment virtual temperature which caused the decrease (increase) of CAPE (CIN) under 400m (1400m) compared to 1999-HIS.
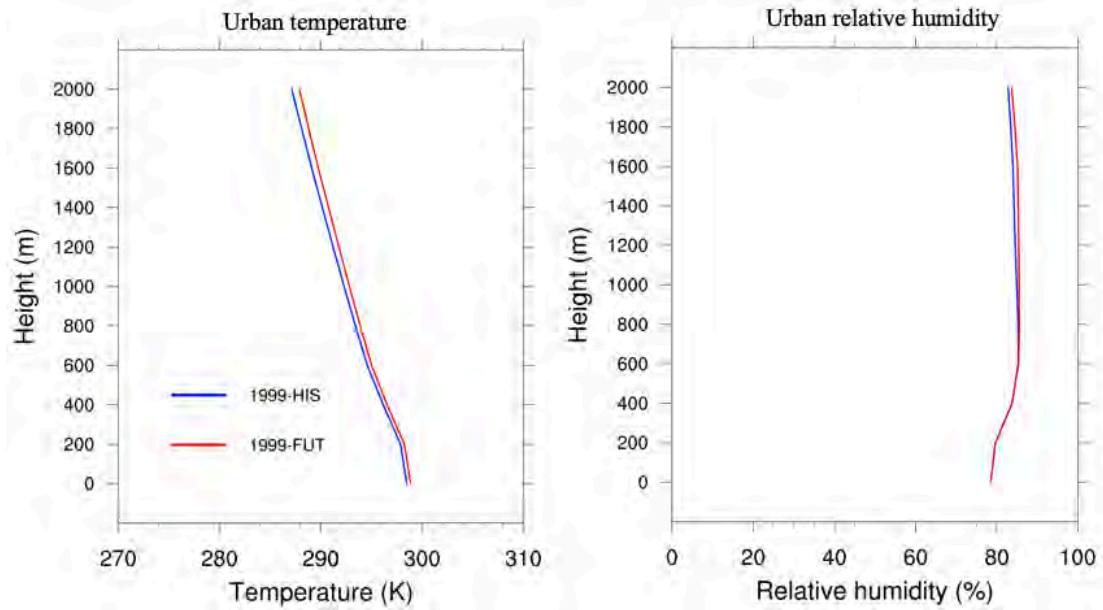
Figure 4.16 *Same as Figure 4.15 except for (a) temperature, (b) relative humidity.*

Figure 4.17 shows the vertical profile of CAPE and CIN averaged over the urban area from 2030-FUT (red) and 1999-HIS (blue). Decrease of surface evaporation caused by urban development leads to a decrease of CAPE for parcel under 600m of height. However, the CAPE difference is still weak above 600m (no more than 3J/kg) over whole megacity. Considering such small change due to land use change, the impact of urban development over whole urban area is weak and regional. From the difference of CIN between 2030-FUT and 1999-FUT, it can be inferred that the urban development results in less CIN from surface to 2000m, with a decrease of 1.46J/kg and 1.06J/kg at surface and 2000m respectively.
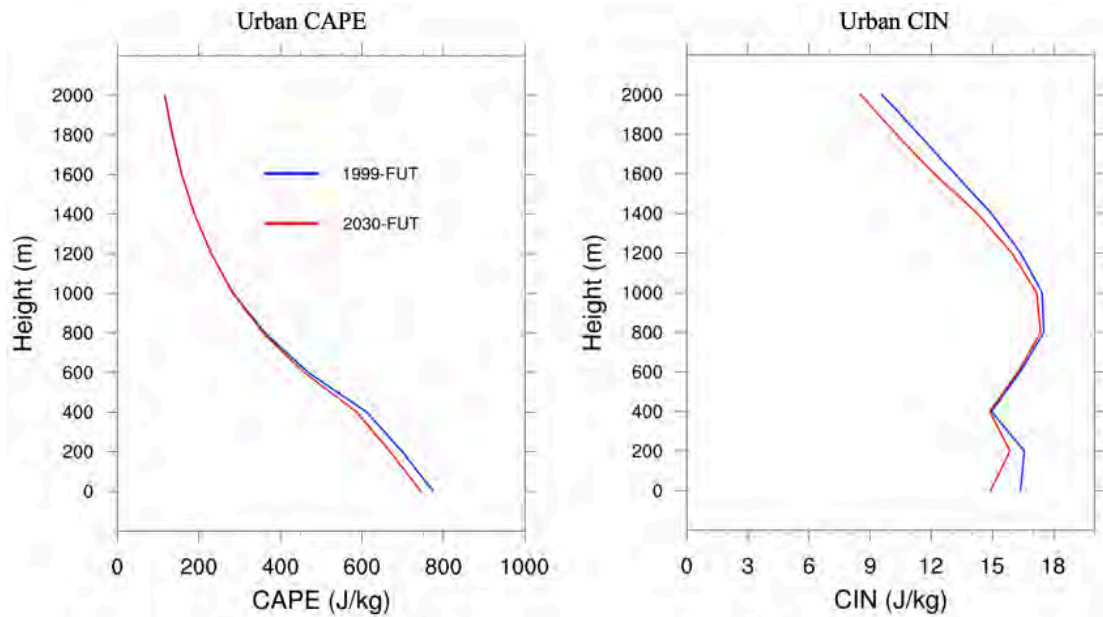
Figure 4.17 *(a)Vertical CAPE profile averaged over urban grids in d03 from 1999-FUT (blue) and 2030-FUT (red). CAPE is computed by averaging over entire integrations for all selected extreme cases. (b) Same as (a) except for CIN.*

Considering that the impact of urban development is not uniform over the whole urban area, daily rainfall increases more over the central urban area. We further computed CAPE difference for parcel rising at 1000m between 2030-FUT and 1999-FUT (see Figure 4.18). For CAPE, there is an increase of CAPE around 15 to 30J/kg at the central urban area, and such increase is consistent with the rainfall increase (about 3-12mm/d) at the same location. At the same time, Figure 4.19 gives the vertical profile of CAPE averaged over a subdomain within the urbanized PRD region (113.1-113.8E, 22.6-23.18N, shown as the red area in Figure 4.19b, in which only the urban girds were considered) from 2030-FUT and 1999-FUT. CAPE has a decrease under 600m, then increasing above this level, and the difference from 1000m to 1600m is about 8-10J/kg.
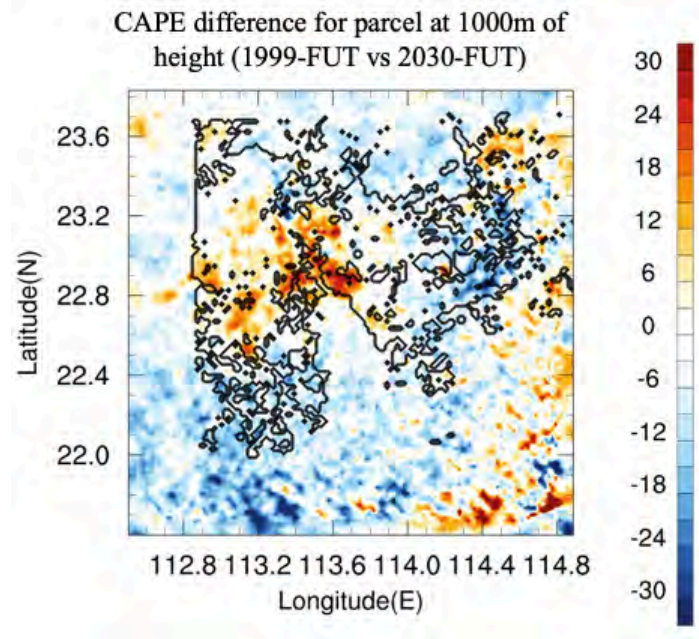
Figure 4.18 *Same as Figure 4.7 except for CAPE of 1000m parcel (units: J/kg)*

between 2030-FUT and 1999-FUT.
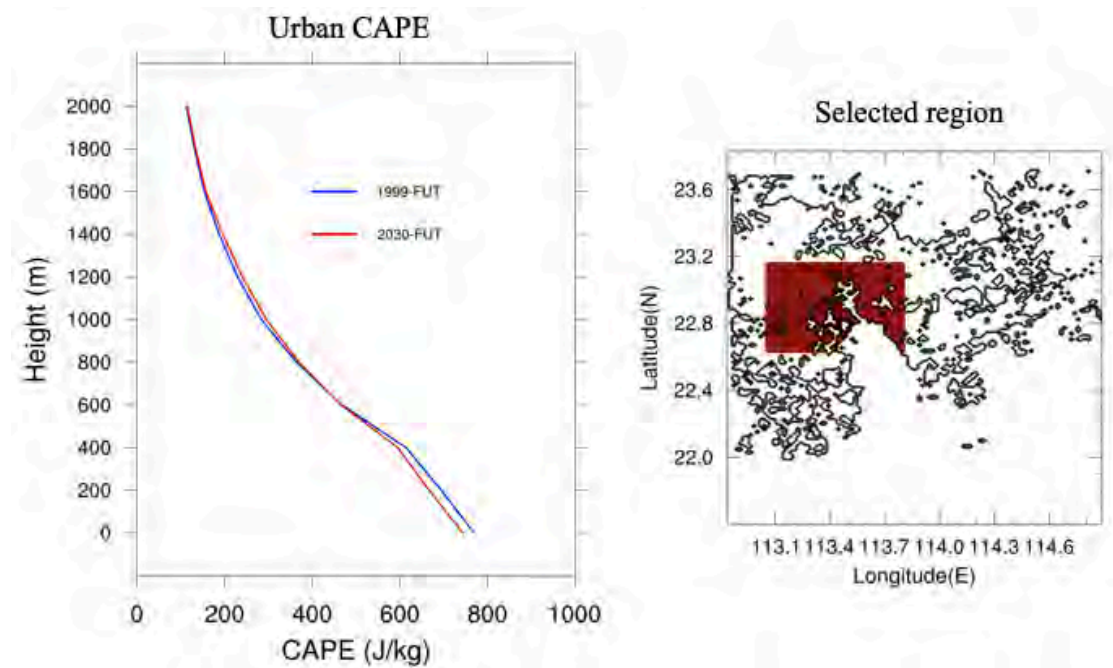
Figure 4.19 *(a)Vertical CAPE profile averaged over land within* 113.1-113.8E,
22.6-23.18N *from 1999-FUT (blue) and 2030-FUT (red). (b) Selected area for*
averaging.

It was shown that the urban development indeed leads to an increase of CAPE above 600m in the central urban area. To find out whether convection also changed due to urban development, Figure 4.20 gives the difference of cross-section of vertical specific humidity and wind vector between 2030-FUT and 1999-FUT. Due to urban development, surface specific humidity is reduced, but more water vapor is found at the height from 300m to 6km. In other words, there is still more water vapor during extreme rainfall events. Moreover, compared with 1999-FUT experiment, 2030-FUT has stronger vertical wind in the urban area, especially in the western new urban area and central highly urbanized area. This phenomenon can also be explained by the regional increasing CAPE. Therefore, the urban development can play a role in local circulation and convection over the central urban area, which leads to a significant increase of extreme rainfall probability in that region.
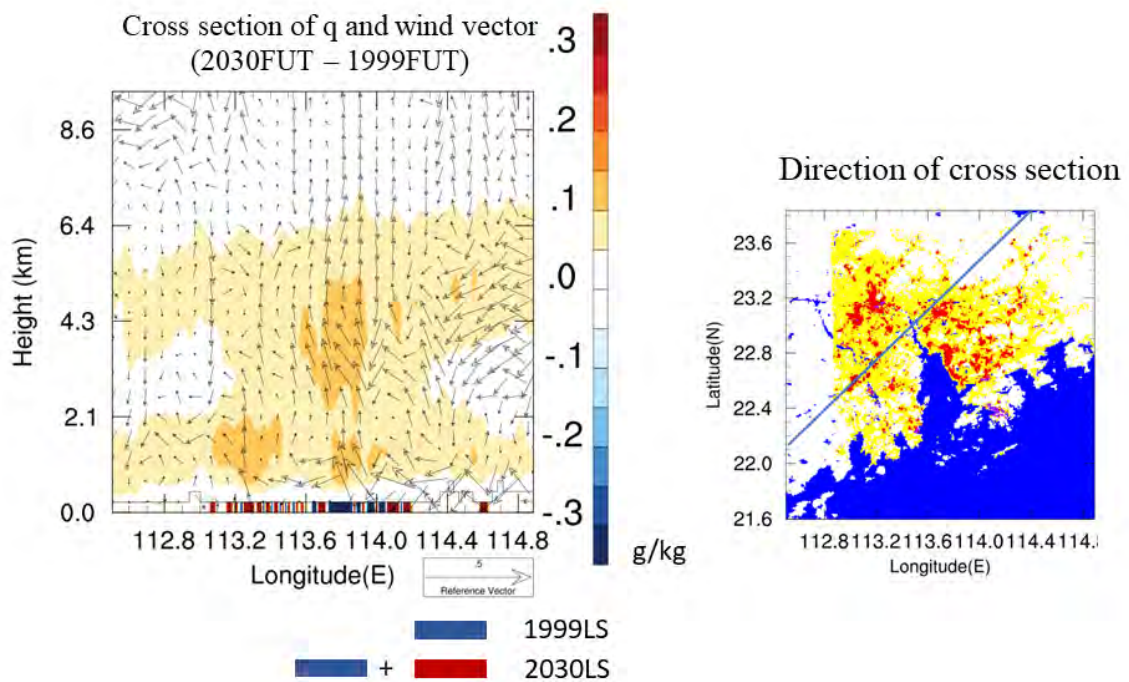
Figure 4.20 *(a) Cross section of hourly mean vertical wind vector and specific*

humidity between 1999-FUT and 2030-FUT, blue bar represents the old urban area in 1999 and red bar means new urban area in 2030. (b) Direction of cross section over the PRD region. See text for details.

4.4 Diurnal change of rainfall

How global warming and urban development can affect the diurnal rainfall is also considered. Figure 4.21 shows the diurnal change of urban precipitation for 1999-HIS, 1999-FUT, and 2030-FUT, computed by averaging all cases over the megacity region. Here the signals are filtered such that only the first and second harmonics are remained. Comparing 1999-FUT and 1999-HIS, it is evident that global warming can lead to a slight decrease in rainfall at late night and in the morning, with reduction about 0.1 to 0.15mm/hr. On the other hand, intensity of rainfall in the afternoon is increased, by about 0.4mm/hr at 4 pm. Urban development can increase rainfall intensity for the whole day (compare 1999-FUT and 2030-FUT), by about 0.1 to 0.2mm/hr during 6 am to 4 pm, but no more than 0.1mm/hr in the evening and at late night. Moreover, there is a delay of the peak diurnal rainfall to later hours in the afternoon during extreme precipitation events.
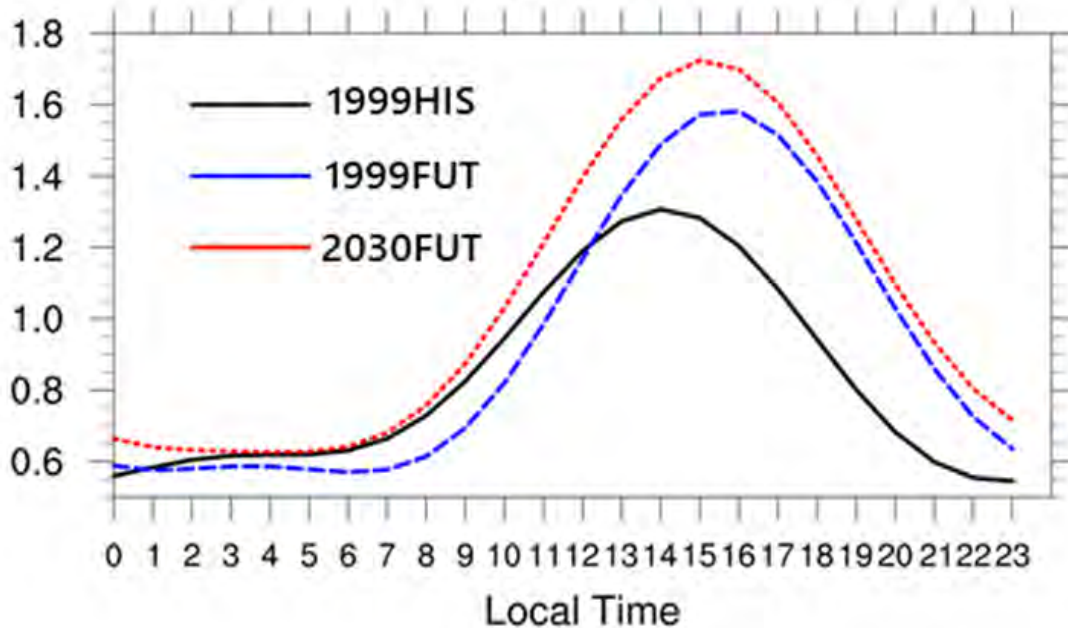
Figure 4.21 *Diurnal change of urban precipitation (unit: mm/hr) from 1999-HIS (black), 1999-FUT (blur) and 2030-FUT (red). Precipitations are computed by averaging over entire integration for all selected extreme cases over the urban area. See text for details.*

Figure 4.22 gives the diurnal change of frequency of extreme urban rainfall (larger than 50mm/hr) from 1999-HIS, 1999-FUT, and 2030-FUT, by counting number of grids with rainfall larger than 50mm/hr, for all cases over the urban region. Global warming and urban development result in more frequent heavy rainfall for the whole day. The probability of extreme rainfall in 1999-FUT is about 2.5 times at 3 pm compared with 1999-his; even in the morning and late night 1999-FUT still gives more extreme frequent rainfall event. For 2030-FUT, the probability increases about 40% to 80% from 7 am to 12 am compared to 1999-FUT. The most probable time for

extreme rainfall to happen during the day also seen to be delayed in 1999-FUT, compared to 1999-HIS.
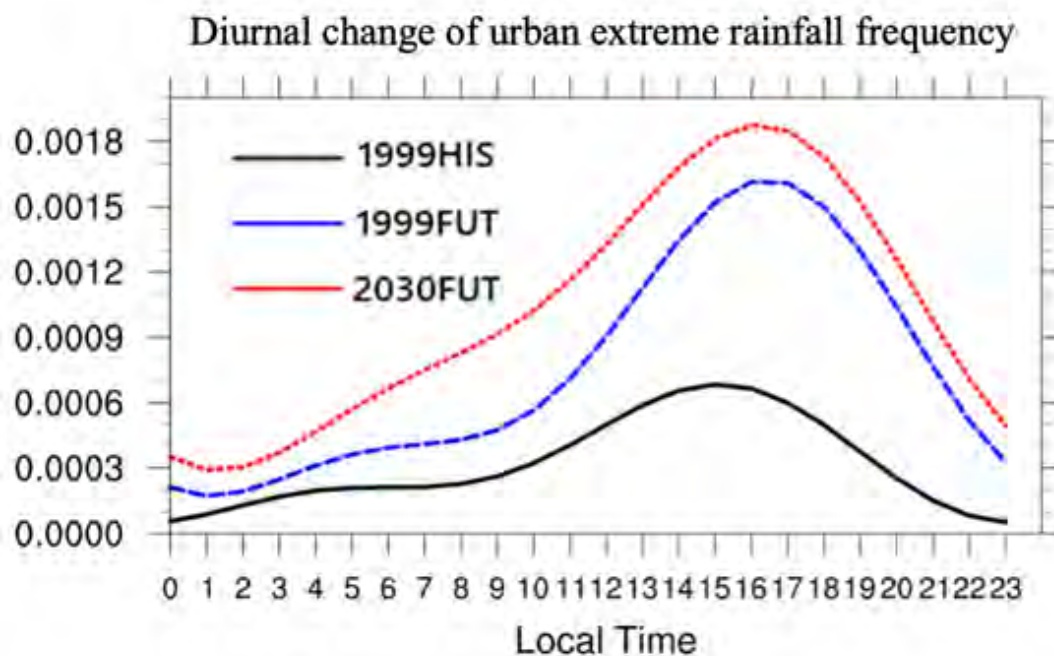
Figure 4.22 *Same as Figure 4.21 except for frequency of rainfall larger than* *50mm/hr.*

The sea breeze front for coastal locations such as the PRD region, can be play an essential role in determining the diurnal rainfall characteristics. Li et al. (2018) showed that the peak diurnal rainfall of Hong Kong, which is found at 8 - 9 am, can be attributed to the arrival of a convergence band from the ocean. Figure 4.23 shows the afternoon convergence at 900hPa in the diurnal cycle, based on results from the middle model domain (see Chapter 2) from 1999-HIS and 1999-FUT, averaged over 12 to 2 pm. For 1999-HIS, the low level convergence band reaches the inland area in the afternoon; at the same time, the same feature in 1999-FUT is still close to the coast line in the afternoon. This suggests that the propagation of sea breeze front is

slower in the 1999-FUT experiments. This may be due to change of land-sea interaction in the model environment. Compared with 1999-HIS, the 2m-temperature in 1999-FUT over the PRD land area increased by about 0.35°C, while the ocean area is warmed by about 0.43°C. Similar difference in ocean vs land warming was also found in the original GFDL-ESM2M data (by about 0.1°C). Weaker land-sea contrast tends to slow down the sea breeze front from ocean to land, which can also delay the most probable time of rainfall over the PRD megacity area in the model environment.

However, weaker land-sea contrast in near-future over the PRD region found here is contrary to general results; there are studies indicating that surface temperature increases more rapidly over land than ocean due to climate change (Dong et al, 2008). The delay of diurnal peak rainfall may only happen during extreme rainfall events. In general, the peak time of diurnal rainfall may happen even earlier due to stronger land sea contrast in the future.
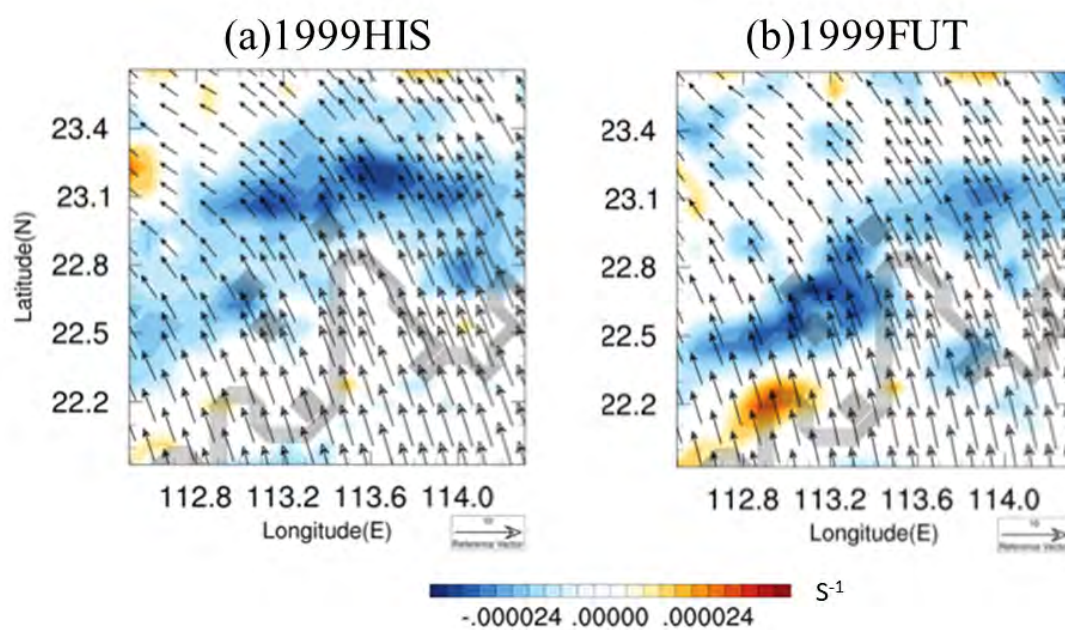
Figure 4.23 *900hpa convergence band phase horizontal distribution in second domain (d02) from (a)1999-HIS and (b)1999-FUT in the afternoon. Convergences are computed by averaging over 12pm, 1pm and 2pm for all selected extreme cases, while blue means convergence and red means divergence, black line represents the coastline. See text for more details.*

4.5 Discussion and Summary

In this part of the study, the impacts of both urban development and global warming on near-future extreme rainfall over the PRD megacity cluster were examined by numerical model simulations. Parallel experiments were designed by varying the urban land use (1999 vs 2030) and climate condition (present vs near-future). Results showed that both urban development and global warming exerted a positive influence on the amount and occurrence rate of extreme rainfall. Though global warming led to a decline of light rainfall (1-20mm/hr) frequency, it significantly increased the probability of heavy rainfall. Urban development enhanced the rainfall probability over a wide range of values (1-110mm/hr), with the likelihood almost doubled for rain rate of 90-100mm/hr. Urban development caused an increase of CAPE, while global warming increased CIN, making convection more difficult to occur. Similar to part 1, the ocean also had an important effect versus urbanization on rainfall in the PRD region; while urban development led to a decreased surface water vapor content in the large scale (2030-FUT vs 1999-FUT), the urban area could still get more water vapor. Moreover, the surface evaporation also increased under a warmer climate, which could leads to an environment with more sufficient water vapor supply in the PRD region.

Moreover, a delay of the peak diurnal rainfall to later afternoon hours in the PRD area under a warmer climate was found in the model results, which was possibly due to modifications on land-sea breeze characteristics and weaker land-sea contrast.

Chapter5
5   Conclusions and discussions
5.1 Major conclusions

By utilizing GFDL-ESM2M historical and near-future simulations, and the WRF-UCM mesoscale model, impacts of urbanization and global warming on extreme rainfall over the PRD megacity cluster were investigated. In part 1, with different land surface (cropland vs urban), and different AH ($0W/m^2$ vs $300W/m^2$), three experiments were designed and downscaling for 26 extreme cases were carried out. Compared with urban surface properties, local extreme rainfall was more sensitive to the intensity of AH, with the mean rainfall increased by about 4-20mm/day in AH300 compared to NO-URBAN. On the other hand, only 0-6mm/day of increase was found between AH0 and NO-URBAN. The hourly precipitation intensity in AH300 increased by 20% at $10-20mm/h^{-1}$ to almost 200% at $90-100mm/h^{-1}$ compared to NO-URBAN. Higher CAPE, lower CIN, and stronger moisture flux convergence due to stronger UHI could lead to a significant increase of extreme rainfall over the PRD urban area. It was also found that, though urbanization would result in lower surface evaporation, moisture supply from the ocean could still support the increase of extreme rainfall magnitudes. In fact, cases with prevailing wind not from the ocean did not show stronger moisture flux convergence over the urban area. This highlights the importance of the background wind direction, and supported the notion that moisture supply from the ocean is essential for exacerbating heavy precipitation due to the AH effect over coastal cities.

In part 2, it was shown that both urban development and global warming could significantly enhance the amount and frequency of extreme rainfall, with comparable increase in precipitation intensity. Global warming could increase rainfall over almost the whole PRD land area by about 3-12mm/day, while the increase due to urban development was around 6-12mm/day. Furthermore, there was negative impact on light rainfall (1-20mm/hr) and less frequent rainfall in the rage of 1-10mm/hr (by around 30% of reduction), which could be attributed to increased CIN under a warmer climate. For heavy rainfall (larger than 50mm/hr), global warming would significantly enhance its probability by about 1.3 to 1.4 times. Urban development, on the other hand, could increase the likelihood of urban rainfall in all ranges (1-110mm/hr). Fractional increase of probability from 1999-FUT to 2030-FUT was no more than 5% for light rainfall (1-10mm/hr), but almost reached 50% to 80% for heavy rainfall (50-110mm/hr). The significant increase of extreme rainfall could be attributed to the regionally increasing CAPE and decrease of CIN. Besides, global warming might lead to a delay in the peak diurnal rainfall about 1-2 hours in the afternoon during extreme precipitation events. This was possibly due to the change of land-sea breeze characteristics and weaker land-sea contrast.

5.2 Limitations and future direction

There are some limitations in this study. For part 1, the SLUCM was used. Due to the limitation of SLUCM and lack of land use data, only one type of urban land cover was utilized, which gave an land surface parameter in urban areas too homogeneous. More heterogeneous distribution of urban parameter should be

incorporated; for instance, the AH value of 300Wm^{-2} (daily maximum intensity) was based on the situation of Hong Kong, and this may not fit the whole PRD region well. Moreover, extreme cases were selected by averaging 16 girds over the South China region in the GFDL-ESM2M historical simulations. This region is quite large and covers part of the South China Sea. The oversized region may lead to some extreme precipitation not found in the PRD land region.

For part 2, urban-induced aerosol can play a cooling effect and inhibit the formation of rainfall in some situations. It is also important to consider the impact of aerosols in urban development. Aerosols were not considered in this study due to the lack of data. Some parameters in SLCUM may also be underestimated based on the WUDAPT default setting; the daily averaging AH in the first and second type of urban land use is only 15Wm^{-2} and 50Wm^{-2} in WUDAPT, respectively. Moreover, the delay of diurnal rainfall peak time may not be robust, long-term intergrations are needed to further support the robustness of this finding.

Moreover, for both two parts of studies, only one GCM data (GFDL-ESM2M) was utilized. If other GCM instead of the GFDL-ESM2M was used as the boundary conditions of WRF, we think the result will be similar. For urban development, the effect is not highly sensitive to the climate condition. Lower surface evaporation will lead to lower surface water vapor content, but stronger surface temperature and moisture flux convergence can still enhance the intensity and frequency of precipitation over the PRD megacity under other GCM climate condition. For climate

change, even in other GCM model, the increase of surface sea temperature and evaporation is consistent with the GFDL-ESM2M (IPCC, 2013), which can still lead to stronger extreme precipitation over the PRD megacity follow the CC relationship.

For future research, other megacity clusters such as Yangtze River Delta (YRD) and Beijing-Tianjin-Hebei area can be considered. Different city clusters might respond differently to global warming and urbanization, due to their different geographical location (coastal or inland city), and background circulations. More numerical experiments will be carried out in this direction.

Reference

Adachi, S., Kimura, F., Kusaka, H., Inoue, T., and Ueda, H. (2012). Comparison of the impact of global climate changes and urbanization on summertime future climate in the Tokyo metropolitan area. Journal of Applied Meteorology and Climatology, 51(8), 1441-1454.

Allen, L., Lindberg, F., and Grimmond, C. (2011). Global to city scale urban anthropogenic heat flux: Model and variability. International Journal of Climatology, 31(13), 1990-2005.

Allan, R., and Soden, B. (2008). Atmospheric warming and the amplification of precipitation extremes. Science (New York, N.Y.), 321(5895), 1481-4.

Atkinson, B. (1971). The Effect of an Urban Area on the Precipitation from a Moving Thunderstorm. Journal of Applied Meteorology (1962-1982), 10(1), 47-55.

Bae, S., Hong, S., and Lim, K. (2016). Coupling WRF Double-Moment 6-Class Microphysics Schemes to RRTMG Radiation Scheme in Weather Research Forecasting Model. Advances in Meteorology, 2016, 1-11.

Bao, J., Feng, J., Wang, Y. Dynamical downscaling simulation and future projection of precipitation over China. Journal of Geophys. Res. Atmos., 120 (2015), pp. 8227-8243.

Bechtel, B., Alexander, P., Böhner, J., Ching, J., Conrad, O., Feddema, J., Mills, G., See, L. and Stewart, I. (2015). Mapping local climate zones for a worldwide database of form and function of cities. International Journal of Geographic Information, 4(1), 199-219.

Bohnenstengel, S., Evans, S., Clark, P., and Belcher, S. (2011), Simulations of the London urban heat island, Q. J. Roy. Meteor. Soc., 137:1625–1640.

Bornstein, R. (1968). Observations of the Urban Heat Island Effect in New York City. Journal of Applied Meteorology.

Bornstein, R., and Lin, Q. (2000), Urban heat islands and summertime convective thunderstorms in Atlanta: three case studies, Atmos. Environ., 34:507–516.

Burian, S., Shepherd, J., Aronica, Giuseppe, and Lanza, Luca. (2005). Effect of urbanization on the diurnal rainfall pattern in Houston. Hydrological Processes, 19(5), 1089-1103.

Cao, Q., Yu, D., Georgescu, M., and Wu, J. (2016). Impacts of urbanization on summer climate in China: An assessment with coupled land-atmospheric modeling. Journal of Geophysical Research: Atmospheres, 121(18), 10,505-10,521.

Changnon, S. (1968). The La Porte weather anomaly—fact or fiction? Bulletin of the American Meteorological Society, 49(1), 4-11.

Changnon, S. (1979), Rainfall changes in summer caused by St. Louis, Science, 205, 402–404.

Changnon, S. (1980). More on the La Porte Anomaly: A Review. Bulletin of the American Meteorological Society, 61(7), 702-711.

Changnon, S., and Huff, F. (1986). Urban-related nocturnal rainfall anomaly at St. Louis. Journal of Climate and Applied Meteorology, Boston, 25(12), 1985-1995.

Chen, F., and Dudhia, J. (2001). Coupling and advanced land surface-hydrology model with the Penn State-NCAR MM5 modeling system. Part I: Model implementation and sensitivity. Monthly Weather Review, 129(4), 569-585.

Chen, F., Mitchell, K., Schaake, J., Xue, Y., Pan, H., Koren, V., Duan, Q., Ek, M., and Betts, A. (1996), Modeling of land surface evaporation by four schemes and comparison with fife observations, J. Geophys. Res., 101(D3):7251–7268.

Chen, F., Kusaka, H., Bornstein, R., Ching, J., Grimmond, C., Grossman-Clarke, S., et al. (2011). The integrated WRF/urban modelling system: Development, evaluation, and

applications to urban environmental problems. International Journal of Climatology, 31(2), 273-288.

Chen, H. (2013). Projected change in extreme rainfall events in China by the end of the 21st century using CMIP5 models. Chinese Science Bulletin, 58(12), 1-10.

Chen, S., Li, W., Du, Y., Mao, C., and Zhang, L. (2015). Urbanization effect on precipitation over the Pearl River Delta based on CMORPH data. Advances in Climate Change Research, 6(1), 16-22.

Cheng, and Chan. (2012). Impacts of land use changes and synoptic forcing on the seasonal climate over the Pearl River Delta of China. Atmospheric Environment, 60(C), 25-36.

Ching, J., Mills, G., el al. (2018). WUDAPT: An Urban Weather, Climate, and Environmental Modeling Infrastructure for the Anthropocene: WUDAPT is an international community-generated urban canopy information and modeling infrastructure to facilitate urban-focused climate, weather, air quality, and energy-use modeling application studies. Bulletin of the American Meteorological Society, 99(9), 1907-1924.

Chou, C., Chen, C., Tan, P., and Chen, K. (2012). Mechanisms for global warming impacts on precipitation frequency and intensity. Journal of Climate, 25(9), 3291–3306.

Coceal, O., and Belcher, S. (2004). A canopy model of mean winds through urban areas. Quarterly Journal of the Royal Meteorological Society, 130(599 PART B), 1349–1372.

Cui, L., and Shi. J. (2012). Urbanization and its environmental effects in Shanghai, China. Urban Climate, 2, 1-15.

Dee, D., Uppala, S., Simmons, A., Berrisford, P., Poli, S., Kobayashi, U., et al. (2011). The ERA-Interim reanalysis: Configuration and performance of the data assimilation system. Quarterly Journal of The Royal Meteorological Society, 137(656), 553-597.

Dong, B., Gregory, J., and Sutton, R. (2009). Understanding Land-Sea Warming Contrast in Response to Increasing Greenhouse Gases. Part I: Transient Adjustment. Journal of Climate, 22(11), 3079-3083,3085-3086,3089-3090,3092-3097.

Dou, J., Wang, Y., Bornstein, R., and Miao, S. (2015). Observed Spatial Characteristics of Beijing Urban Climate Impacts on Summer Thunderstorms. Journal of Applied Meteorology and Climatology, 54(1), 94-105.

Dudhia, J. (1989). Numerical study of convection observed during the Winter Monsoon Experiment using a mesoscale two-dimensional model. Journal of the Atmospheric Sciences 46: 3077-3107

Dunne, J., John, J., Adcroft, A., Griffies, S., Hallberg, R., Shevliakova, E., et al. (2012). GFDL's ESM2 Global Coupled Climate–Carbon Earth System Models. Part I Physical Formulation and Baseline Simulation Characteristics. Journal of Climate, 25(19), 6646-6665.

Dunne, J. (2013). GFDL's ESM2 Global Coupled Climate-Carbon Earth System Models. Part II: Carbon System Formulation and Baseline Simulation Characteristics. Journal of Climate, 26(7), 2247-2267.

Fung, K. (2018). Comparing the Urban Heat and Global Warming Impacts on Extreme Rainfall Characteristics in Pearl River Delta Based on Dynamical Downscaling. Mphill dissertation, the Chinese University of Hong Kong, Hong Kong, 77pp

Gordon, H., Whetton, B., Pittock, P., Fowler, A., and Haylock, M. (1992). Simulated changes in daily rainfall intensity due to the enhanced greenhouse effect: Implications for extreme rainfall events. Climate Dynamics, 8(2), 83-102.

Guo, X., Fu, D., and Wang, J. (2006). Mesoscale convective precipitation system modified by urbanization in Beijing city. Atmos. Res., 82, 112–126.

Gu, Y., and Li. D. (2018). A Modeling Study of the Sensitivity of Urban Heat Islands to Precipitation at Climate Scales. Urban Climate 24 2018: 982-93.

Han, J., Baik, J., and Lee, H. (2014). Urban impacts on precipitation. Asia-Pacific Journal of Atmospheric Sciences,50(1), 17-30.

Han, J., and Pan, H. (2011). Revision of convection and vertical diffusion schemes in the NCEP Global Forecast System. Weather and Forecasting, 26(4), 520-533.

Harnack, R., and Landsberg, H. (1975). Selected Cases of Convective Precipitation Caused by the Metropolitan Area of Washington, D. C. Journal of Applied Meteorology (1962-1982), 14(6), 1050-1060.

Holst, C., Tam, C., and Chan, J. (2016). Sensitivity of urban rainfall to anthropogenic heat flux: A numerical experiment. Geophysical Research Letters, 43(5), 2240-2248.

Hong, S., Noh, Y., and Dudhia, J. (2006). A New Vertical Diffusion Package with an Explicit Treatment of Entrainment Processes. Monthly Weather Review, 134(9), 2318-2341.

Hou, A., Ni, G., Yang, H., and Lei, Z. (2013). Numerical Analysis on the Contribution of Urbanization to Wind Stilling an Example over the Greater Beijing Metropolitan Area. Journal of Applied Meteorology and Climatology, 52(5), 1105-1115.

Hsu, P., Li, T., Luo, J., Murakami, H., Kitoh, A., and Zhao, M. (2012). Increase of global monsoon area and precipitation under global warming: A robust signal? Geophysical Research Letters, 39(6).

Huang, D., and Gao, S. (2018). Impact of different reanalysis data on WRF dynamical downscaling over China. Atmospheric Research, 200, 25-35.

Huang, H., Ooka, R., and Kato, S. (2005). Urban thermal environment measurements and numerical simulation for an actual complex urban area covering a large district heating and cooling system in summer. Atmospheric Environment,39(34), 6362-6375.

Huff, F., and Changnon, S. (1972). Climatological Assessment of Urban Effects on Precipitation at St. Louis. Journal of Applied Meteorology (1962-1982), 11(5), 823-842.

Hutcheon, R., Johnson, R., Lowry, W., Black, C., and Hadley, D. (1967). Observations of the urban heat island in a small city. Bulletin of the American Meteorological Society, 48(1), 7-9.

Iacono, M., Delamere, J., Mlawer, E., Shephard, M., Clough, S., and Collins, W. (2008), Radiative forcing by long-lived greenhouse gases: Calculations with the AER radiative transfer models, J. Geophys. Res., 113(D13103).

Iwashima, T., and Yamamoto, R. (1993). A statistical analysis of the extreme events: Long-term trend of heavy daily precipitation. Journal of the Meteorological Society of Japan, 71(5), 637-640.

Jin, M., Li, Y., and Su, D. (2015). Urban-Induced Mechanisms for an Extreme Rainfall Event in Beijing China: A Satellite Perspective. Climate, 3(1), 193–209.

Karl, T., and Knight, R. (1998) Secular trends of precipitation amount, frequency, and intensity in the USA. Bull. Amer. Meteor. Soc., 79, 231-241.

Kharin, V., Zwiers, F., Zhang, X., and Hegerl, G. (2007). Changes in temperature and precipitation extremes in the IPCC ensemble of global coupled model simulations. Journal of Climate, 20(8), 1419-1444.

Krishtawal, C., Niyogi, D., Tewari, M., Pielke, R., and Shepherd, M. (2010), Urbanization signature in the observed heavy rainfall climatology over India. International Journal of Climatology, 30(13), 1908-1916.

Kusaka, H., Kondo, H., Kikegawa, Y., and Kimura, F. (2001). A Simple Single-Layer Urban Canopy Model for Atmospheric Models: Comparison with Multi-Layer and Slab Models. Boundary-Layer Meteorology, 101(3), 329-358.

Kusaka, H., Nawata, K., Suzuki-Parker, A., Takane, Y., and Furuhashi, N. (2014). Mechanism of Precipitation Increase with Urbanization in Tokyo as Revealed by Ensemble Climate Simulations. Journal of Applied Meteorology and Climatology, 53(4), 824-839.

Langenberg, H, and Feser, F. (2000). A Spectral Nudging Technique for Dynamical Downscaling Purposes. Monthly Weather Review, 128(10), 3664–3673.

Leung, Y., Yeung, K., Ginn, E., and Leung, W. (2004). Climate change in Hong Kong. Hong Kong Observatory Technical Note, No. 107.

Liang, P., and Ding, Y. (2017). The long-term variation of extreme heavy precipitation and its link to urbanization effects in Shanghai during 1916–2014. Advances in Atmospheric Sciences, 34(3), 321-334.

Li, M., Song, Y., Mao, Z., Liu, M., and Huang, X. (2016). Impacts of thermal circulations induced by urbanization on ozone formation in the Pearl River Delta region, China. Atmospheric Environment, 127, 382-392.

Li, J., Wu, Z., Jiang, Z., and He, J. (2010). Can global warming strengthen the East Asian summer monsoon? Journal of Climate, 23(24), 6696–6705.

Li, Y., and Zhao, X. (2012). An empirical study of the impact of human activity on long-term temperature change in China: A perspective from energy consumption. Journal of Geophysical Research: Atmospheres, 117(D17).

Lin, C., Chen, W., Liu, S., Liou, Y., Liu, G., and Lin, T. (2008). Numerical study of the impact of urbanization on the precipitation over Taiwan. Atmospheric Environment, 42(13), 2934-2947.

Liu, J. and Niyogi, D. (2019). Meta-analysis of urbanization impact on rainfall modification. Scientific Reports, 9(1), 7301.

Long-term climate change: Projections, commitments and irreversibility. (2013). In Climate Change 2013 the Physical Science Basis: Working Group I Contribution to the Fifth Assessment Report of the Intergovernmental Panel on Climate Change (Vol. 9781107057999, pp. 1029-1136). Cambridge University Press.

Miao, S., Chen, F., Li, Q., and Fan, S. (2011). Impacts of urban processes and urbanization on summer precipitation: A case study of heavy rainfall in Beijing on 1 August 2006. Journal of Applied Meteorology and Climatology, 50(4), 806-825.

Miao, S., Li, Q., Wang, Y., Chen, F., LeMone, M., and Tewari, M. (2009). An observational and modeling study of characteristics of urban heat island and boundary layer structures in Beijing. Journal of Applied Meteorology and Climatology, 48(3), 484-501.

Mills, G., Ching, J., See, L., Bechtel, B., and Foley, M. (2015). An Introduction to the WUDAPT project. In Proceedings of the 9th International Conference on Urban Climate, Toulouse, France (pp. 20-24).

Mlawer, E., Taubman, S., Brown, P., Iacono, M., and Clough, S. (1997). Radiative transfer for inhomogeneous atmospheres: RRTM, a validated correlated-k model for the longwave. Journal of Geophysical Research: Atmospheres, 102(D14), 16663-16682.

Mohajerani, A., Bakaric, J., and Jeffrey-Bailey, T. (2017). The urban heat island effect, its causes, and mitigation, with reference to the thermal properties of asphalt concrete. Journal of Environmental Management,197, 522-538.

Oke, T. (1973). City size and the urban heat island. Atmospheric Environment, 7(8), 769-779.

Oke, T. (1976). The distinction between canopy and boundary layer urban heat islands. Atmosphere, 14(July 2015), 268–277.

Oke, T. (1981). Canyon geometry and the nocturnal urban heat island: comparison of scale model and field observations. J. Climatology, 1, 237–254.

Oke, T. (1988), The urban energy balance. Progress in Physical Geography, 12(491).

Orville, R., Huffines, G., Nielsen-Gammon, J., Zhang, R., Ely, B., Steiger, S., et al. (2001). Enhancement of cloud-to-ground lightning over Houston, Texas. Geophysical Research Letters, 28(13), 2597-2600.

Paul, S., Ghosh, S., Mathew, M., Devanand, A., Karmakar, S., and Niyogi, D. (2018). Increased Spatial Variability and Intensification of Extreme Monsoon Rainfall due to Urbanization. Sci Rep, 8(1), 3918.

Rani, S., Sreekesh, S. (2018). Variability of Temperature and Rainfall in the Upper Beas Basin Western Himalaya. Climate Change Extreme Events and Disaster Risk Reduction pp 101-120.

Raymond, J., Yarkoni, S., and Andriyash, E. (2016). Global Warming: Temperature Estimation in Annealers. Frontiers in ICT, 3, Frontiers in ICT, Nov 7, 2016.

Sachweh, M., and Koepke, P. (1995). Radiation fog and urban climate. Geophysical Research Letters, 22(9), 1073-1076.

Shastri, H., Paul, S., Ghosh, S., and Karmakar, S. (2015). Impacts of urbanization on Indian summer monsoon rainfall extremes. Journal of Geophysical Research: Atmospheres, 120(2), 496-516.

Sheffield, J., and Wood, E. (2008). Projected changes in drought occurrence under future global warming from multi-model, multi-scenario, IPCC AR4 simulations. Climate Dynamics,31(1), 79-105.

Shepherd, J. (2006). Evidence of urban-induced precipitation variability in arid climate regimes. Journal of Arid Environments, 67(4), 607-628.

Shepherd, J., and Burian, S. (2003). Detection of Urban-Induced Rainfall Anomalies in a Major Coastal City. Earth Interactions, 7, Earth Interactions, 2003, Vol.7.

Shem, W., and Shepherd, M. (2009). On the impact of urbanization on summertime thunderstorms in Atlanta: Two numerical model case studies. Atmospheric Research, 92(2), 172-189.

Shimadera, H., Hayami, H., Morino, Y., Toshimasa, O., Satoru, C., Shuichi, H., and Naoki, K. (2013) Analysis of summertime atmospheric transport of ne particulate matter in Northeast Asia, Asia-Paci c Journal of Atmospheric Sciences, 49(3), 347–360.

Shimadera, H., Kondo, A., Shrestha, K., Kitaoka, K., and Inoue, Y. (2015). Numerical Evaluation of the Impact of Urbanization on Summertime Precipitation in Osaka, Japan. Advances in Meteorology,2015(2015), 149-159.

Skamarock, W., Klemp, J., Dudhia, J., Gill, D., Barker, D., Duda, M., Huang, X., Wang, W., and Powers, J. (2008), A description of the advanced research WRF version 3 NCAR Tech. Note, NCAR/TN–475+STR.

Solecki, D., Rosenzweig, C., Parshall, L., Pope, G., Clark, M., Cox, Jennifer; M., (2005). Mitigation of the heat island effect in urban New Jersey. Global Environmental Change Part B: Environmental Hazards. 6 (1): 39–49.

Soltani, A., and Sharifi, E. (2017). Daily variation of urban heat island effect and its correlations to urban greenery: A case study of Adelaide. Frontiers of Architectural Research, 6(4), 529-538.

Stewart, I., Oke, T., Krayenhoff, E. (2014). Evaluation of the 'local climate zone' scheme using temperature observations and model simulations. Int. J. Climatol. 34 (4), 1062–1080.

Streutker, D., Rice University, and William M. Rice Institute. (2003). A Study of the Urban Heat Island of Houston, Texas, ProQuest Dissertations and Theses.

Tayanç, M., and Toros, H. (1997). Urbanization effect on reginal climate change in the case of four large cities of Turkey. Climatic Change, 35(4), 501-524.

Tewari, M. F., Chen, F., Kusaka, H., and Miao, S. (2008). Coupled WRF/Unified Noah/urban-canopy modeling system, NCAR WRF Documentation, NCAR, Boulder, 1–20.

Vukovich, F., and King, W. (1980). A Theoretical Study of the St. Louis Heat Island: Comparisons Between Observed Data and Simulation Results on the Urban Heat Island Circulation. Journal of Applied Meteorology (1962-1982), 19(7), 761-770.

Wang, D., Jiang, P., Wang, G., and Wang, D. (2015). Urban extent enhances extreme precipitation over the Pearl River Delta, China. Atmospheric Science Letters, 16(3), 310-317.

Wang, D., Wang, D., Qi, X., Liu, L., and Wang, X. (2018). Use of high-resolution precipitation observations in quantifying the effect of urban extent on precipitation characteristics for different climate conditions over the Pearl River Delta, China. Atmospheric Science Letters, 19(6).

Wang, J., Feng, J., and Yan, Z. (2015). Potential sensitivity of warm season precipitation to urbanization extents: Modeling study in Beijing-Tianjin-Hebei urban agglomeration in China. Journal of Geophysical Research: Atmospheres,120(18), 9408-9425.

Wang, X., He, X., Miao, S., and Dou, Y. (2018). Numerical simulation of the influence of aerosol radiation effect on urban boundary layer. Science China Earth Sciences, 61(12), 1844-1858.

Wong, M., Yang, J., Weng, Q., Menenti, M., and Chan, P. (2015). Modeling of Anthropogenic Heat Flux Using HJ-1B Chinese Small Satellite Image: A Study of Heterogeneous Urbanized Areas in Hong Kong. IEEE Geoscience and Remote Sensing Letters, 12(7), 1466-1470.

Wu, L., and Zhang, J. (2018). Assessing population movement impacts on urban heat island of Beijing during the Chinese New Year holiday: Effects of meteorological conditions. Theoretical and Applied Climatology, 131(3), 1203-1210.

Xu, K., Yang, D., Yang, H., Li, Z., Qin, Y., Shen, Y. (2015). Spatio-temporal variation of drought in China during 1961–2012: A climatic perspective. Journal of Hydrology., 526, 253-264.

Yaduvanshi, A., Ranade A. (2017). Long-Term Rainfall Variability in the Eastern Gangetic Plain in Relation to Global Temperature Change. Atmosphere-Ocean 552, 94-109.

Zhang, C., Chen, F., Miao, S., Li, Q., Xia, X., and Xuan, C. (2009). Impacts of urban expansion and future green planting on summer precipitation in the Beijing metropolitan area. J. Geophys. Res., 114, D02116

Zhang, C., Miao, S., Li, Q., Chen, F., Xia, X., and Xuan, C. (2009). Impacts of urban expansion and future green planting on summer precipitation in the Beijing metropolitan area. Journal of Geophysical Research Atmospheres, 114(2).

Zhang, Y., Miao, S., Dai, Y., and Bornstein, R. (2017). Numerical simulation of urban land surface effects on summer convective rainfall under different UHI intensity in Beijing. Journal of Geophysical Research: Atmospheres, 122(15), 7851-7868.

Zhao, C., Jiang, Q., Sun, Z., Zhong, H., and Lu. S (2013). Projected Urbanization Impacts on Surface Climate and Energy Budgets in the Pearl River Delta of China. Advances in Meteorology,2013(2013), 145-154.